Proceedings of the 4th BSME-ASME International Conference on Thermal Engineering
27-29 December, 2008, Dhaka, Bangladesh

MICROSTRUCTURE AND MECHANICAL BEHAVIOR OF THERMO-MECHANICALLY TREATED TRIP STEELS

M.A. Islam

Materials and Metallurgical Engineering Department
BUET, Dhaka-1000, Bangladesh.
e-mail:aminulislam@mme.buet.ac.bd

ABSTRACT

Worldwide environmental concern put the automobile industries under tremendous pressure to reduce the weight of the vehicles without compromising the crashworthiness. Similarly, reduction of building weight might play an important role to reduce the damage from earthquake. TRIP (transformation induced plasticity) steel is one of the newly developed high strength steels to fulfill the present growing demands in the field of various structural applications. In this research work, initiative has been taken to compare the microstructure and mechanical properties of traditional structural steels with that of TRIP steels and the underlying phenomena related to the latter have been discussed. Experimental results show that TRIP steels provide excellent ductility without compromising its strength.

Key words: *Strength, TRIP steels, Retained austenite*

1. INTRODUCTION

TRIP-aided multiphase steels are a new generation of low-alloy steels that exhibit a combination of enhanced strength and ductility, thus satisfying the requirements of automotive industry for good formable high-strength steels. Concerning the environmental issue, reduction in the fuel consumption as well as the CO_2 emissions is an increasing demand throughout the whole world. As a result, it has become one of the most important tasks for automobile industries to make reduction in the weight of auto bodies without compromising the crashworthiness of the vehicle and safety of the passengers. In this situation, application of high strength steel sheets can provide necessary solution. However, the key problem concerning the use of high strength steels is that the increased strength decreases the elongation (Fig.1), deep draw ability and stretch ability of the sheets [1]. Recently, large amount of high strength steels (HSS) are used for chassis and underbody components of auto-bodies, which is about 30% of the total weight of the car [1,2]. The stress-strain conditions experienced by the structural steels in building and bridges during the time of earthquake might be compared to the low cycle fatigue. It has been observed that the low cycle fatigue properties of TRIP steels are excellent [3-5] and thus this group of steel might be a potential candidate as building materials in earth quake sensitive countries like Bangladesh, Indonesia and Japan.

The objective of this research work is to discuss the thermo-mechanical treatment to develop controlled microstructural phases essential for a good combination of tensile

properties and also to explain the underlying stress-induced phase transformation phenomena for the characteristic tensile behavior of TRIP steel.

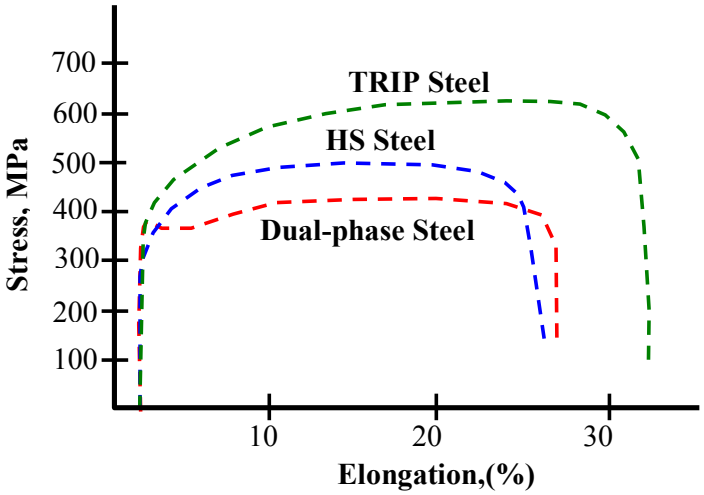

Table.1 Chemical compositions of TRIP steels (wt%).

Element	Steel A	Steel B
C	0.09	0.19
Si	1.29	1.21
Mn	1.58	1.60
P	0.010	0.008
S	0.0014	0.0009
N	0.005	0.003

Fig.1 Stress-strain diagram of TRIP, HS and DP steels.

2. EXPERIMENTAL

The materials of this study were commercially available TRIP steels having the chemical compositions presented in Tab.1. After continuous casting, the ingots were thermo-mechanically processed according to the schedule (double pass; $TMA_{\varepsilon 1}$+ $TMA_{\varepsilon 2}$) presented in Fig.2. Following necessary steps, metallographic samples were cut, polished and etched in nital to reveal the microstructures. After etching, they were observed in the scanning electron microscope (SEM) and photographed. Tensile tests were also carried out and the fracture surfaces were observed and photographed in the SEM.

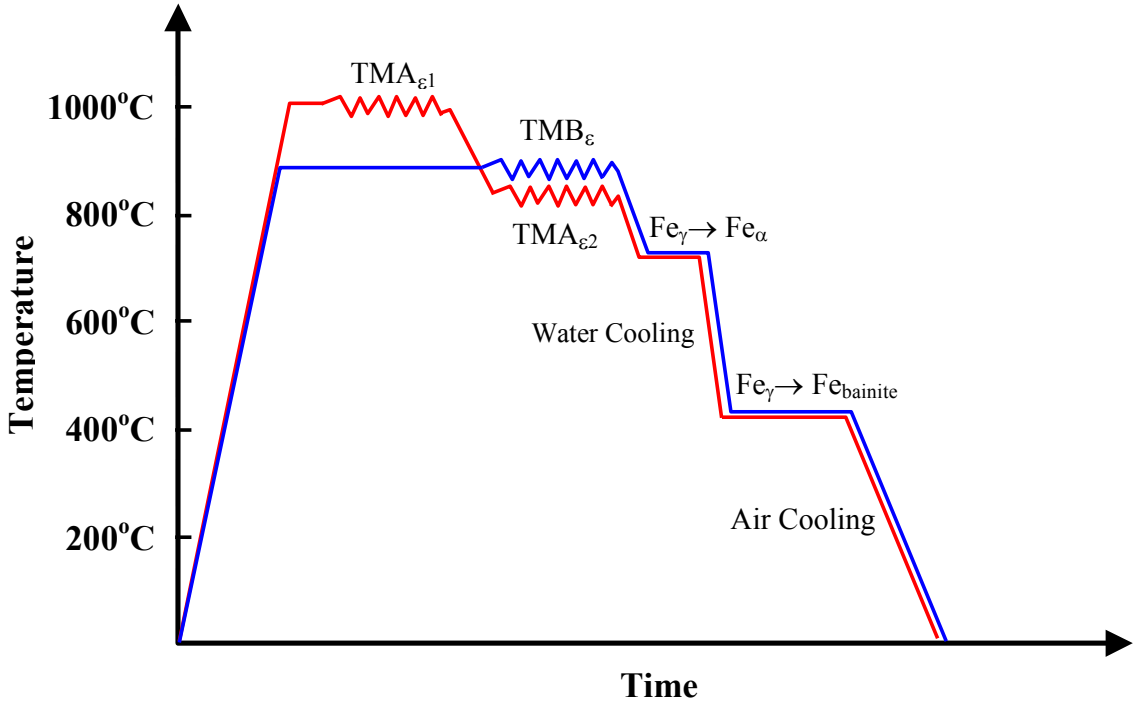

Fig.2 Schematic diagram of a typical thermo-mechanical treatment process.

3. RESULTS

3.1 Microstructures

In the present work, both TRIP steels exhibited triple-phase microstructures consisting of ferrite (F), bainite (B) and retained austenite (RA), Fig.3.

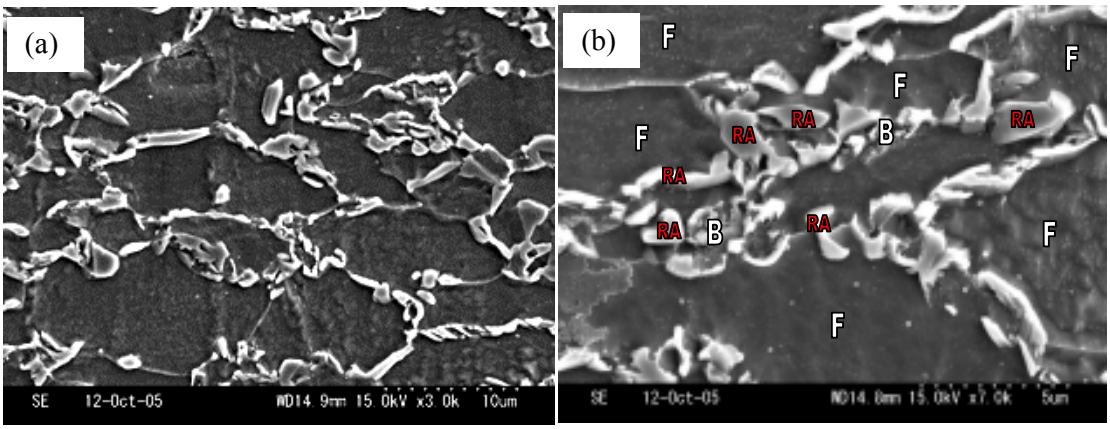

Fig.3 Microstructures of TRIP steel (a) low magnification and (b) high magnification.

3.2 Tensile Properties

The nominal stress-strain curves are shown in Fig.4. From Fig.4, it is evident that steel B gave comparatively lower elongation before final fracture. However, both steels showed reasonably high values of total elongation with ductile fracture surfaces, Fig.5.

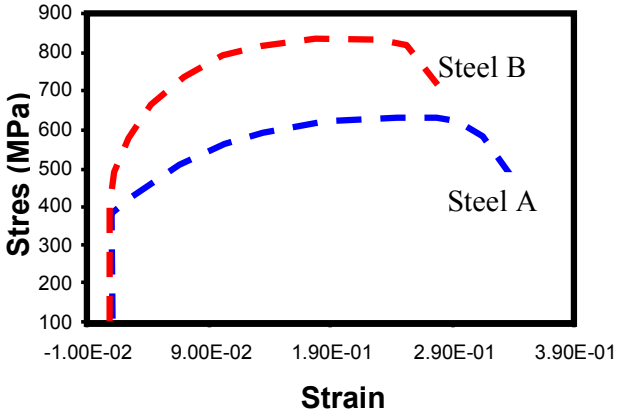

Fig.4 Stress-strain curves of two TRIP steels.

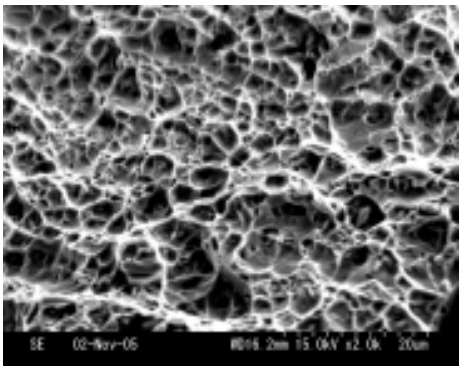

Fig.5 Typical tensile fracture surface of TRIP steel at room temperature.

4. DISCUSSION

4.1 Control of Microstructure During Thermo-Mechanical Treatment

Depending on expected grain size and microstructures, heating may be to about 850°C for single pass rolling (TMBε) or about 1000°C for double pass rolling (TMAε_1 + TMAε_2), Fig.2. At the required temperature, the sample is held for about 30 minutes. After structural homogenization, it becomes ready for mechanical treatment, i.e., for rolling. During rolling,

austenite grains are severely elongated. Samples with severely elongated austenite grains are held isothermally in furnace at around 700^{o}C for a short period to allow a partial transformation of austenite to ferrite grain. During isothermal holding in the furnace some austenite grains are transformed to ferrite grains and rest of austenite grains become equiaxed with possible carbon enrichment. Because the solubility of carbon in ferrite is very very low compared to that in austenite. When structures with ferrite and enriched austenite are cooled very quickly to about 400^{o}C, the carbon enriched austenite grains transform to bainite, which is relatively stronger than austenite.

Here it is to be noted that all retained austenite cannot be transformed to bainite. The reason is that sufficient amount of manganese, silicon and aluminium are added in the steel. Manganese and silicon acts as austenite stabilizer, whereas silicon and aluminium act to retard carbide formation [6,7]. Altogether, during short period of holding below the lower critical temperature, only a certain fraction of austenite gets chance to be transformed to ferrite. Due to the compositional reason mentioned earlier, all retained austenite cannot get chance to transform to bainite. After bainitic transformation a certain portion of austenite is retained in the structure. After this phase transformation, the sample is air cooled which may or may not cause transformation of retained austenite to martenite depending on carbon content in the retained austenite and cooling rate.

4.2 Microstructures of TRIP Steels and Traditional Structural Steels

As mentioned earlier, TRIP steels showed three different phases as ferrite, retained austenite and bainite. Depending on carbon content and cooling rate martensite needles might also be observed. Here it is to be noted that retained austenite is a meta-stable phase, which transforms to a more stable phase (bainite or martensite) under favorable conditions. However, traditional normalized structural steels contain ferrite and pearlite, Fig.6. Depending on carbon content and cooling rate, the proportions of ferrite and pearlite vary. Here it is to be mentioned that both ferrite and pearlite are stable phases at room temperature. In some cases, medium carbon structural steels are cooled through water spray after rolling to increase the strength of the steel. In such cases, medium carbon steels might contain bainitic structures at surface to sub-surface areas, Fig.6c. This bainite is also stable at room temperature.

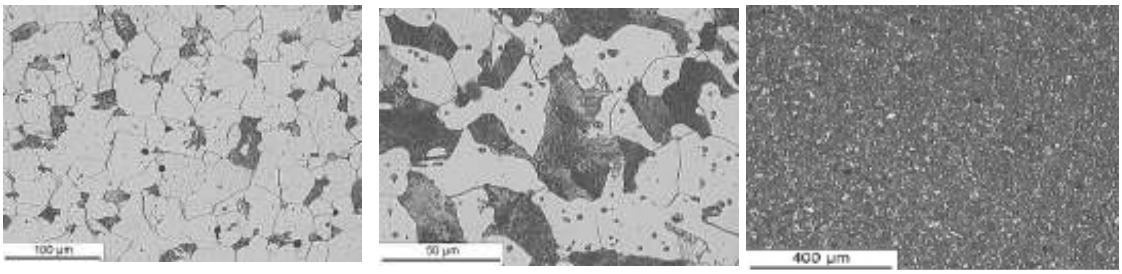

Fig.6 Microstructure of traditional steels (a) 0.1%C, (b) 0.35%C and (c) typical bainitic structure.

4.3 Tensile Behavior of Traditional Structural Steels

In the case of traditional steels, total applied load is absorbed by elastic deformation and plastic deformation. For high strength traditional structural steels dislocation movement is difficult. As a result, with increase in strength the ductility gradually decreases because of

severe level of dislocation pile-up, which causes local micro-crack easily. This micro-crack also induces local stress concentration, which ultimately forms macro-crack easily and then failure takes place within a short period of time. So, ductility level decreases sharply.

4.4 Tensile Behavior of TRIP Steels

Now, the tensile behavior of TRIP steels will be discussed. TRIP steels are not very soft like low carbon steel/mild steel and also not very hard like bainitic structural steel. So, total elongation related to elastic and plastic deformation will be moderate as expected. In the case of TRIP steel, another source of elongation is due to strain-induced plasticity. When the applied load cause stress above the yield point, then plastic deformation starts and stress gradually increases due to strain hardening. In this situation, at a point, necking starts, which causes local stress concentration as well as severe local strain. This strain transforms the meta-stable retained austenite to relatively high strength bainite as shown by filled (red) circles, Fig.7. Due to increase in local strength, necking tries to expand towards upper and lower region rather than penetrating towards the center of materials. As a result, crack loses its sharpness and thus catastrophic failure is avoided. As necking tries to move towards surface areas and causes stress concentration there, the meta-stable austenite phase at that region also starts to transform to bainite. This transformation continues to some extent and absorbs applied energy, as the process of transformation is stress-induced [1,2,8,9]. During earthquake or car crash, certain portion of the impact experienced by the structural members is absorbed by this stress-induced transformation and increases the strength of the structural members. Thus rest portion of the impact energy either cannot exceed the strength required for final fracture or cause severe catastrophic failure and thus car passengers as well as dwellers inside the residential structures are saved from major injury.

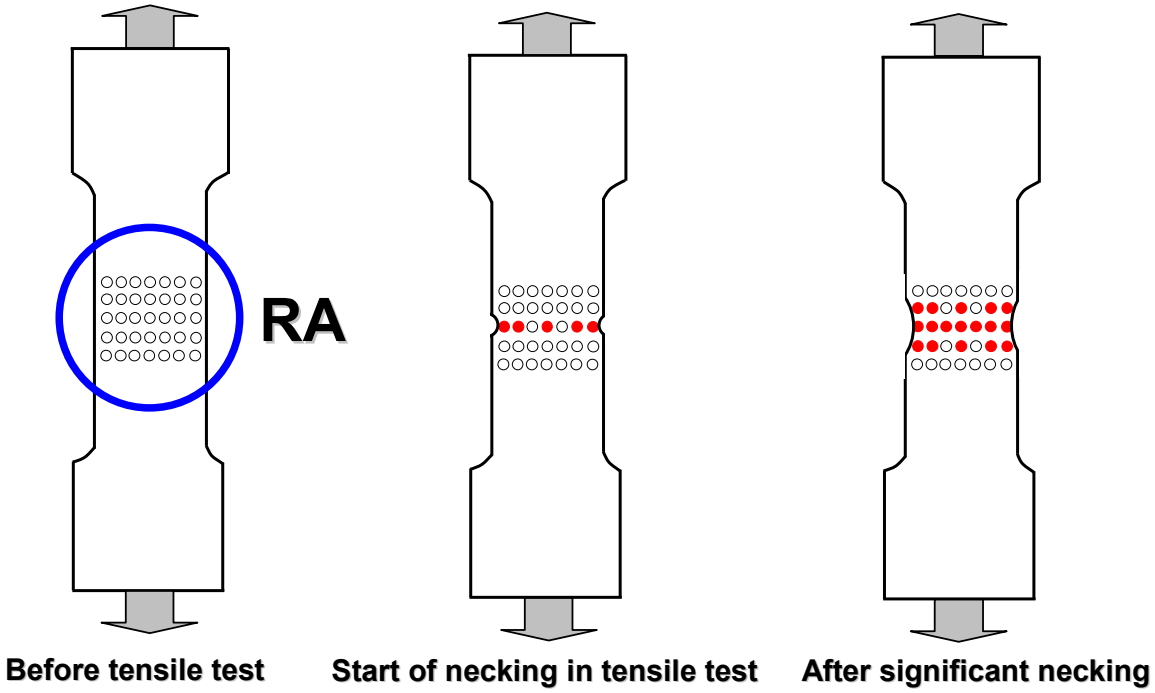

Fig.7 Gradual austenite phase transformation during tensile test. Note: Filled (red) circles denote bainite.

5. CONCLUSIONS

1. Traditional structural steels have stable phase(s). The microstructures of TRIP steel are composed of ferrite, austenite and bainite, where austenite is a meta-stable phase and tries to transform to relatively more stable bainitic phase when gets chance under stressed condition.

2. The applied load in traditional structural steel is absorbed by elastic and plastic deformation, whereas in TRIP steel, a third source to absorb applied energy is by stress-induced phase transformation.

3. The capability of energy absorption in TRIP steel by stress-induced phase transformation provides more ductility to the structural steel component and reduces severity of catastrophic failure as a certain portion of the impact caused by car crash or by earthquake is absorbed by phase transformation.

6. REFERENCES

[1] Takahashi, M., Kawano, O., Hayashida, T., Okamoto, R., Taniguchi, H., High Strength Hot-rolled Steel Sheets for Automobiles, Report No. 88, 2003, Nippon Steel Company, Japan.
[2] Beynon, D., Jones, T.B., Fourlaris, G., Effect of High Strain Rate Deformation on Microstructure of Trip Steels Tested Under Dynamic Tensile Conditions, Materials Science and Technology, 21(2005), 1, pp.103-112.
[3] Islam, M.A., Tomota, Y., Tensile and Plane Bending Fatigue Properties of Two TRIP Steels at Room Temperature in the Air, Materials Engineering and Performance, 16(2007), 2, pp.248-253.
[4] Islam, M.A., Chen, S., Tomota, Y., Proceedings, First Afro-Asian Conference, Cairo, Egypt, 2006, pp.30-41.
[5] Islam, M.A., Chen, S., Tomota**,** Y., Proceedings, International Conference on Structure Integrity and Failure (SIF-2006), Sydney, Australia, 2006, pp.361-368.
[6] Zaefferer, S., Ohlert, J., Bleck, W., A Study of Microstructure, Transformation Mechanisms and Correlation Between Microstructure and Mechanical Properties of a Low Alloyed TRIP Steel, Acta Materialia, 52(2004), pp.2765-2778.
[7] Son, D., Choi, H., Shin, E., Analysis of the Retained Austenite Stability in TRIP Steels by X-ray and Neutron Diffraction, Proceedings, International Symposium on Research Reactor and Neutron Science – In Commemoration of the 10th Anniversary of HANARO- Daejeon, Korea, April 2005, pp.706-710.
[8] Hulka, K., The Role of Niobium in Cold Rolled Trip Steel, Materials Science Forum, 473(2005), pp.91-102.
[9] Berrahmoune, M.R., Berveiller, S., Inal, K., Moulin, A., Patoor, E., Analysis of the Martensite Transformation at Various Scales in TRIP Steel, Materials Science & Engineering A, 378(2004), pp.304-307.

Proceedings of the 4th BSME-ASME International Conference on Thermal Engineering
27-29 December, 2008, Dhaka, Bangladesh

PREDICTION OF SURFACE ROUGHNESS IN END MILLING OF PREHEATED TI6AL4V ALLOY USING COUPLED ARTIFICIAL NEURAL NETWORK AND RESPONSE SURFACE METHODOLOGY

Md. Anayet U Patwari[1,2], A.K.M. Nurul Amin[2], Turnad L. Ginta3, M.A. Lajis[4]

[1] Mechanical and Chemical Engineering Department, Islamic University of Technology, Dhaka, Bangladesh
[2]Department of Manufacturing and Materials Engineering, International Islamic University Malaysia
[3] Mechanical Engineering Department, Universitag Jenderal Achmad Yani, Bandung, Indonesia
[4] Faculty of Mechanical & Manufacturing Engineering, UTHM, Batu Pahat, Johor, Malaysia
[1]Corresponding author e-mail: aupatwari@hotmail.com

ABSTRACT:

In this work, a surface roughness model was developed by coupling artificial neural network (ANN) with response surface methodology for the investigation and prediction of the relationship between cutting parameters, work-piece preheated temperature and surface roughness during high speed end milling of Ti6Al4V. For this interpretation, advantages of statistical experimental design technique, experimental measurements, artificial neural network were exploited in an integrated manner. Cutting experiments are designed based on small centre composite design technique to develop a response surface mode. The input parameters of the model are the cutting parameters: cutting speed, feed, and work-piece preheated temperature. The output parameter of the model was surface roughness. This response surface model was coupled with artificial neural network for the surface roughness model. A predictive model for surface roughness was created using a feed-forward back-propagation neural network exploiting experimental data. The network was trained with pairs of inputs/outputs datasets generated when end milling Ti6Al4V alloy with WC-Co insert. The model can be used for the analysis and prediction for the complex relationship between cutting conditions and the surface roughness in metal-cutting operations for efficient and economic production.

Key words: *Surface Roughness, Response surface methodology, preheating, Artificial Neural Network*

1. INTRODUCTION

Surface roughness is one of the important factors for evaluating work-piece quality during the machining process because the quality of surface roughness affects the functional characteristics of the work-piece such as compatibility, fatigue resistance and surface friction. Surface roughness is expressed as the irregularities of material resulted from various machining operations. In quantifying surface roughness, average surface roughness definition, which is often represented with Ra symbol, is commonly used. In workshop practice, cutting parameters are selected from machining databases or specialized handbooks, but the range given in these sources

are actually starting values, and are not the optimal values. To ensure the quality of machining products, and to reduce the machining costs and increase the machining effectiveness, it is very important to select the machining parameters. A machinability model may be defined as a functional relationship between the input of independent cutting variables (speed, feed, depth of cut) and the output known as responses (tool life, surface roughness, cutting force, etc) of a machining process [1].

The factors that affect the surface roughness during the end milling process include tool geometry, feed rate, depth of cut and cutting speed. Several researchers have studied the end milling process in the recent years. The researchers also used response surface methodology (RSM) to explore the effect of cutting parameters as cutting speed, feed rate and axial depth of cut. Alauddin et al. [2] developed a mathematical model to predict the surface roughness of steel after end milling. The prediction model was expressed via cutting speed, feed rate and depth of cut. Fuh and Hwang [3] used RSM to construct a model that can predict the milling force in end milling operations. Sundaram and Lambert [4 -5] considered six variables i.e speed, feed, depth of cut, time of cut, nose radius and type of tool to monitor surface roughness. But it is very important to investigate the effect of work-piece preheated temperature on the surface roughness along with the other major cutting parameters effects considering nonlinearity and time variant. Compared to traditional computing methods, the artificial neural networks (ANNs) are robust and global. ANNs have the characteristics of universal approximation, parallel distributed processing, hardware implementation, learning and adaptation, and multivariable systems [6]. ANNs have been extensively applied in modeling many metal-cutting operations such as turning, milling, and drilling [7-9]. However, this study was inspired by the very limited work on the application of ANNs in modeling the relationship between cutting conditions, work-piece preheating temperature and the surface roughness during high-speed end milling of Titanium alloy.

2. EXPERIMENTAL SETUP

Cutting tests was conducted mainly on Vertical Machining Center (VMC ZPS, Model: 1060) powered by a 30 KW motor with a maximum spindle speed of 8000 rpm. Fig.1 shows the preheating set up used in vertical machining centre for preheated machining. Surface measuring instrument (SURFTEST) SV-500 was used to measure the surface roughness ($R_{a)}$ are shown in Fig. 2.

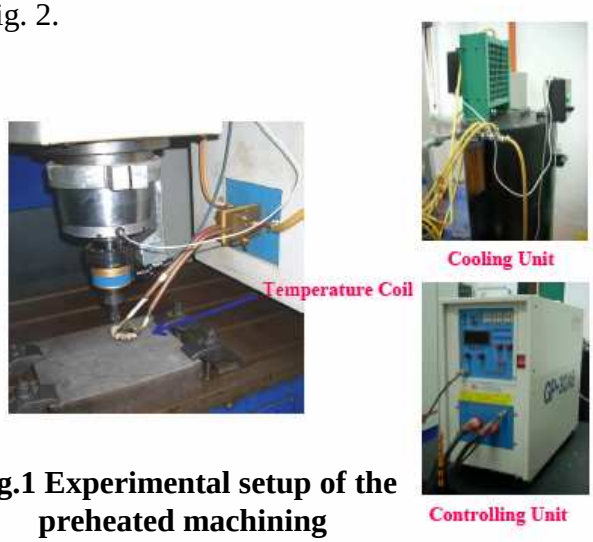

Fig.1 Experimental setup of the preheated machining

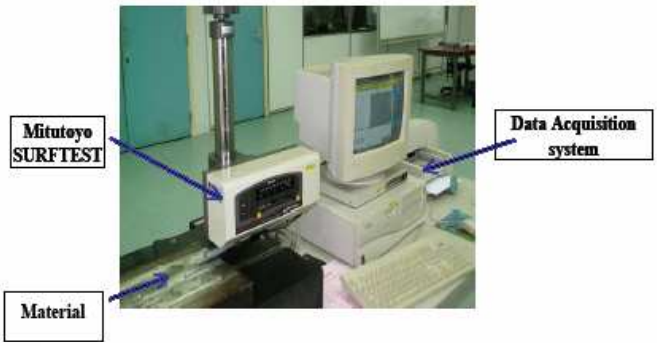

Fig.2 Surface Roughness Measurement Apparatus

Tool (inserts)-SANDVIK grade PM1030 Insert code: R390- 11 T3 08E- PL, Insert coating material: carbide, Working condition: light to medium milling. Insert geometries are given below in Table 1.

Table 1: Cutting tool material and geometry data

Tool material	*Dimension(mm)*					Number of cutting edge
	l_a	iW	s	b_s	r_ε	
Uncoated WC-Co insert (R390-11 T3 08E-NL H13A)	11	6.8	3.59	1.5	0.8	2
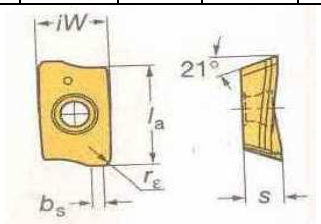						

3. DEVELOPMENT OF QUADRATIC RESPONSE SURFACE MODEL

The design of experiment has a major effect on the total number of required experiments. A well planed experimental design can reduce the number of experiments quite substantially. For this reason, a small CCD with 2 blocks and 4 replication of centre point in each factorial block was selected to design the experiments. This ultimately resulted in 14 experiments, with 4 other factorial points and 6 axial points. This experimental design provides 5 levels for each of the independent variables. The cutting variables with different cutting conditions are given below:

x_1, Cutting speed, V (m/min)	: 30.6, 39, 70, 126, 160.6
x_2, Feed, f_z (mm/tooth)	: 0.05, 0.06, 0.088, 0.128, 0.15
x_3, Preheating temperature (^{0}C)	: 315^{0}C, 350^{0}C, 450^{0}C, 580^{0}C, 650^{0}C

From the experimental results, empirical equation (1) was developed to predict the surface roughness and the significant parameters involved using response surface methodology. From the analysis of variance (ANOVA) and fit and summary test results it has been observed that quadratic model is more significant for the prediction of surface roughness. The second-order model (1) for surface roughness in its transformation state with the transforming equation of each individual variable is:

$$\hat{y} = -1.55 - 0.11x_1 + 0.25x_2 + 0.056x_3 - 0.03x_2^2 + 0.085x_3^2 + 0.052x_1x_2 + 0.16x_1x_3 - 0.068x_2x_3 \quad (1)$$

$$x_1 = \frac{\ln V - \ln 70}{\ln 126 - \ln 70};$$

$$x_2 = \frac{\ln f_z - \ln 0.088}{\ln 0.128 - \ln 0.088};$$

$$x_3 = \frac{\ln \theta - \ln 450}{\ln 580 - \ln 450}$$

4.0 ARTIFICIAL NEURAL NETWORK DESIGN

Supervised neural network was developed in this study for the prediction of surface roughness in end milling process and its performance was tested. The network was back

propagation neural network (BP) with log-sigmoid transfer function in hidden layers and linear transfer functions in the output layers. The neural network architecture used in this study is shown in Fig. 3. It was designed using MATLAB Neural Network Toolbox [10]. The network consists of input layer, two hidden and one output layers. Hidden layers have 15 neurons each, whereas input and output layers have three and one neurons, respectively. Neurons in the input layers correspond to cutting speed (V), feed (f_z) and preheated temperature (θ). Output layer corresponds to surface roughness (R_a).The developed RSM model based on design of experiment for the prediction of surface roughness are coupled with the ANN model for the data generation. Since only a limited number of experiments are representative of the feasible parameter space, it is important that the ANN realizes each set fully [11]. All the data sets are taken with in the ranges of -1 to +1 for feasible parameter space.

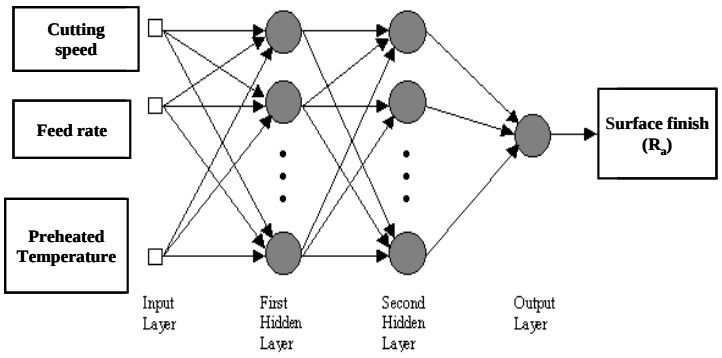

Fig.3 ANN architecture designed

4.1 ANN Model Development: *Training the ANN model*

Before the ANN can be trained and mapping learned, the experimental data was processed into patterns. So Training, validation and testing pattern vector had been formed before the ANN was trained. Each pattern was formed with an input condition vector,

$$Input_i = \begin{bmatrix} CuttingSpeed \\ FeedRate \\ \Pr eheated\_Temperature \end{bmatrix}$$

And the corresponding target vector,

$$Target_i = [SurfaceRoughness]$$

The back-propagation learning algorithm was used for training the network. For training the network, the TRAINLM function of MATLAB was utilized which works on back propagation algorithm [11]. These algorithms iteratively adjust the weights to reduce the error between the experimental and predicted outputs of the network. The 14 experimental results and further 56 generated results from the RSM model were used for this training, prediction and validation of the model. TRAINLM updates weights so as to minimize the mean square error (MSE) between the network prediction and training data set. When the network training was successfully finished, the network was tested with additional test data.

5. SIMULATED RESULTS OF DEVELOPED ANN MODEL

The developed ANN model can predict surface roughness based on the cutting conditions, with a high degree of accuracy within the scope of cutting conditions investigated in the study. Hence, the influence of the cutting conditions on the surface roughness can be studied using the model.

Effect of Cutting parameters on Surface Roughness

Cutting speed is one of the most important cutting parameters in metal-cutting operations and it is very influential on surface roughness as shown in Fig 4. At a very low cutting speed it has an adverse effect on surface finish, but after a certain speed the surface finish improves with increase of cutting speed.

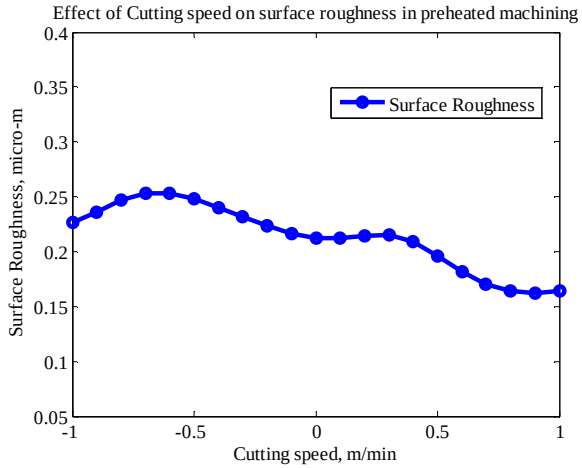

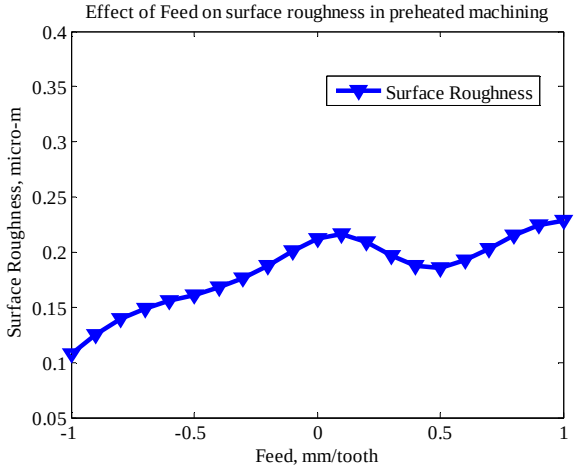

Fig.4 Cutting speed effect on surface roughness **Fig.5 Feed effect on surface roughness**

Feed plays a dominant role on surface finish as shown in the Fig 5. At very low feed it has a sharp adverse effect on surface roughness until a certain feed value. After that surface finish remains somewhat almost constant with feed. But at even higher feed it again affects surface roughness.

.

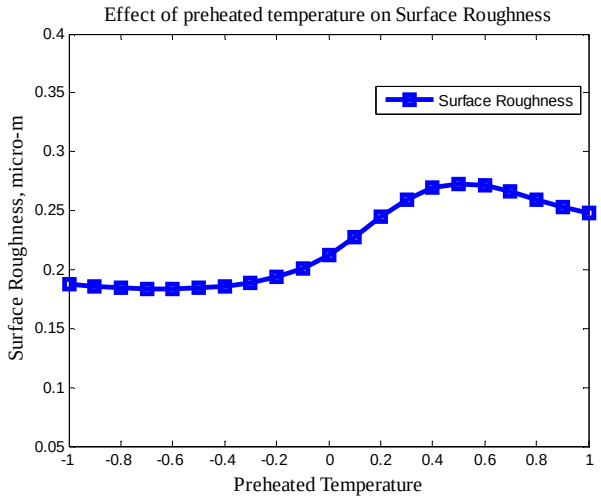

Fig.6 Simulation of surface roughness at varying preheated temperature.

Preheated temperature has a small effect on surface roughness as shown in Fig.6. Initially at a very low preheated temperature, it does not have any significant effect on surface roughness. But after certain increases in preheated temperature the surface roughness increases and then again with the further increase the surface roughness shows little improvement

6. CONCLUSIONS

The multilayer network with two hidden layers having 15 'log-sigmoid' neurons trained with TRAINLM algorithm was found to be the optimum network for the model developed in this study. From the model it has been observed that increase in feed and preheated temperature increase the surface roughness whereas increase of cutting speed shows improvement of surface roughness. This developed ANN model can now be used to analysis and predict the surface roughness for different cutting conditions while end milling of Ti6Al4V alloy in preheated machining.

7. REFERENCES

[1] I.A Choudhury, M.A. El-Baradie, 'Machinability assessment of Inconel 718 by factorial design of experiment coupled with response surface methodology', Journal of Material Processing and Technology 95, pp. 30 – 39, 1999.

[2] M. Alauddin, M.A. El Baradie, M.S.J Hashmi, Computer-aided analysis of a surface-roughness model for end milling, J. Mater. Process. Technol. 55(1995) 123-127.

[3] K.H. Fuh, R.M. Hwang, Predicted milling force model for high-speed end milling operation, Int. J. Mach. Tools Manuf. 37 (7) (1997) 969-979.

[4] R.M. Sundaram and B.K. Lambert , Mathematical models to predict surface finish in fine turning of steel, Part I. International Journal of Production Research 19 (1981), pp. 547–556

[5] R.M. Sundaram and B.K. Lambert , Mathematical models to predict surface finish in fine turning of steel, Part II. International Journal of Production Research 19 (1981), pp. 557–564

[6] D.E. Dimla Sr., Application of perceptron neural networks to tool-state classification in a metal-turning operation, Eng. Appl. Artif. Intell. 12 (1999) 471-477.

[7] H. Z. Li, H. Zeng, X. Q. Chen, An experimental study of tool wear and cutting force variation in the end milling of Inconel 718 with coated carbide inserts,2006, Journal of Materials Processing Technology, 180 (2006) 296-304.

[8] Sandvik Coromant, MetalCutting Technical guide, AB Sandvik Coromant 2005.10, Printed in Sweden by Elanders.

[9] L.H. Tsoukalas, R.E. Uhrig, Fuzzy and Neural Approaches in Engineering, 1997, pp. 191-288.

[10] MathWorks Incorporation (2007) MATLAB user manual version 7.4.0 (R2007a). MathWorks Incorporation, Natick, MA.

[11] L.H. Tsoukalas, R.E. Uhrig, Fuzzy and Neural Approaches in Engineering, 1997, pp. 191-288.

Proceedings of the 4th BSME-ASME International Conference on Thermal Engineering
27-29 December, 2008, Dhaka, Bangladesh

VARIATION OF FRICTION COEFFICIENT WITH DURATION OF RUBBING AND NORMAL LOAD FOR DIFFERENT MATERIALS

D. M. Nuruzzaman*, M. A Chowdhury and M. L. Rahaman

Department of Mechanical Engineering
Dhaka University of Engineering and Technology, Gazipur, Gazipur-1700, Bangladesh
*e-mail: dewan052005@yahoo.com, lutfar57@yahoo.com

ABSTRACT

The present paper reports the effect of duration of rubbing on friction coefficient for different materials. Variations of friction coefficient and wear rate with the normal load are also investigated experimentally when stainless steel (SS 304) pin slides on different types of materials such as cloth reinforced ebonite (commercially known as gear fiber), glass fiber reinforced plastic (glass fiber), nylon and polytetrafluoroethylene (PTFE). To do so, a pin on disc apparatus is designed and fabricated. During experiment, the rpm of test samples was kept constant. Studies have shown that the values of friction coefficient depend on applied load and duration of rubbing. It is observed that the values of friction coefficient decrease and wear rate increases with the increase of normal load for glass fiber, nylon and PTFE. The different trends are observed for gear fiber i.e. the coefficient of friction and wear rate of gear fiber increase with the increase of normal load. The magnitudes of friction coefficient and wear rate are different for different materials.

Keywords: *Friction Coefficient, Duration of Rubbing, Normal Load, Wear Rate.*

1. INTRODUCTION

Numerous investigations have been carried out on friction and wear of different materials under different operating conditions. Several researchers [1-3] observed that the friction force and wear rate depend on roughness of the rubbing surfaces, relative motion, type of material, temperature, normal force, relative humidity, vibration etc. There have been also a number of investigations exploring the influence of test conditions, contact geometry and environment on the friction and wear behavior of polymers. Tanaka [4] and Bahadur and Tabor [5] have reported that the tribological behavior of polyamide, high density polyethylene (HDPE) and composites is greatly affected by normal load, sliding speed and temperature. This is because polymers are extensively used in sliding/rolling components such as gears and cams where their self lubricating properties are exploited to avoid the need for oil or grease lubrication with its attendant problems of contamination. However, where the contact is there, there is the problem of friction and wear. The friction between polymers can be attributed to two main mechanisms, deformation and adhesion. In this case, the deformation mechanism involves complete dissipation of energy in the contact area while the adhesion component is responsible for the friction of polymer and is a result of breaking of weak bonding forces between polymer chains in the bulk of the material.

Several authors [6-9] observed that the friction coefficient of polymers rubbing against metals decreases with the increase of normal load and sliding velocity though some of

the researchers have different views. Stuart [10] and other researchers [11-13] showed that value of friction coefficient increases with the increase in load. Suresha et al. [14] observed that wear rate increases with the increase of normal load for polymer-metal contact.

To date, investigations on the effects of duration of rubbing and normal load on frictional behavior of different materials such gear fiber, glass fiber, nylon and PTFE are limited. Therefore, in this study an attempt is made to investigate the effect of duration of rubbing and normal load on the friction coefficient of these materials. The relative frictional and wear behavior of these polymers and composite materials are also examined in this study.

2. EXPERIMENTAL

A schematic diagram of the experimental set-up is shown in Fig. 1 i.e. a pin which can slide on a rotating horizontal surface (disc). In this set-up a circular test sample (disc) is to be fixed on a rotating plate (table) having a long vertical shaft clamped with screw from the bottom surface of the rotating plate. The shaft passes through two close-fit bush-bearings which are rigidly fixed with stainless steel plate and stainless steel base such that the shaft can move only axially and any radial movement of the rotating shaft is restrained by the bush. These stainless steel plate and stainless steel base are rigidly fixed with four vertical round bars to provide the rigidity to the main structure of this set-up. The main base of the set-up is constructed by 10 mm thick mild steel plate consisting of 3 mm thick rubber sheet at the upper side and 20 mm thick rubber block at the lower side. A compound V-pulley above the top stainless steel plate was fixed with the shaft to transmit rotation to the shaft from a motor. An electronic speed control unit is used to vary the speed of the motor as required. A 6 mm diameter cylindrical pin (roughness, $R_{a,}$ about 3 μm) whose contacting foot is flat made of stainless steel, fitted on a holder is subsequently fitted with an arm. The arm is pivoted with a separate base in such a way that the arm with the pin holder can rotate vertically and horizontally about the pivot point with very low friction. To measure the frictional force acting on the pin during sliding on the rotating plate, a load cell (TML, Tokyo Sokki Kenkyujo Co. Ltd, CLS-10NA) along with its digital indicator (TML, Tokyo Sokki Kenkyujo Co. Ltd, Model no. TD-93A) was used. The average surface roughness (R_a) of the tested materials such as gear fiber, glass fiber, nylon and PTFE is about 0.7, 0.8, 0.2 and 0.9 μm respectively.

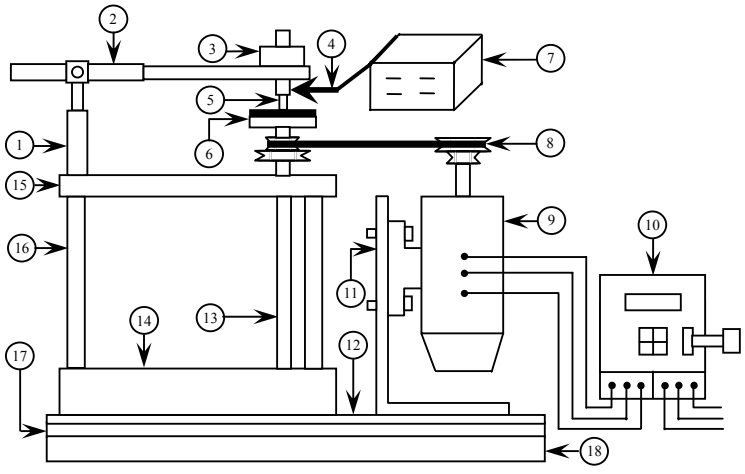

Fig. 1: Block Diagram of the Experimental Set-up

3. RESULTS AND DISCUSSION

Figure 2 shows the variation of friction coefficient with the duration of rubbing at different normal load for gear fiber. During experiment, the sliding velocity and relative humidity were 1 m/s and 70% respectively. Curve 1 of this figure is drawn for normal load 10.0 N. From this curve, it can be seen that during the starting, the value of friction coefficient is 0.038 which remains constant for few minutes then increases very steadily up to 0.042 over a duration of 26 minutes of rubbing and after that it remains constant for the rest of the experimental time. At starting of experiment the friction force is low due to contact between superficial layer of pin and disc. Then the friction coefficient increases due to ploughing effect and because of roughening of the disc surface. Curve 2 of this figure is drawn for normal load 12.5 N and shows similar trend as that of curve 1. Curves 3, 4 and 5 of Fig. 2 are drawn for normal load 15.0, 17.5 and 20 N respectively. It is shown that the slope of the curve 3 is higher than that of curves 1 and 2. From the roughness of the test disc after 30 minutes of rubbing, the higher the normal load, the higher the roughness was obtained. This is the reason for the curve 3 being steeper. Curves 4 and 5 of this figure show similar trend as that of curve 3. The increase in coefficient of friction with the increase of normal load is due to the detachment and removal of worn materials and more contact with reinforced cloth fibers. From these curves, it is also observed that the time to reach steady state value is different for different normal load. It indicates that the higher the normal load, the time to reach constant friction is less. This is because the surface roughness and other parameter attain a steady level at short period with the increase of normal load.

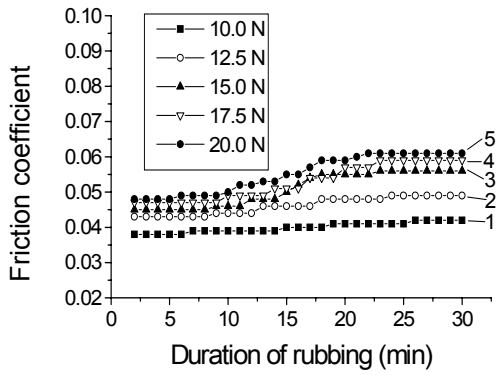

Fig. 2: Friction coefficient as a function of duration of rubbing at different normal load (sliding velocity: 1 m/s, relative humidity: 70%, test sample: gear fiber)

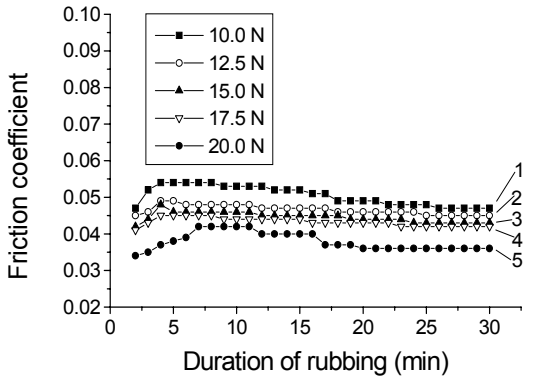

Fig. 3: Friction coefficient as a function of duration of rubbing at different normal load (sliding velocity: 1 m/s, relative humidity: 70%, test sample: glass fiber)

Figure 3 shows the effect of the duration of rubbing on the value of friction coefficient at different normal load for glass fiber at speed of 1 m/s and 70% of relative humidity. Curve 1 of this figure drawn for normal load 10.0 N, shows that during starting of the experiment, the value of friction coefficient is 0.047 which rises for few minutes to a value of 0.054 and then decreases very steadily up to 0.047 over a duration of 26 minutes of rubbing and then it becomes steady for the rest of the experimental time. Almost similar trends of variation are observed in curves 2, 3, 4 and 5 are drawn for load 12.5, 15, 17.5 and 20 N shown respectively. In the first few minutes of rubbing the temperature of test disc and stainless steel pin was about room temperature. The adhesive force between transfer substance and the pin was weak. This causes lower friction force and friction coefficient at

initial stage of running. The temperature of the frictional zone rose with increase of rubbing time. When the adhesive force between pin and transfer substance is quite strong, the transfer substance might settle on the counterface. This incomplete transfer substance had a large resistance to friction and hence the coefficient of friction is high. From these curves, it is found that time to reach constant friction is different for different normal load and higher the normal load, glass fiber takes less time to stabilize.

Figure 4 is drawn to show the variation of friction coefficient with the duration of rubbing at different normal load for nylon. Curve 1 of Fig. 4 is drawn for 10.0 N shows that during starting of the running-in, the value of friction coefficient is 0.077 which increases for few minutes to a value of 0.092 and then decreases almost linearly up to 0.08 over a duration of 26 minutes of rubbing and after that it remains constant for the rest of the experimental time. Similar trends of variation are observed for normal load 12.5, 15, 17.5 and 20 N which are shown in curves 2, 3, 4 and 5 respectively. In the first few minutes (about 8 min) the frictional heat is very low. The adhesive force between transfer substance and stainless steel pin was quite small and transfer film could not form. So the stainless steel pin contacts directly to the nylon disc. During first few minutes the coefficient of friction was small, after that the temperature of the rubbing zone rose with time. When the adhesive force of the transfer substance to the pin was adequately strong, the transfer substance might settle on the pin to form transfer film. The transfer film is formed gradually and difficult to destroy and therefore higher values of friction coefficient are obtained. When the transfer film formed completely, then the friction occurred between the nylon disc and transfer film of nylon. As a result, the coefficient of friction gradually decreases and after sometime it becomes steady.

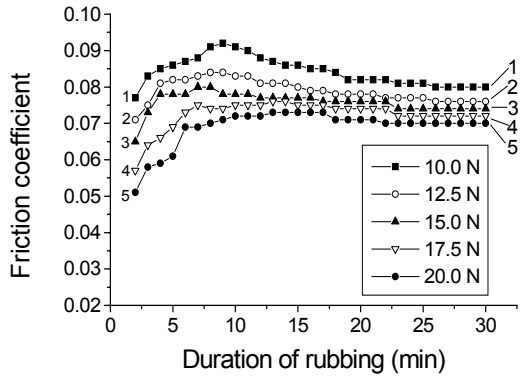

Fig. 4: Friction coefficient as a function of duration of rubbing at different normal load (sliding velocity: 1 m/s, relative humidity: 70%, test sample: nylon)

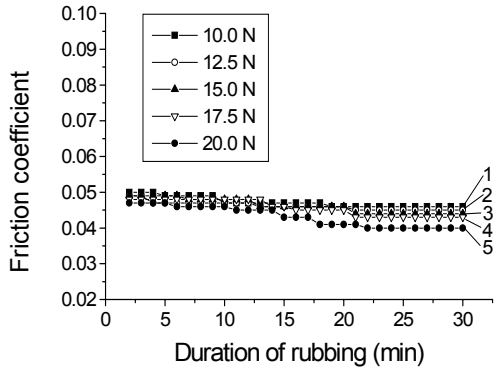

Fig. 5: Friction coefficient as a function of duration of rubbing at different normal load (sliding velocity: 1 m/s, relative humidity: 70%, test sample: PTFE)

Several experiments are conducted to observe the effect of duration of rubbing on friction coefficient under different normal load for PTFE. These results are shown in Fig. 5. Curve 1 of this figure drawn for normal load 10.0 N shows that during the starting, the value of friction coefficient is 0.050 which decreases almost linearly up to 0.046 over a duration of 19 minutes of rubbing and after that it remains constant for the rest of the experimental time. Curves 2, 3, 4 and 5 of this figure are drawn for normal load 12.5, 15, 17.5 and 20 N, respectively. These curves also show similar trend as that of curve 1. Due to low adhesion of PTFE surface at the beginning of rubbing the steel pin may easily detached the PTFE layer and therefore the contact is between PTFE and pin. This might be the reason for high friction at the start of rubbing. The strong adhesions that are formed across the interface initiate the formation of a thin, coherent transfer film of PTFE on the pin. This results in subsequent

contact between PTFE and transfer film of PTFE on pin and easy sliding, hence the coefficient of friction is low.

Figure 6 shows comparison of the variation of friction coefficient with normal load for above said materials. Curves 1, 2, 3 and 4 of this figure are drawn for gear fiber, glass fiber, nylon and PTFE respectively. It is shown that the friction coefficient varies from 0.046 to 0.034, 0.046 to 0.04 and 0.08 to 0.069 with the variation of normal load from 10 to 20 N for glass fiber, PTFE and nylon respectively. These results show that friction coefficient decreases with the increase of normal load. Different behavior is observed for gear fiber in comparison with other tested materials, that is, friction coefficient of gear fiber increases almost linearly from 0.04 to 0.061 with the increase of normal load from 10 to 20 N. This might be due to high ploughing, surface damage and breakage of reinforced fibers.

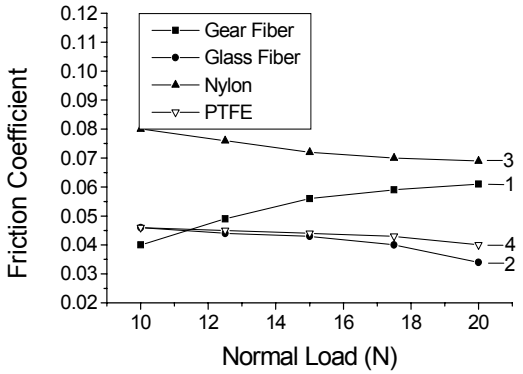

Fig. 6: Friction coefficient as a function of normal load for different materials (sliding velocity: 1 m/s, relative humidity: 70%)

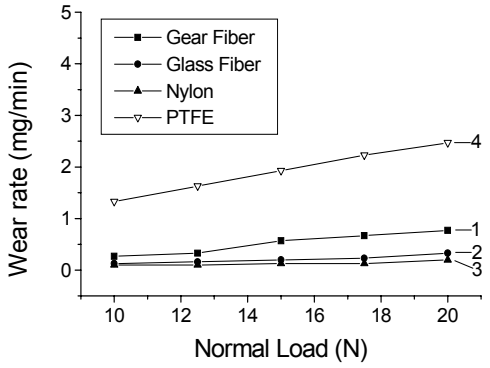

Fig. 7: Wear rate as a function of normal load for different materials (sliding velocity: 1 m/s, relative humidity: 70%)

Variations of wear rate with normal load for gear fiber, glass fiber, nylon and PTFE are presented in Fig. 7. The experimental results indicate that the curves drawn showing the variation of wear rate from 1.33 to 2.47, 0.27 to 0.77, 0.13 to 0.33 and 0.1 to 0.2 mg/min with the variation of normal load from 10 to 20 N for PTFE, gear fiber, glass fiber and nylon respectively. From these curves, it is observed that wear rate increases with the increase of normal load for all types of materials investigated. The shear force and frictional thrust are increased with increase of applied load and these increased values accelerate the wear rate. Figure 7 also shows the comparison of the variation of wear rate with normal load for gear fiber, glass fiber, nylon and PTFE. Wear rate of PTFE shows the highest and nylon shows the lowest value among these materials. For composite materials, the values of wear rate are higher for gear fiber compared to the values of glass fiber. For plastic materials, higher values are observed for PTFE compared to nylon.

4. CONCLUSION

The followings can be concluded from this study:

1. Friction coefficient varies with duration of rubbing and normal load and this variation is different for different materials. In general, after 20 minutes of rubbing, the friction coefficient reached steady value for all types of tested materials.
2. The coefficient of friction decreases with increase of load for glass fiber, PTFE and nylon while the coefficient of friction increases with increase of normal load for gear fiber.

3. Nylon has the highest and glass fiber has the lowest friction coefficient except at normal load 10.0 N. When applied load is 10.0 N, the lowest friction is for gear fiber. The friction coefficient of gear fiber is higher than PTFE and lower than nylon.
4. Wear rate increases with increase of load for all types of tested materials. Wear rate of PTFE bears the highest and nylon bears the lowest value among these materials.

REFERENCES

[1] Archard, J. F., Wear Theory and Mechanisms, Wear Control Handbook, ASME, New York, 1980.

[2] Tabor, D., Friction and Wear – Developments Over the Last 50 Years, Keynote Address, Proceedings, International Conference of Tribology – Friction, Lubrication and Wear, 50 Years On, London, Inst. Mech. Eng., 1987, pp. 157-172.

[3] Chowdhury, M. A., and Helali, M. M., The effect of amplitude of vibration on the coefficient of friction for different materials, Tribology International, 41(2008), 4, pp. 307 – 314.

[4] Tanaka, K., Transfer of Semicrystalline Polymers Sliding Against Smooth Steel Surface, Wear, 75 (1982), pp.183 – 199.

[5] Bahadur, S., Tabor, D., Role of fillers in the friction and wear behavior of high-density polyethylene. In: Lee LH, editor. Polymer wear and its control. ACS Symposium Series, Washington DC, 1985, 287, pp. 253–68.

[6] Sirong, Yu, Zhongzhen, Yu, Yiu-Wing, Mai, Effects of SEBS-g-MA on tribological behavior of nylon 66/organoclay nanocomposites. Tribology International, 40 (2007), pp. 855-862.

[7] Bratcu, O., Tomescu, L., and Bologa, O., Tribological Behavior of PTFE+Glass Fiber Composites Used for Axial Bearings, Under Water Lubrication, The Annals of University "DUNAREA DE JOS' of Galati, Fascicle VIII (2002), Tribology, ISSN 1221-4590, pp. 65 – 69.

[8] Unal, H., Mimaroglu, A., Kadioglu, U., and Ekiz, H., Sliding Friction and Wear Behavior of Polytetrafluoroethylene and its Composites under Dry Conditions, Materials and design, 25 (2004), pp. 239 – 245.

[9] Mimaroglu, A., Unal, H., and Arda, T., Friction and Wear Performance of Pure and Glass Fiber Reinforced Poly-Ether-Imide on Polymer and steel Counterface Materials, Wear, 262 (2007), pp. 1407 – 1413.

[10] Stuart, B. H., Tribological studies of poly(ether ether ketone) blends, Tribology International, 31 (1998), 11, pp. 647–51.

[11] Unal, H., Mimaroglu, A., Influence of test conditions on the tribological properties of polymers, Industrial Lubrication and Tribology, 55 (2003), 4, pp. 178–83.

[12] Unal, H., Mimaroglu, A., Friction and wear behavior of unfilled engineering thermoplastics, Material Design, 24 (2003), pp. 183–7.

[13] Suresha, B., Chandramohan, G., Prakash, J.N., Balusamy, V., and Sankaranarayanasamy, K., The role of fillers on friction and slide wear characteristics in Glass-Epoxy composite systems. Journal of Minerals & Materials Characterization & Engineering, 5 (2006), 1, pp. 87 – 101.

[14] Suresha, B., Chandramohan, G., Samapthkumaran, P., Seetharamu, S., and Vynatheya, S., Friction and wear characteristics of Carbon-Epoxy and Glass-Epoxy woven roving Fiber composites, Journal of Reinforced Plastics and Composites, 25 (2006), pp. 771-782.

Proceedings of the 4th BSME-ASME International Conference on Thermal Engineering
27-29 December, 2008, Dhaka, Bangladesh

UNIFIED MATERIAL PARAMETERS FOR 429EM STAINLESS STEEL AT ELEVATED TEMPERATURE IN TERMS OF 'CHABOCHE MODEL' AND 'MODIFIED OVERLAY MODEL'.

S M Humayun Kabir , Sang- Ho Kim , Tae-In Yeo

School of Mechanical and Automotive Engg., University of Ulsan.
P.O Box18 Ulsan 680-749, Republic of Korea.
E-mail : humayun@mail.ulsan.ac.kr

Abstract

Identifying the parameters to find the stabilized hysteresis loop in an elasto-plastic steel behavior, is an important step concerning low cycle fatigue life studies at elevated temperature. The present work is concerned with the determination of unified material parameters for 429EM Stainless Steel at elevated temperature of 200^0C using the Chaboche model [1] and the Modified Overlay model [2] of cyclic plasticity. The parameters are calibrated using uniaxial cyclic experimental stabilized loop from [2]. Utilizing the determined material parameters in the considered elasto-plastic constitutive models, attempts are made to simulate the stabilized hysteresis loops in FE (finite element) code ABAQUS by means of user-defined material subroutine called UMAT for the strain range of 1.4%. The stabilized hysteresis cycles obtained by the analysis with considered models are in good harmony with that of experiment.

Keywords: *Cyclic hardening; Stabilized hysteresis loops; Chaboche model; Overlay model; Material parameters for elasto-plastic behavior.*

1. Introduction

During routine operation, many automotive engine components experience high temperature changes nearly up to 800^0C generally. These temperature differences in conjunction with structural constraint can cause stresses to develop in addition to those caused by normal operating loads. Due to high thermal fatigue resistance as well as excellent corrosion resistance of ferritic stainless steel, it is commonly used in the exhaust systems of automobile engines besides many high temperature structures [4]. So the material parameters and mechanical properties of 429EM steel in elasto-plastic behavior have been the object of many studies during recent years. We focus on the study of the two models and determination of unified material parameters for the 429EM steel at 200^0C.

The literature on the subject matter is vast and during the past three decades enormous progress has been accomplished in the development of constitutive equations to represent the inelastic behavior of various materials, under uniaxial and multiaxial cyclic loading at isothermal and anisothermal conditions. For time-independent plasticity, a set of internal-variables of thermodynamical concepts has been studied under many different ways in order to generalize the classical isotropic and kinematic theories [1]. This includes the use of multiyield surfaces by Mroz [5] and the 'nonlinear kinematic rule' which is in terms of differential equation initially proposed by Armstrong & Frederick [6], developed further and intensively used by Chaboche [1, 7]. Furthermore, the overlay model was proposed by Iwan [8] and generalized by Chiang [9]. And later Yoon et. al. [2] modified the overlay model to consider the characteristics in the cyclic deformation behavior of Non-Masing material and strain range dependency.

In this paper we study two different material models: one is the Combined Nonlinear Isotropic and Kinematic Hardening model which is often referred to as Chaboche model [1] and the other one is the Modified Overlay model [2]. Then the unified material parameters are determined from the available experimental material data obtained from [2, 3] in terms of the above considered models. The parameters are unified because we correlate the above two models during the determination of parameters, and hence a common set of parameters results between each set of parameters for each individual model. We integrate these models using the implicit integration scheme. Finally these models are implemented in the commercial FE code ABAQUS through UMAT subroutine [10] with the determined parameters, and stabilized hysteresis loops from the simulations are compared to experimental stabilized hysteresis loop for the strange range $(\Delta\boldsymbol{\varepsilon})$ of 1.4% at 200^0 C .

2. Description of the Constitutive Models

The description of time-independent plasticity constitutive equations in order to model Von Mises elastoplasticity combined with non-linear isotropic and kinematic hardening can be found elsewhere. For example, [1] , [6], and [7]. We will not elaborate on these details here. Similarly, [2] and [8] for the Overlay model.

2.1. Combined Nonlinear Isotropic and Kinematic Hardening Model

The constitutive model considered here is based on the yield criterion of Von Mises, the non-linear isotropic hardening law and the non-linear kinematic hardening law of Chaboche [1, 7], and the normality hypothesis with the associated flow rule of plasticity theory. A brief summery of the resulting set of equations is,

1. Yield function: $f = \boldsymbol{J}_2(\boldsymbol{\sigma} - \boldsymbol{x}) - \sigma_y(p) = 0$
2. Size of the surface: $\sigma_y(p) = \sigma_{y0} + r(p)$
3. Effective stress: $\sigma_e = \boldsymbol{J}_2 = \sqrt{\frac{3}{2}(\boldsymbol{\sigma}' - \boldsymbol{x}') : (\boldsymbol{\sigma}' - \boldsymbol{x}')}$ (1)
4. Flow rule: $d\boldsymbol{\varepsilon}^p = d\lambda \frac{\partial f}{\partial \boldsymbol{\sigma}}$
5. Plastic multiplier: $d\lambda = \frac{H(f)}{h} \left\langle \frac{3}{2} \frac{\partial f}{\partial \boldsymbol{\sigma}} : d\boldsymbol{\sigma} \right\rangle$

where f : yield function, $\boldsymbol{\sigma}$: stress tensor, $\boldsymbol{x}$:back stress tensor, $\boldsymbol{\sigma}'$: deviatoric stress tensor, $\boldsymbol{x}'$:deviatoric back stress tensor, $\boldsymbol{J}_2(\boldsymbol{\sigma} - \boldsymbol{x})$:second invariant of deviatoric stress, $\boldsymbol{\varepsilon}^p$: plastic strain tensor, $d\boldsymbol{\varepsilon}^p$: Increment in plastic strain, h : hardening modulus, r : Isotropic hardening function, σ_{y0} : initial size of the surface with $r(0) = 0$, p : accumulated plastic strain, $H(f)$: Heaviside function, G, λ :lame constants.

The evolution of the back stress $\boldsymbol{x}$ in kinematic hardening and the internal stress r can be written in their simplest form as [1],

$$d\boldsymbol{x} = \frac{2}{3} C d\boldsymbol{\varepsilon}^p - \gamma \boldsymbol{x} dp \quad (2)$$

$$dr = b(Q - r)dp \quad (3)$$

where C and γ are temperature dependent material parameters describing the kinematic hardening . Q is the saturation value of r and b controls the pace of the isotropic hardening. There are six material parameters involved regarding combined nonlinear isotropic and kinematic hardening model E, C, γ, Q, b and σ_{y0} whose values are calibrated in section 3 integrated with the Modified Overlay model parameters at 200^0C.

2.2.1. Overlay Model

The Overlay model is based on the assumption that the material is composed of a series of Jenkin's element connected in parallel and each element consists of a linear spring with stiffness E_i in series with a slip element of strength k_i. Each element is therefore an ideal elasto-plastic unit [8]. The yield function of the sub-elements can be given as,

$$f_i = \boldsymbol{J}_2(\tilde{\boldsymbol{\sigma}}_i) - k_i \tag{4}$$

where k_i is the yield stress of the ith sub-element. Macroscopic stress is,

$$\boldsymbol{\sigma} = \sum_{i=1}^{N} \phi_i \tilde{\boldsymbol{\sigma}}_i \tag{5}$$

where $\tilde{\boldsymbol{\sigma}}_i$ and ϕ_i defines the applied stress and fraction of ith sub-element. When the number of elements becomes very large the distribution function ϕ can be considered as a continuous function of a variable k and macroscopic stress can be defined as,

$$\boldsymbol{\sigma} = \int_0^{\infty} \phi(k)\tilde{\boldsymbol{\sigma}}(\varepsilon, k)\,\mathrm{d}\,k \tag{6}$$

To evaluate the discrete distribution of elements, the tensile curve was divided into several linear segments to minimize the difference between a multi-linear curve and actual curve. The stiffness of the multi-linear curve is related with the sum of yield fraction ϕ which is defined as,

$$\frac{\sigma_{i+1} - \sigma_i}{\varepsilon_{i+1} - \varepsilon_i} = \left(1 - \sum_{j=1}^{i} \phi_j\right) E \tag{7}$$

2.2.2. Modified Overlay Model

To take into account the non-Masing's behavior of material and strain range dependency Overlay model was modified [2]. The yield stress is divided as follows,

$$k_i = m_i + R\left(\Delta\varepsilon, p\right) \tag{8}$$

where m_i describes the master curve and $R\left(\Delta\varepsilon, p\right)$ represents the change of elastic limit which depends on the strain range $(\Delta\varepsilon)$ and previous history. When a few points $\left(\varepsilon_i, \sigma_i\right)$ are selected to represents the master curve, the m_i and ϕ_i of each sub-element can be calculated through the following equations,

$$\phi_i = \frac{1}{E}\left(\frac{\sigma_i - \sigma_{i-1}}{\varepsilon_i - \varepsilon_{i-1}} - \frac{\sigma_{i+1} - \sigma_i}{\varepsilon_{i+1} - \varepsilon_i}\right) \tag{9}$$

$$m_i = E\varepsilon_i / 2 \tag{10}$$

and the evolution law of the elastic limit for cyclic hardening is,

$$R = R_0 + (R_{st} - R_0)\,[1 - \sum_{i}^{N} a_i\ \exp(-b_i\ p)] \tag{11}$$

where R_0 is the minimum elastic limit and R_{st} is the elastic limit of the stabilized hysteresis loop. $m_i, \phi_i, R_0, R_{st}, a_i, b_i$ and E are material parameters to be determined.

3. Material Parameters Determination for 429EM Steel

The stabilized cyclic behavior of a material is of particular interest in low cycle fatigue life prediction since the crack initiation prediction is generally based on it [1]. The plastic parameters are determined using optimum technique with the available cyclic test data from [2, 3] at isothermal condition of 200^0C.

Fig.1 and Fig.2 show the experimental stabilized hysteresis loop (σ-ε) and stress amplitude versus accumulated plastic strain ($\Delta\sigma$ - p) from [2, 3] respectively. The evolution of r in Eq. $(1)_2$ is related to the stress amplitude ($\Delta\sigma$) during cyclic test as follows [1],

$$\frac{\Delta\sigma-\Delta\sigma_{\min}}{\Delta\sigma_{st}-\Delta\sigma_{\min}}\cong\frac{r}{Q}=1-e^{-bp} \tag{12}$$

where $\Delta\sigma_{st}$ and $\Delta\sigma_{\min}$ are the stress amplitude for the stabilize cycle and first cycle respectively and $\Delta\sigma$ is the stress amplitude in between. And from the evolution of R in Eq. (11), we can define the hardening ratio as,

$$H\cdot R.=\frac{\Delta\sigma-\Delta\sigma_{\min}}{\Delta\sigma_{st}-\Delta\sigma_{\min}}=\frac{R-R_0}{R_{st}-R_0} \tag{13}$$

Q and b are easily obtained from whole history data of Eqs.$(1)_2$,(12) and (13) in conjunction with nonlinear regression procedure. The Young's modulus E and R_{st} are derived directly from the linear part of the stabilized hysteresis loop. Making the correlation between Eq.(12) and Eq.(13) R_0 is evaluated in such a way so that it can meet the first inelastic flow, and simultaneously we use the same magnitude for σ_{y0} as of R_0. Then material parameters m_i's and ϕ_i's are computed from experimental stabilized loop data by means of Eq.(9) and Eq.(10) . To determine m_i, we divide the nonlinear part of the upper branch of the stabilized hysteresis loop into six linear segments that minimize the difference between the original curve and the multi-linear curve. Therefore the numbers of sub-elements used in this paper for the Modified Overlay model is six.

Utilizing stabilized hysteresis loop data with the built-in calibration procedure of the ABAQUS code, C and γ are determined. The experimental curve of stress versus plastic strain is obtained directly from the stabilized loop and the experimental kinematic hardening (x) is extracted by translation of the plastic curve as shown in Fig.3. Then considering the first data pair $(\varepsilon_1^p,\sigma_1)$ with $\varepsilon_1^p=0$, integration of Eq.(2) gives [10],

$$x=\frac{C}{\gamma}(1-e^{-\gamma.\varepsilon^p})+x_1e^{-\gamma.\varepsilon^p} \tag{14}$$

which is used to calibrate the parameters C and γ. All calculated unified parameters for the 429EM steel are listed in the Tables 1-2. The parameters which are determined and listed in the Tables 1-2 are unified because parameters are optimized in such a way so that the first

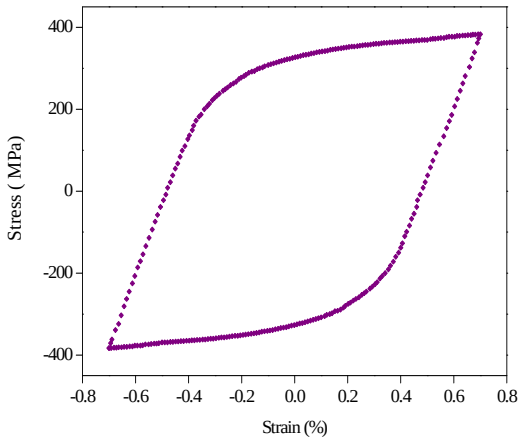

Fig. 1. Experiment stabilized hysteresis loop from [2] at $\Delta\varepsilon$ = 1.4 % .

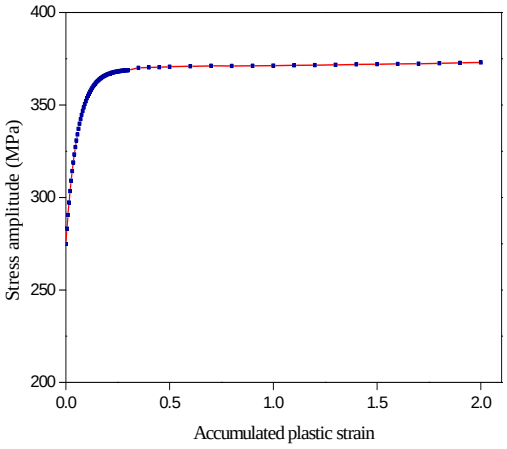

Fig. 2. Stress amplitude-accumulated plastic strain curve from [3].

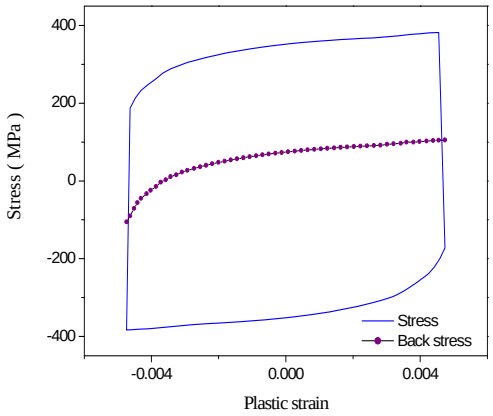

Fig. 3. Back stress derived from stabilized hysteresis loop.

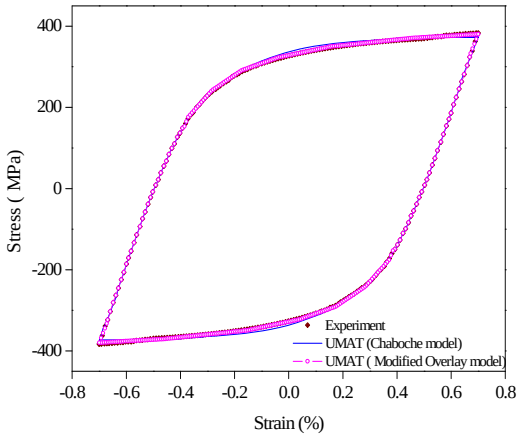

Fig. 4. Comparisons of stabilized hysteresis loops from UMAT results and experiment.

three parameters for each model remain the same, hence reduce the complication of parameters between the Chaboche model and the Modified Overlay model.

4. FE Modeling and Results

Cyclic plasticity equations for modeling inelastic material behavior are generally given in rate form for capturing history dependence behavior, thus requiring numerical integration for implementation in the finite element program ABAQUS. An algorithm for implementation of the combined hardening has been proposed by Doghri [11] and modified by Mahnken [12], whereby discretized rate equation reduced to one-dimensional problem. In this implicit scheme only plastic multiplier appears to be unknown. We combine the Bisection method with Newton-Rhapson iteration for better convergence in iterative procedure. The formulation for Combined Nonlinear Isotropic and Kinematic Hardening model and modified Overlay model have been implemented in ABAQUS by means of a UMAT subroutine using the already determined parameters. In finite element technique strain driven approach of implicit return mapping-type algorithm [13] has been implemented through UMAT subroutine.

Table. 1
Parameters of 429EM steel at 200^{0}C for the Combined Nonlinear model $(\Delta\varepsilon/2 = 0.7\%)$**.**

E (GPa)	σ_{y0} (MPa)	b	Q (MPa)	C (MPa)	γ
169.22	179.45	15.69	98.06	55982.20	605.68

Table. 2
Material parameters of 429EM steel at 200^{0}C for the Modified Overlay model $(\Delta\varepsilon/2 = 0.7\%)$**.**

E (GPa)	R_0 (MPa)	b	a	R_{st} (MPa)
169.22	179.45	15.69	1.0	277.51

m_0 (MPa)	m_1 (MPa)	m_2 (MPa)	m_3 (MPa)	m_4 (MPa)	m_5 (MPa)	m_6 (MPa)
0.0	107.82	231.70	377.94	563.61	847.95	1372.41
ϕ_0	ϕ_1	ϕ_2	ϕ_3	ϕ_4	ϕ_5	ϕ_6
0.7034	0.0970	0.0656	0.0576	0.0445	0.0251	0.0069

The experimental result of stabilized hysteresis loop together with UMAT results for the Chaboche model and the Modified Overlay model is demonstrated in Fig.4. It shows that the stabilized loop from the ABAQUS UMAT for the considered models are in good agreement with the experimental results using the determined material parameters. Without compromising accuracy and sacrificing the larger memory required for analysis, we choose six sub-elements in the modified Overlay model compared to five sub-elements in [2], and subsequently we determine the material parameters. And calculated parameters in this work regarding modified Overlay model are fairly different than parameters given in [2]. But still UMAT results using this new parameter set strongly follow the experimental stabilized hysteresis loop in case of the Modified Overlay model. The determined parameters are unified because we show that simulated stabilized hysteresis loops for the above two models closely follow the experimental stabilized hysteresis loop using some common parameters among all calibrated parameters.

5. Conclusion

Unified material parameters of 429EM Stainless Steel at 200^0C are determined in terms of two well-known plasticity models with different hardening rules – the Combined Nonlinear Isotropic and Kinematic Hardening model and the Modified Overlay model - via calibration using the experimental data. The values of the parameters listed in each table need to be understood as a group and any single value may be meaningless individually. These calibrated parameters are reasonable because by using these parameters it shows that stabilized hysteresis loops from ABAQUS UMAT for the considered models have good correlation with the experimental stabilized hysteresis loop.

References

[1] Chaboche J.L., Time-independent constitutive theories for cyclic plasticity, *Int. J. Plasticity*, 2(2) (1986) , pp. 149–188.

[2] Yoon, S., Hong, S.G. and Lee, S.B., Phenomenological description of cyclic deformation using the overlay Model, *Mat Sci and Engg*., A364 (2004), pp. 17-26.

[3] Yoon, S., Inelastic analysis and life prediction for structures subject to thermomechanical loading, Ph.D Thesis, KAIST, South Korea, 2003

[4] Beddos, J. and Parr, J.G., Introduction to stainless steels, 3rd ed., ASM Intl.,1998.

[5] Mroz, Z., On the description of anisotropic work hardening, *J. Mech. Phys. Solids*. 15 (1967), pp.163-175.

[6] Lemaitre, J. and Chaboche, J.L., Mechanics of Solid Materials, Cambridge University, Cambridge, 1990.

[7] Chaboche J.L., Constitutive equations for cyclic plasticity & cyclic viscoplasticity, *Int. J. Plasticity* , 5 (1986), pp. 247–302.

[8] Iwan, W.D., A distributed-element model for hysteresis and it's steady-state dynamic response, *J. Appl. Mech.*, (1966), pp. 893-900.

[9] Chiang, D.Y. and Beck, J.L., A new class of distributed-element models for cyclic plasticity, *Int. J. Solids Structures*, 31 (1994), pp. 469-484.

[10] Hibbitt, Karlsson and Sorensen, ABAQUS Version 6.6., 2006

[11] Doghri I., Fully implicit integration and consistent tangent modulus in elasto-plasticity, *Int. J. Numer. Meth. Eng*., 36 (1993), pp. 3915–3932.

[12] Mahnken, R., Improved implementation of an algorithm for nonlinear isotropic – kinematic hardening , *Commun. Numer. Meth. Eng.* , 15 (1999), pp. 745-754

[13] Dunne, F and Petrinic, N., Introduction to computational plasticity. Oxford University Press, 2005.

Proceedings of the 4th BSME-ASME International Conference on Thermal Engineering
27-29 December, 2008, Dhaka, Bangladesh

INFLUENCE OF FREQUENCY AND DIRECTION OF VIBRATION ON THE COEFFICIENT OF FRICTION OF ALUMINUM

M. A Chowdhury*, D. M. Nuruzzaman and M. L. Rahaman

Department of Mechanical Engineering
Dhaka University of Engineering and Technology, Gazipur, Gazipur-1700, Bangladesh
*email: asadzmn2003@yahoo.com, lutfar57@yahoo.com

ABSTRACT

This work examines how coefficient of friction is affected by the frequency of vibration. Variation of coefficient of friction with the variation of frequency of vibration along and perpendicular to the direction of sliding velocity is investigated experimentally on an aluminum disc sliding against stainless steel pin using specially designed pin-on-disc apparatus having facility of vibrating the disc at different frequency, direction and amplitude of vibration. RMS roughness of aluminum test sample was 0.60 microns and relative humidity was 60%. The value of coefficient of friction increases with the increase of frequency of vibration. Studies have also shown that the increasing rate of friction coefficient with the increase of frequency of vibration for vibration along the direction of sliding velocity is higher than that for vibration perpendicular to the direction of sliding velocity. It is also observed that the rate of reduction or increment of coefficient of friction has a particular relationship on the frequency and direction of vibration.

Keywords: *Coefficient of friction, Frequency of vibration, direction of vibration.*

1. INTRODUCTION

Study of mechanics of friction and the relationship between friction and wear dates back to the sixteenth century, almost immediately after the invention of Newton's law of motion. Friction process with vibration is an important practical phenomena because the influence of vibration can cause significant change in this process. It is known that vibration and friction are dependent on each other. Friction generates vibration in various forms, while vibration affects friction in turns. The considerable practical importance of this type of friction led many researchers to undertake experimental analysis [1-2]. They observed that many materials show dependence of normal load, sliding velocity and apparent area on the coefficient of static and kinetic friction in dry and lubricated conditions. Some explanations are given in order to justify the decrease in the friction coefficient though some of the researchers have different views. They claimed that friction force can be increased or decreased as a result of an adequate choice of parameters like surface pressure, amplitude, normal load, sliding velocity, material, frequency, surface roughness, humidity etc. [3-7]. Several other researchers worked on friction force which increased or decreased depending on vibration patameters [8-10]. However, the effect of different direction of vibration in relation to frequency of vibration on friction is yet to be investigated. In the present study, the effects of frequency and direction of vibration on the friction coefficient between solid surfaces are investigated.

This paper describes the results of an experimental investigation of the effects of frequency and direction of vibration on friction. Experiments were conducted using a pin on disc setup with a stainless steel pin sliding on an aluminum disc without lubrication. Vibrations are generated artificially in such a way that amplitude, frequency and direction of vibration can be controlled. Friction coefficient under vibration along the direction of sliding velocity at different frequency of vibration was investigated first and then the results were compared with the results obtained under vibration perpendicular to the direction of sliding velocity.

2. EXPERIMENTAL DETAILS

The set-up is a modified version of pin-on-disc machine is shown Fig.1. In this set-up, a circular aluminum test sample (disc) is fixed on a rotating table. Weights are placed on the load arm in such a way that it can act on the disc through the tip of the pin. Special mechanism is incorporated to generate vibration of the rotating table. For generating horizontal vibration, a spring is fixed at one end of the shaft and other end of the rotating table. During the rotation of the shaft, the adjusting barrier create disturbance due to the rotation of the rollers connected with the rotating table. Due to this disturbance spring is deflected horizontally and hence vibration is generated. Vertical deflection of the spring is restricted by the U-shaped guides.

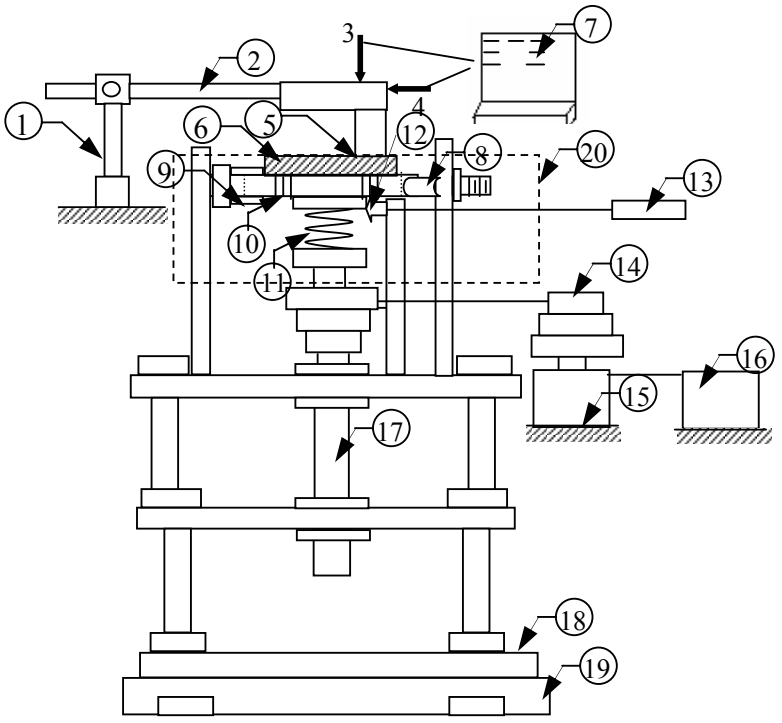

Fig. 1: Block Diagram of the Experimental Set-up

Frequency of vibration was varied by varying the number of rollers at the rotating table without varying the rpm of the rotating table or/and by varying the rpm of the rotating table without varying the number of slots at the lower circular plate. Amplitude of vibration was varied by adjusting the length of the adjusting barrier by a length adjusting screw. Linear velocity was varied by changing the radius of rotation or location of the pin on the disc

without varying the rpm of the motor or/and by changing the rpm of the motor without varying the radius of rotation or location of the pin on the disc. The rpm of the rotating table was varied by a digital inverter.

The set-up was placed inside a chamber where relative humidity can be adjusted by providing required amount of moisture. Relative humidity was measured by using digital hygrometer. Two load cells are incorporated with the set-up, one for measuring vertical load and the other for measuring horizontal load. Surface roughness tester, vibration meter are used to measure required parameters. A data acquisition system was used to input these data directly to a computer. Friction co-efficient was measured as the ratio of horizontal to normal forces.

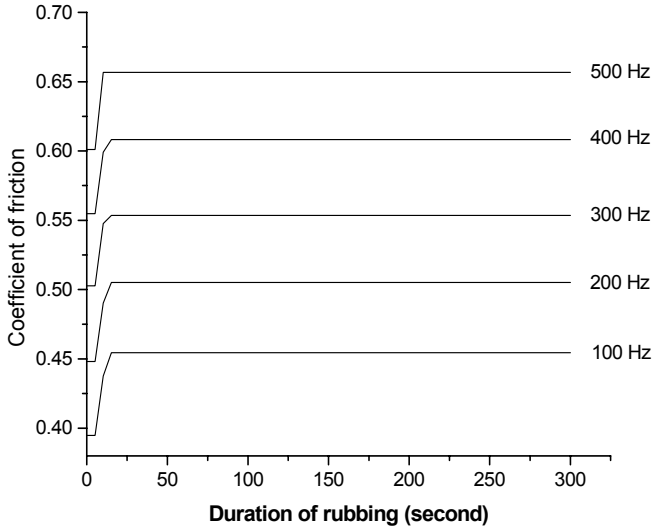

Fig. 2: Variation of friction coefficient with the variation of frequency of vibration and duration of rubbing (vibration along the direction of sliding velocity).

3. RESULTS AND DISCUSSION

Fig. 2 shows the variation of friction coefficient with frequency of vibration along the direction of sliding velocity. During experiment, linear velocity, relative humidity, normal load and amplitude were 1.50 m/s, 60 %, 10 N, and 1 mm respectively. Curves are drawn for frequency of vibration of 100-500 Hz. At 100 Hz frequency, friction co-efficient varies from 0.39 to 0.45 during the rubbing. It is also observed that friction co-efficient remains constant for first few seconds and increases almost linearly up to 0.45 over a duration of 10 seconds of rubbing and then it remains constant for the rest of the time i.e. upto 300 seconds of rubbing. Results also show the variation of friction coefficient for 200, 300, 400 and 500 Hz frequency of vibration. These results show similar trends as the result for 100 Hz. From the obtained results, it can also be seen that the values of friction coefficient increase with the increase of frequency of vibration. Moreover, it is observed that the trends of increasing friction coefficient for the initial period of rubbing are almost same for all the frequencies. The increase of friction coefficient for the increase of frequency of vibration might be due to the increase of contact surfaces between the contacting bodies. During sliding, changes in the conditions of mating surfaces occur which affect friction. During the initial period of rubbing, high asperities may be knocked off, surfaces may mate better, initial surface films may be worn, or new steady films may be formed. These changes result in friction going up from the

initial value. After the first steady-state period, changes in the interface may further occur, such as roughening and trapped particles which lead to an increase in friction. The increase of friction coefficient might also be associated with ploughing because of roughening and trapped wear particles. Increase of surface temperature, viscous damping of the friction surface, increased adhesion or microwelding between the materials might have some role on this increment of friction coefficient as well. After a certain duration of rubbing, the increase of surface roughness may become to a certain maximum value and hence the values of friction coefficient remain unchanged.

Fig. 3 shows the variation of friction coefficient with frequency of vibration perpendicular to direction of sliding velocity. During experiment, linear velocity, relative humidity, normal load and amplitude were 1.50 m/s, 60 %, 10 N, and 1 mm respectively. Curves are drawn for frequency of vibration of 100-500 Hz. At 100 Hz frequency, friction coefficient varies from 0.50 to 0.53 during the rubbing. It is also observed that friction coefficient remains constant for first few seconds and increases almost linearly up to 0.53 over a duration of 40 seconds of rubbing and then it remains constant for the rest of the time i.e. upto 300 seconds of rubbing. Results also show the variation of friction coefficient for 200, 300, 400 and 500 Hz frequency of vibration. In these cases, the rate of increasing the friction coefficient with time is higher than that at 100 Hz. From the obtained results, it can also be seen that the values of friction coefficient increase with the increase of frequency of vibration.

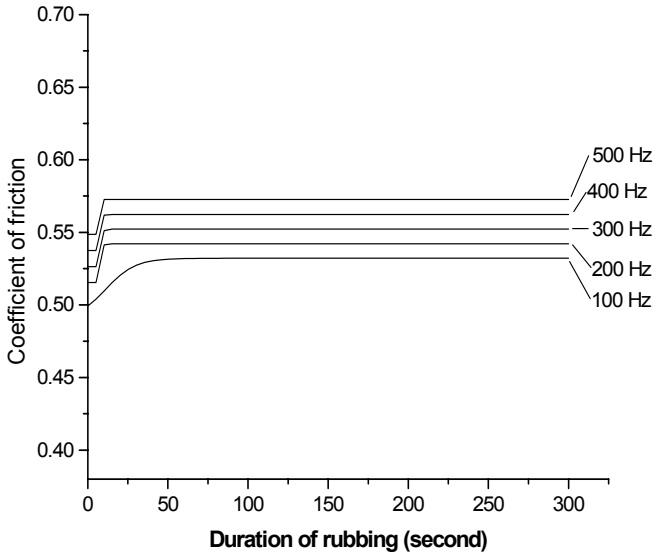

Fig. 3: Variation of friction coefficient with the variation of frequency of vibration and duration of rubbing (vibration perpendicular to the direction of sliding velocity).

Fig. 4 shows the variation of friction coefficient along and perpendicular to the direction of sliding velocity with frequency of vibration. Amplitude, linear velocity, normal load and relative humidity were 1mm, 1.50 m/s, 10N and 60% respectively. From this figure it is shown that the steady value of friction coefficient increases linearly with the increase of frequency of vibration for both the case of vibration. Friction coefficient varies from 0.45 to 0.66 with frequency of vibration from 100 to 500 Hz for vibration along the direction of sliding velocity. But it is 0.53 to 0.57 for vibration perpendicular to the direction of sliding velocity. From this figure it is also observed that the values of friction coefficient are higher

for vibration perpendicular to the direction of sliding than that for the vibration along the direction of sliding upto frequency 300 Hz. Between 300 to 500 Hz frequency of vibration opposite trends are observed that is, friction coefficient is more in case of vibration along the direction of sliding velocity than that of vibration perpendicular to the direction of sliding velocity.

For calculating friction coefficient each experiment was conducted several times at the identical condition. Friction coefficient shown in figures 2, 3 and 4 are drawn from the average values of these results. Results of different experiments vary within ±5% at the similar condition.

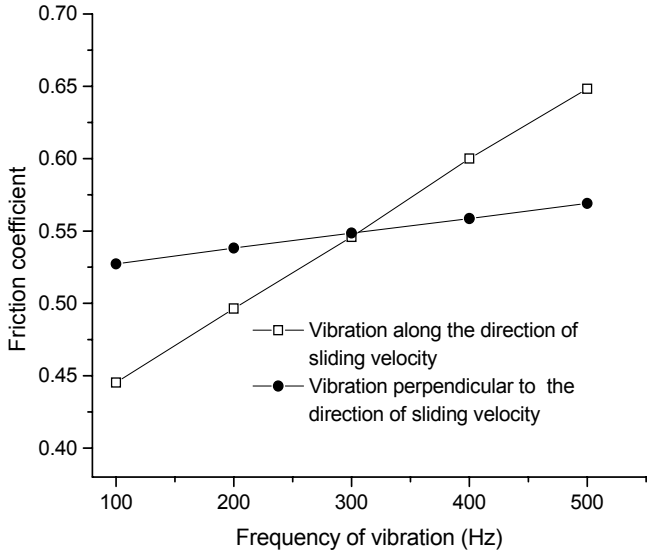

Fig.4: Variation of friction coefficient with the variation of frequency of vibration (vibration along and perpendicular to the direction of sliding velocity).

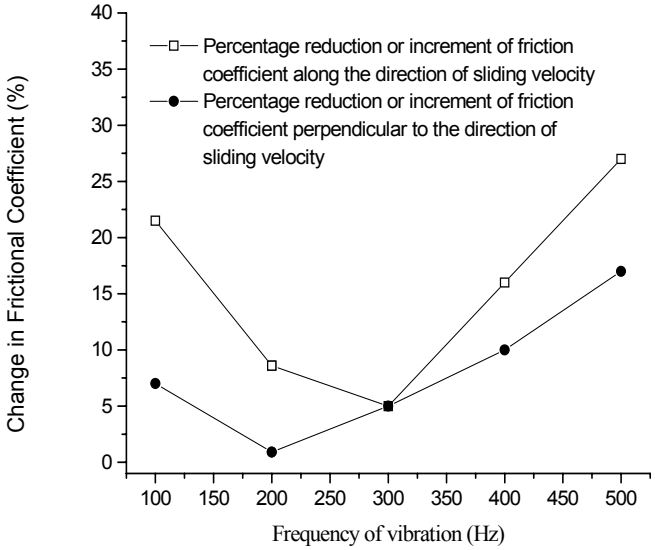

Fig. 5: Percentage reduction or increment of friction coefficient with the variation of frequency of vibration compared with the no vibration condition.

Fig. 5 shows the percentage reduction and increment of friction coefficient with the variation of frequency of vibration along and perpendicular to the direction of sliding velocity as compared with no vibration condition. From this figure it is shown that friction coefficient decreases from 22 to 5% and 7 to 1% up to frequency of vibration 300 and 200 Hz along and perpendicular to the direction of sliding velocity respectively. After that, the values of friction coefficient increases from 5 to 27% and 1 to 16% for vibration along and perpendicular to the direction of sliding velocity. It is mentioned that all these percentage of variations are calculated with reference to no vibration condition.

4. CONCLUSION

From the present investigation, the following conclusions are drawn:

1. The value of friction coefficient increases with the increase of frequency of vibration for both along and perpendicular to the direction of sliding velocity.
2. Friction coefficient is more at vibration perpendicular to the direction of sliding velocity up to 300 Hz frequency of vibration than that at vibration along the direction of sliding velocity and these results are reversed for the range of frequency of vibration from 300 to 500 Hz.
3. Rate of increase of friction coefficient with frequency of vibration is higher for vibration along the direction of sliding velocity.
4. Friction co-efficient is significantly high at no vibration (0 Hz) condition than that of vibration condition up to 200 and 300 Hz frequency of vibration for vibration perpendicular and along the direction of sliding velocity. After that the value of friction is lower at no vibration condition than that of vibration condition.

REFERENCES

[1] Tworzydlo, W. W., and Becker, E., Influence of forced vibrations on the static coefficient of friction-Numerical Modeling, Wear, 143 (1990), pp. 175-196.

[2] Godfrey, D., Vibration Reduces Metal to Metal Contact and Causes an Apparent Reduction in Friction, ASLE Transactions, 10 (1967), pp. 183-192.

[3] Tolstoi, D. M., Borisova, G. A., and Grigorova, S. R., Friction Reduction by Perpendicular Oscillations, Soviet Physics-Doklady, 17 (1973), pp.907-909.

[4] Wertheim, O., and Bucher, I., On the Influence of Controlled Vibration on Friction, Research Supported by the ISARELI Academy for Science (Grant. No. 030072), 2000.

[5] Imada, Y., and Nakajima, K., Effect of Humidity on the Friction and Wear Properties of Sn, Journal of Tribology, 117 (1995), pp. 737-744.

[6] Imada, Y., Effect of Humidity and Oxide Products on the Friction and Wear Properties of Mild Steel, Journal of Japanese Society of Tribology, 114 (1996), pp. 131-140.

[7] Tabor, D., Friction and Wear – Developments Over the Last 50 Years, Keynote Address, Proc. International Conf. Tribology – Friction, Lubrication and Wear, 50 Years On, London, Inst. Mech. Eng.,1987, pp. 157-172.

[8] Lenkiewicz, W., The Sliding Process–Effect of External Vibrations, Wear, 13 (1969), pp. 99-108.

[9] Aronov, V., D'souza, A. F., Kalpakjian, S., and Shareef, I., Interactions among Friction, Wear, and System Stiffness-Part 2: Vibrations Induced by Dry Friction, ASME Journal of Tribology, 106 (1984), pp. 59-64.

[10] Skare, T., and Stahl, J., Static and Dynamic Friction Processes Under the Influence of External Vibrations, Wear, 154 (1992), pp. 177-192.

Proceedings of the 4th BSME-ASME International Conference on Thermal Engineering
27-29 December, 2008, Dhaka, Bangladesh

STUDY ON THE EFFECT OF FRICTION IN INCREMENTAL FORMING PROCESS USING FEM

Behrooz Hemmati[1], Foad Farhani[2]

[1]Department of Mechanical Engineering
Islamic Azad University, Shahr-e-Rey Branch, Tehran, Iran
[2]Department of Mechanical Engineering
Iranian Research Organization for Science and Technology (I.R.O.S.T)
P.O. Box 15815 – 3538, Tehran, Iran
e-mail: b_hemmati@mecheng.iust.ac.ir

ABSTRACT

In the incremental sheet forming process a numerically controlled spherical tool is used to obtain the desired shape by pushing the sheet against a simple support tool. During the process, heat is generated due to the friction at the interface between the tool and sheet. Therefore, it is important to use suitable lubricants to control friction, and reduce the generated heat. This prevents the tearing of the sheet, and ensures production of flat and smooth surfaces. In this paper the effect of friction as an operating parameter has been studied for the incremental forming of a conical metal piece made of low carbon steel. Three different friction coefficients have been considered. We have used finite element simulation software and classical relations in this study. The analysis results, in the form of stress and strain contours, the sheet forming procedure during various stages of the process, and residual stresses show that the friction effects during the incremental forming process can be effectively controlled using suitable lubricants. The good agreement between the numerical and analytical results shows the suitability of the criteria used for determination of the mechanical behavior of the sheet, and that the simulation using FEM provides a useful tool for estimation of the effective parameters in the of incremental forming process.

KEYWORDS: *Incremental sheet forming, Die-less forming, Finte Element Method (FEM)*

1. INTRODUCTION

The classical deep drawing is an accurate and rapid process. However, there is a need for production of expensive special punches and dies. Therefore, use of classical metal forming can prove economical only for mass production of work pieces [1]. Stretch drawing for production of larger work pieces such as automobile and aircraft structures. Although the cost of the forming die (mold) is eliminated, this method is not efficient for production of complex parts. The spinning method is only suitable for symmetrical cylindrical and conical parts [2].

In incremental sheet forming process, which is an innovative and flexible method used in sheet metal forming technology, a numerically controlled spherical tool is used to obtain the desired shape by pushing the sheet against a simple support tool. The tool traces a complex path and forms the desired shape in a continuous manner (see fig. 1 [3]). It is used for production of work pieces in small volumes, and prototyping without the need for dies or special punches for forming of a complex shape**.** It has been developed as an answer to the shortcomings in the rapid prototyping method [4].
There are two different methods for incremental sheet forming. Figure 2 shows the incremental sheet forming methods with and without support. However, the supported method produces better results, but it is more complex [5].

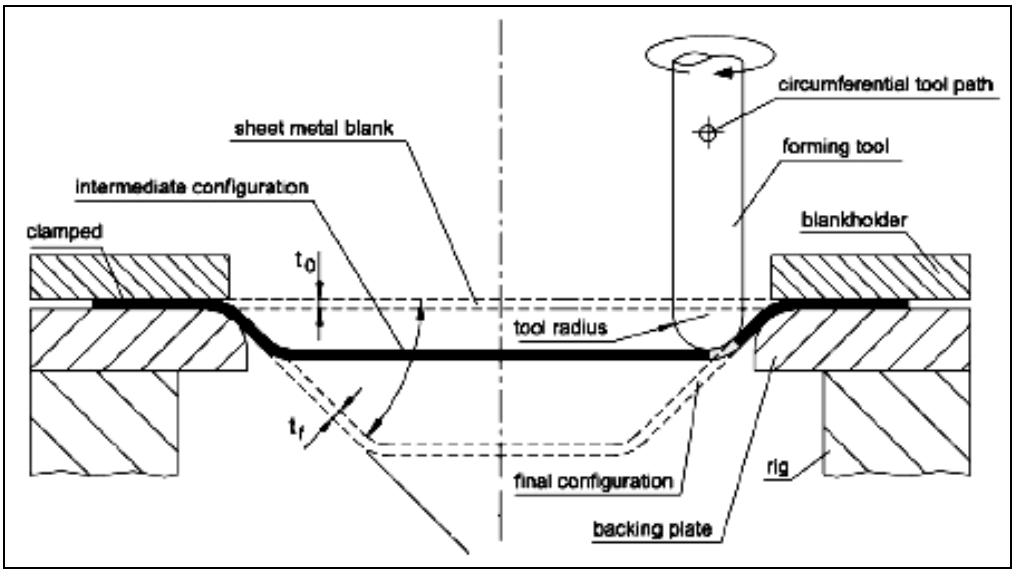

Fig.1 The incremental sheet forming method

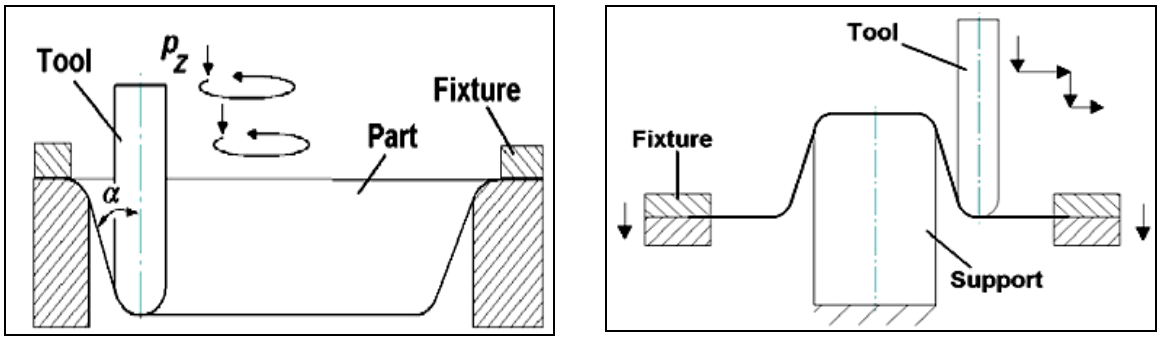

(a) Without support **(b) With support**

Fig.2 The incremental sheet forming methods

The sheet is supported from four sides, and the tool with spherical nib rotates about its own axis (see fig. 3). The single point forming is obtained as the result of regular displacement of the tool and change in the height of the milling machine work table [5, 6].

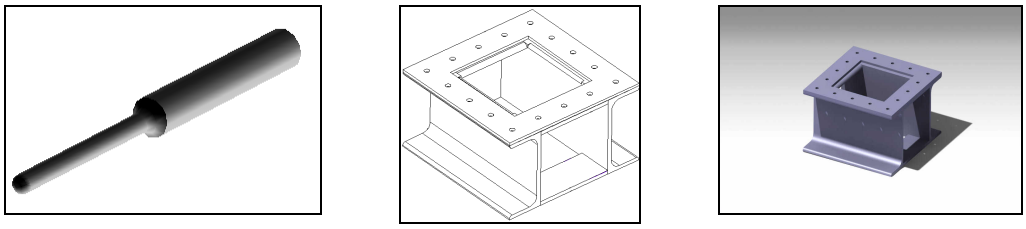

Fig.3 Geometry of the fixture and spherical nib tool

There are many occasions where it is not possible to directly observe all phenomena involved in manufacturing processes. In addition, there are limitations for direct measurement of some physical and technological parameters [6]. Therefore, it is necessary to use new methods for analysis and quantification of the related phenomena. Numerical methods such as FEM can be useful tools to supplement experimental studies, with the aim of obtaining the required technology know how for simulation of complex production processes.

During the incremental forming process, heat is generated due to the friction at the interface between the tool and sheet. Friction control prevents tearing of the sheet, and ensures production of flat and smooth surfaces. Therefore, it is important to use suitable lubricants to control friction, and reduce the generated heat. The type and amount of the lubricant used depends on the sheet thickness.

In this paper the effect of friction as an operating parameter has been studied for the incremental forming of a conical metal piece made of low carbon steel. Three friction coefficients have been considered. We have used finite element simulation software and classical relations in this study.

2. SHEET DEFORMATION GEOMETRY

Figure 4 presents the sheet forming geometry during the incremental sheet forming process, having an incremental depth of h [7]. The trigonometric relations related to the triangle in the above figure are given as:

$$\cos\beta = \frac{r}{l}, \qquad \sin\beta = \frac{h}{l}, \qquad \tan\beta = \frac{h}{r}, \qquad l \cong \beta R, \qquad \beta = \frac{l}{R} \tag{1}$$

For small β angles we have $\cos\beta \cong 1$ and $\sin\beta \cong \beta$. Therefore we have $\tan\beta = \frac{h}{r} \Rightarrow \beta = \frac{h}{r}$, and hence, $h = l\sin\beta = l\beta$. On substitution for $l \cong \beta R$ in this relation we get:

$$h = \beta^2 R \quad or \quad \beta = \sqrt{\frac{h}{R}} \tag{2}$$

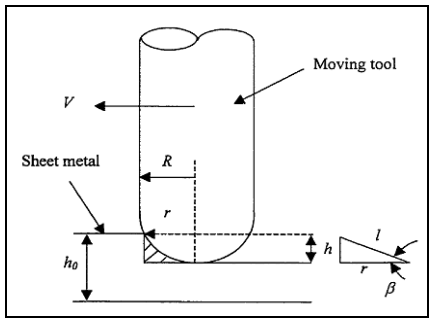

Fig.4 Sheet deformation geometry, incremental depth *h*, and volume of formed metal

2.1 Incremental Forming Per Unit Depth

Considering fig. 4, the incremental forming per unit depth is obtained from Eq.(3) as follows [7]:

$$D_v = \frac{1}{2} rhl \tag{3}$$

On substitution of $r = \frac{h}{\beta}$ in Eq.(3) we get:

$$D_v = \frac{h^2}{2\beta} = \frac{1}{2} h^{3/2} \sqrt{R} \tag{4}$$

2.2 The Incremental Forming Work

The time for the incremental forming is given by:

$$t_{def} = \frac{r}{V} \tag{5}$$

On substitution of $r = \frac{h}{\beta}$ in Eq.(5) we get:

$$t_{def} = \frac{h}{\beta V} \tag{6}$$

Also substitution of $\beta = \sqrt{\frac{h}{R}}$ in Eq.(6) yields:

$$t_{def} = \frac{\sqrt{hR}}{V} \tag{7}$$

The deformation velocity $v_{def} = \frac{h}{t_{def}}$ will be given as:

$$v_{def} = \sqrt{\frac{h}{R}} \times V \tag{8}$$

In the above equation, v is the tool speed, when moving with feed rate f. The incrmental forming work, W, can be calculated from the following equation [8, 9]:

$$W = F \times \sqrt{hR} \tag{9}$$

2.3. Strain in the Incremental Deformation

The strain in the metal sheet is found from the following equation [5]:

$$\varepsilon = \ln\left(\frac{h}{h_0}\right) \tag{10}$$

In the above equation, h is the incremental depth, and h_0 is the total sheet thickness (see fig. 4).

The rate of strain can be calculated from the following equation:

$$\dot{\varepsilon} = \frac{\varepsilon}{t_{def}} \tag{11}$$

On substitution of ε and t_{def} in Eq.(11) we get:

$$\dot{\varepsilon} = \frac{V \times \ln\left(\frac{h}{h_0}\right)}{\sqrt{hR}} \tag{12}$$

3. RELATIONSHIP BETWEEN REDUCTION IN SHEET THICKNESS AND BENDING

The incremental forming is a suitable method for production of complex 3-D shapes. The product geometry is free, but there are certain limitations in the geometry, depending on the sheet thickness and the equipment used [10, 11]. The dimensions and size of the spherical tool, fixes the minimum curve radius, which is equal to half of the tool diameter. As the size of the tool depends on the sheet thickness, a small tool with small thickness cannot withstand the forces associated with forming of thick metal sheets [5].

Production of inward bent forms is not possible using incremental forming, because the forming tool works only in Z-direction. The wall angle is limited by the sheet thickness. The wall angle is also affected by the formability of the material. Figure 5 shows the relationship between reduction in sheet thickness and bending, based on the final thickness t_f, initial thickness t_0 and the bend angle θ. The sheet thickness reduces with increase in its bending, as given by the following relation [8, 12]:

$$t_f = t_0 \sin\theta \tag{13}$$

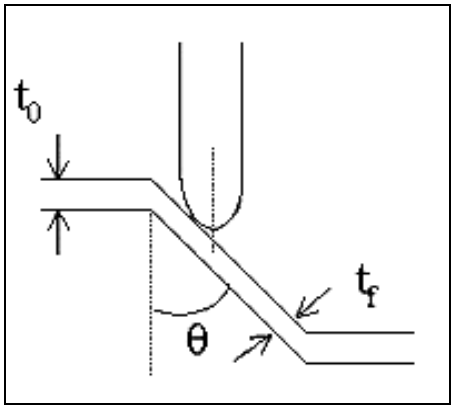

Fig.5 Relationship between reduction in sheet thickness and bending

4. THE FINITE ELEMENT MODEL

We have used rigid-flexible contact regime for modeling of incremental forming of the conical part, having a 45° wall angle, in which the flexible element is the steel sheet. The contact pairs consist of the sheet-fixture matrix lower surface and the sheet-spherical tool upper surface. The fixture and spherical tool act as the rigid surfaces. Surface elements have been used for the fixture, its frame and the spherical nib, and visco elements, with large deformation capability, have been selected for the metal sheet. Simulation of the forming process for the conical part, made of low carbon steel of 2 mm thickness, has been done in steps. Mechanical properties of the sheet metal, fixture and spherical nib tool are shown in tab. 1.

Table 1. Mechanical properties of the sheet, fixture and spherical tool

Material Type	E (GPa)	v	σ_x	n_x	σ_v	n_v	R0	R45	R90
Sheet	200	0.3	3.5	1923	0.07	623	2	1.45	2.5
Fixture and spherical tool	400	0.29	-	-	-	-	-	-	-

The modeling process has been carried out using ANSYS software. In order to reduce the solution time, only half of the die has been modeled, taking into account the asymmetric behavior of the element. As the sheet has a small displacement towards the matrix hole, between the fixture and matrix, resulting in increase in its thickness, a small inclination has been applied to the fixture frame to prevent the increase in force [10]. Horizontal, vertical and rotational displacements of the spherical tool elements, during each load step, have been considered to be loadings of the sheet, producing a step by step deformation of the sheet.

As mentioned earlier, it is necessary to lubricate the sheet surface. Lubrication reduces the friction between the spherical tool and metal sheet, and absorbs the heat generated due to friction at the interface between the tool and metal sheet. We have considered three values of coefficient of friction namely 0.01, 0.05 and 0.2, between the contacting surfaces. Figure 6 shows the complete FEM model of the fixture and spherical tool in two and three dimensions.

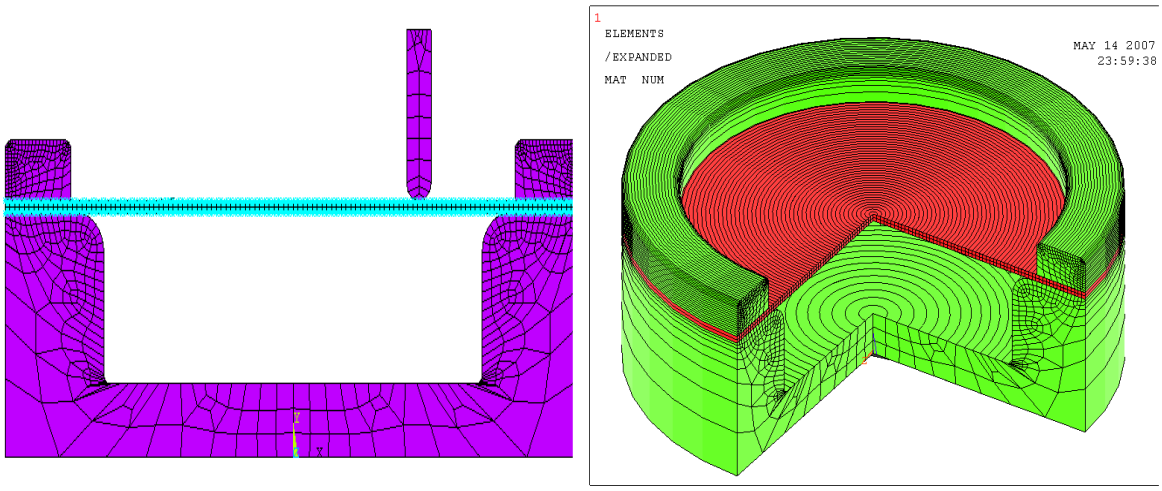

Fig.6 The complete FEM model of the fixture and spherical tool in two and three dimensions

5. ANALYSIS RESULTS

Figure 7 presents the stress contours on basis of Von Mises criteria for three values of coefficient of friction (0.01, 0.05, and 0.2) during the sheet deformation. As shown, with increase in the coefficient of friction, the stress concentration at the tool-sheet interface increases, in this case from 663 MPa to 1850 MPa, at the end of deformation.

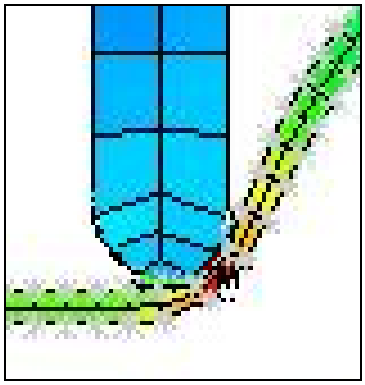

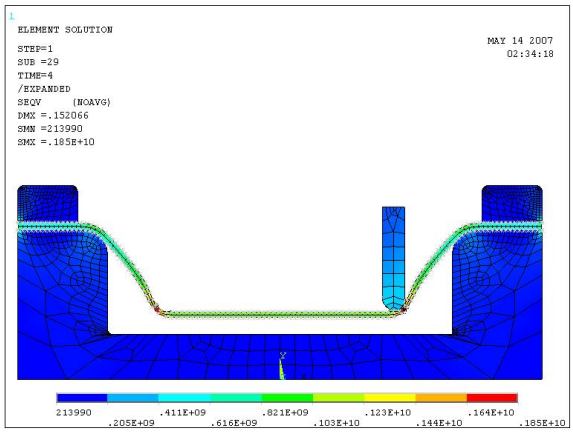

Coefficient of friction = 0. 2

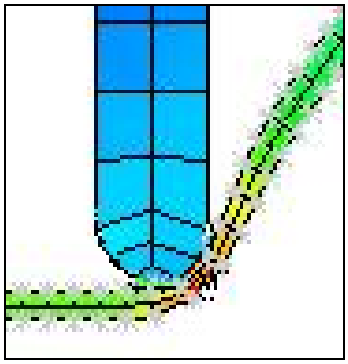

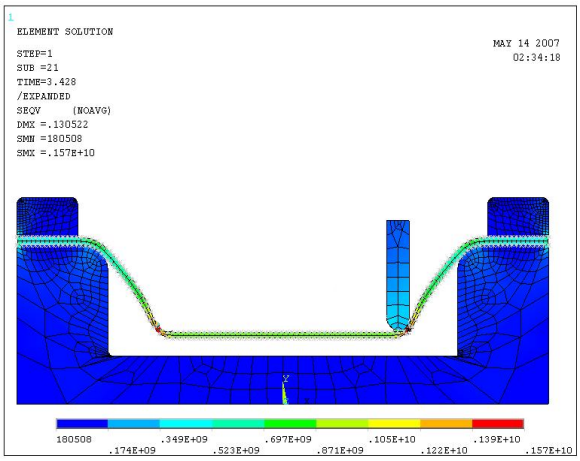

Coefficient of friction = 0. 05

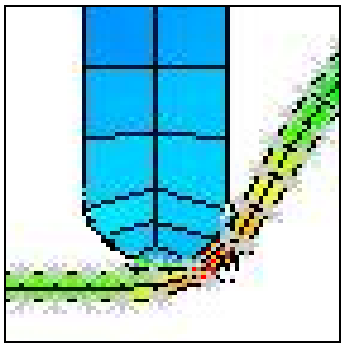

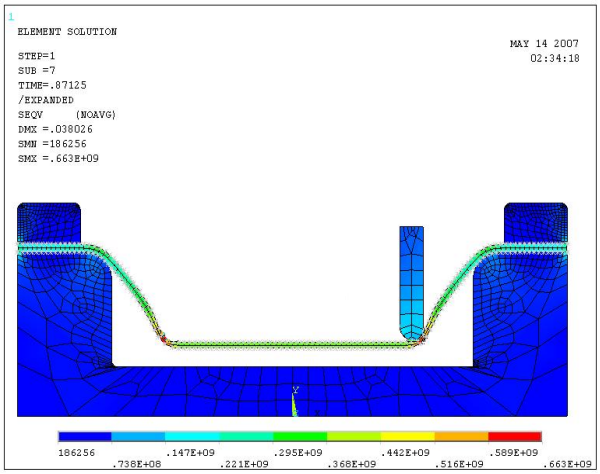

Coefficient of friction = 0. 01

Fig.7 Stress contours for three values of coefficient of friction during the sheet deformation

6. CONCLUSIONS

A stepwise simulation of single point incremental forming process for a conical part made of low carbon steel, for three values of coefficient of friction, has been performed using FEM. The numerical results have been compared with results from classical calculations and theoretical predictions as given below:

- With increase in the coefficient of friction, the stress concentration at the tool-sheet interface increases, at the end of deformation.
- Decrease in the wall thickness at the three values of coefficient of friction considered in this study, show similar values for FEM and classical methods. This proves the validity of the simulation process used in this study.
- The increase in friction clearly indicates that the sheet does not flow during the forming process. This indicates the need for suitable lubrication to reduce the friction.
- Existence of high amount of principle residual stresses in the final part geometry (in axial, radial and circumferential directions) indicates the main shortcoming of the sheet metal incremental forming, as predicted by the theory. However, this can provide opportunity for further analysis such as fatigue life, based on forming conditions and standard loading.
- The good agreement between the numerical and anlytical results shows the suitability of the criteria used for determination of the mechanical behaviour of the sheet. It also goes to show that simulation using FEM provides a useful tool for estimation of the effective parameters in the of incremental forming process.

7. REFERENCES

[1] Marciniak, Z., Duncan, J.L., Hu, S.J., Mechanics of Sheet Metal Forming, Butterworth-Heinemann, 2002.

[2] Dieter, G.E., Mechanical Metallurgy, McGraw-Hill, 1976.

[3] Altan, T., Meta1 Forming: Fundamentals and applications, American Society for Metals, 1983.

[4] Pearce, R., Sheet metal forming, Bristol, Hilger, 1991.

[5] Ramani, K., Miller, A.K., Cutkosky, M.R., Die-less Forming of Thermoplastic, *J. Matrix Continuous Fiber Composite Materials Process and Demonstration of Engineering for Industr*y, 117 (Nov. 1995), pp. 501- 507.

[6] Yang, E.G., Kobayashi, S., Mechanics of Plastic Deformation, MacMillan Co., New York, 1963.

[7] Lamminen, L., Tuominen, T., Kivivuori, S., Incremental Sheet Forming with an Industrial Robot, *Materials Forum*, 29, (2005).

[8] Jeswiet, J., Study of Single Point Incremental Sheet Forming with FEM, Society of Manufacturing Engineers, 2001.

[9] Backofen, W.A., Deformation Processing, Addison-Wesley, Massachusett, 1972.

[10] Hosford, W.F., Metal Forming - Mechanics and Metallurgy, Prentice-Hall, Inc., 1983.

[11] Matsubara, S., Incremental Backward Bulge Formïng of a Sheet Metal with a Hemispherical Head Tool, *J. Japan Society of Technical Processing (JSTP)*, 35(406), (1994).

[12] Mielnik, E.M., Metalworking Science and Engineering, McGraw-Hill, Inc., 1991.

Proceedings of the 4th BSME-ASME International Conference on Thermal Engineering
27-29 December, 2008, Dhaka, Bangladesh

CRYOGENIC TREATMENT OF METALS–A REVIEW OF EXPERIMENTAL STUDIES, UNDERLYING MECHANISM AND PROCESS EQUIPMENT

F. Farhani, K.S. Niaki

Iranian Research Organization for Science and Technology (I.R.O.S.T),
P.O. Box 15815 – 3538, Tehran, Iran.
ffarhani@yahoo.com

ABSTRACT

Cryogenic treatment of metals increases the metal wear resistance, which is an important consideration in industrial applications. The treatment also increases the intervals between component replacements for cutting tools, blades, drill bits, machining mills, etc. The cryogenic process usually involves controlled cooling of the metal from room temperature to liquid nitrogen (LN2) temperature, soaking of the metal at LN2 temperature for the prescribed time and finally warming up the metal back to the room temperature. Success of the cryogenic treatment depends on the rate of cooling, the soaking time at the LN2 temperature, and the final warming up of the treated metal. To ensure maximum effectiveness, the cryogenic process must be carried out in a dedicated programmable cryogenic processor. In this paper we review the latest research on the cryogenic treatment technology and its development in recent years, the underlying mechanism, and the processing equipment.

KEYWORDS: *Wear resistance, Cryogenic treatment, Tempering, Tool steels, Cryogenic processor*

1. INTRODUCTION

All mechanical components that undergo sliding or rolling contact are subjected to some degree of wear. So, wear is an important tribological phenomenon while studying the failure of components. Controlling machine wear is a fundamental function of lubrication [1].

Cryogenic treatment of metals (especially tooling steels) is a relatively new process that is used to improve metal wear resistance and the intervals between component replacements for blades, bits, machining mills etc., through controlled cooling of metals at cryogenic temperatures. It is a supplementary process to conventional heat treatment process in steels. It is an inexpensive, one time permanent treatment affecting the entire section of the component unlike coatings. The process can be grouped into two categories [2]: shallow cryogenic treatment, which is performed at -120 °C, and deep cryogenic treatment, which is performed at temperatures down to liquid nitrogen temperature (-196 °C). The benefits of cryogenic treatment of metals are [2]:

- dramatic reduction in consumption of perishable tooling, due to reduced frequency and cost of tool regrinding. Tool life improvements from 92% to 817% have been reported for cryogenically treated HSS tools in the industry.

- treated tooling will produce more parts per sharpening (typically two to five times more), and since chipping of the cutting edge is usually reduced, less metal is removed during re-sharpening. It substantially reduces machine downtime attributable to tool replacement.
- orderly arrangement of crystals, increase in the internal bonding energy, and achievement of a structural balance throughout the mass of the material.
- reduced scrap rate for machined forgings and castings by cryogenically treating prior to final machining, for better stability and surface finish.

In this paper we review the latest research on the cryogenic treatment technology and its development in recent years, the underlying mechanism, and the processing equipment. This paper is a condensation of relevant information available concerning the effects cryogenic treatment has on metal structure, as well as an overview of the theories and actual process involved in treating metals. Although this work will not answer all of the questions surrounding this process, it will be a useful source of information for workers in this field of research.

2. EXPERIMENTAL STUDIES

A number of studies have shown the effectiveness of the deep cryogenic process for increasing wear resistance and stability in materials, when applied correctly and consistently. However, research into the metallurgy of the cryogenic treatment process is still necessary to cast light upon the underlying mechanisms of the process, the reasons why process works well for only certain alloys, and to explain the variation in prior research results.
Works by various researchers have shown that cryogenic treatment produces metallurgical changes in the microstructure of steel (see fig. 1). Notice the uniform, more completely transformed microstructure and less retained austenite.

Fig.1 Microstructure of steel samples: (left) before, (right) after deep cryogenic process

Initially, the transformation of soft retained austenite into the harder martensite phase was believed to be the sole reason for the observed increase in the wear resistance of cryogenically processed materials. As greater amounts of retained austenite are transformed, and the amount of martensite is increased, the material obtains a more uniform hardness. The study by Barron **[**2**]** has shown that hardness is not increased appreciably in the material being treated, but the consistency of the hardness is greatly improved. The surface energy of martensite is higher than that of austenite due to the differences in their atomic structures. (Austenite has a Face-Centered-Cubic crystalline structure and martensite has a Body-Centered-Tetragonal crystalline structure as shown in fig. 2).

In adhesive wear situations, the martensite is less likely to “tear” out than is austenite. The probability of wear particles forming in steel in which the austenite has been transformed to martensite is less than for steel containing some retained austenite.

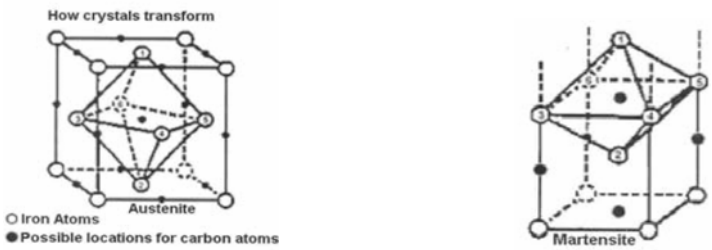

Fig.2 Crystalline structures: left- Austenite, right- Martensite

Further research for example by Meng et al. [3, 4] showed that the reduction in retained austenite was only one of the reasons for the increased wear resistance. They investigated the wear resistance and the microstructure of alloy tool steels after cryogenic treatment at deep cryogenic temperatures (soaking at -190 °C), and showed that certain fine *eta* (η) carbide particles are precipitated during the long cryogenic soak. These are in addition to the larger carbide particles present before cryogenic treatment. They concluded that the contribution of the deep cryogenic processing to wear resistance is through the precipitation of these *eta* carbides, which along with the larger particles, form a denser, more coherent and tougher matrix in material.

A study by the IIT Research Institute [5] suggested that the deep cryogenic treatment gave 50% extra pitting resistance, 5% more load carrying capacity, and a 40 °F to 60 °F higher tempering temperature. Although these experiments were performed on AISI 9310 material (standard helicopter transmission gear material) the conclusions show promising results which may be applicable to the general subject of mechanical and chemical wear resistance.

Rivero and Ruud [6] investigated the effects of strain hardening and retained austenite transformation, both of which are triggered by rolling contact, on the fatigue life of 52100 bearing steel. They concluded that the origin of residual stress generated due to rolling contact is associated with phase transformation. Since cryogenic processing converts retained austenite into martensite, this process can eliminate the primary mechanism for generation of residual stresses in ball bearings due to rolling contact.

Barron [7-9] has shown that high carbon/chromium steel, subjected to cryogenic treatment, has an 817% increase in wear resistance; silicon tool steel has a 503% and 52100 type steel has an increase of 420% (see tab. 1).

Table.1 Wear resistance vs. cryogenic soak temperature

Wear Resistance		
Alloy	**Untreated**	**Soaked at -190 °C**
52100	25.2	135
D2	224	878
A2	85.6	565
M2	1961	3993
O1	237	996

Mohanlal *et al*. [10] performed a study on the improvement in wear resistance and the significance of treatment parameters in different materials. Their findings indicate that the underlying mechanism is essentially an isothermal process, and that cryogenic treatment imparts nearly 110% improvement in tool life, that it is even superior to TiN coatings.

Molinari *et al*. [11] have studied the effect of deep cryogenic treatment (-196 °C) on properties of some tool steels by means of both field tests on real tools and laboratory tests. They concluded that deep cryogenic treatment of quenched and tempered high speed steel

tools increases hardness, reduces tool consumptions and down time for the equipment set up, thus leading to cost reduction of about 50%. Their laboratory investigation on an AISI M2 and AISI H13 steel confirmed the possibility of increasing the wear resistance and toughness by carrying out the treatment after the usual heat treatment.

Zhisheng *et al*. [12] studied the effect of deep cryogenic treatment of electrodes for spot welding hot dip galvanized steel plates, and subsequent electrode life improvements. Their experimental results showed that deep cryogenic treatment of electrodes caused Cr and Zr to disperse and made the grain smaller than in non-cryogenic treatment electrodes. They concluded that the electrical conductivity and the thermal conductivity of deep cryogenic treated electrodes are greatly improved, which results in improved electrode life for spot welding hot dip galvanized steel.

In another study, Singh *et al*. [13] investigated the effect of cryogenic treatment on the axial fatigue performance of fillet welded cruciform joints of AISI 304L stainless steel, which failed in the weld metal. Their observation shows that that after deep cryogenic treatment at liquid nitrogen temperature (-185 °C), the fatigue life improved almost by a factor of two. They have concluded that the significant microstructural changes that occurred during the treatment accounted for the improved fatigue performance.

More recently Singh *et al*. [14] have studied the improvement in the fatigue crack initiation lives of notches in AISI 304L austenitic stainless steel weldments after the deep cryogenic treatment of specimens at liquid nitrogen temperature (-185 °C). Their observation showed that during this treatment, a significant change in microstructure is developed. Strain induced martensitic transformation occurs, and that during this transformation, the weld metal expands. They concluded that this expansion relieves the tensile residual stresses and induces compressive stresses around the welded part. Their results also show the ineffectiveness of the cryogenic treatment in producing change in the fatigue crack propagation properties.

Leskovs˘ek, *et al*. [15] have studied the influence of deep-cryogenic treatment on wear resistance of vacuum heat-treated HSS. They have compared the wear behavior of vacuum heat-treated ESR AISI M2 high-speed steel and the same steel that was vacuum heat treated in conjunction with a deep-cryogenic treatment at -196 °C. The differences in the wear resistance obtained in their investigation were as high as an order of magnitude. However, they concluded that the beneficial effects were not a direct result of the type of the treatment, but related to a proper combination of the resulting fracture toughness and the hardness.

Da Silva *et al*. [16] have used both laboratory and shop floor tests in an automotive industry to verify the effect of cryogenic treatment on M2 high speed steel tools. They have carried out sliding abrasion and hardness tests as well as microstructural analysis. They report certain advantages for the treated tools in some of these tests.

Effect of deep cryogenic treatment on the matrix structure and abrasion resistance of high chromium cast iron subjected to destabilization heat treatment was investigated by Yang *et al*. [17]. Their results show that during the cryogenic treatment, the secondary carbides precipitate in austenite, which promote the transformation of retained austenite to martensite. The cryogenic treated alloys produced superior hardness and wear resistance (β) to the alloys without cryogenic treatment. They also concluded that cryogenic treatment cannot make retained austenite transform to martensite completely.

Effect of deep cryogenic treatment on the hardness and wear resistance of carburized steels used in gears was studied by Preciado *et al*. [18]. Their results show that the deep cryogenic treatment on quenched and tempered (first stage of tempering) steels, increased the wear resistance but the hardness was only increased in steels tempered at 200 °C.

Bensely *et al* [19] have investigated the effect of cryogenic treatment on the wear resistance of case carburized steel (En 353). Their experimental study deals with the pin on disk wear test without lubrication as per ASTM standard designation: G 99-95A. They carried

out their tests for three different load conditions and seven sliding speeds for the samples, which had undergone three different treatment conditions namely conventional heat treatment (CHT), shallow cryogenic treatment (SCT) and deep cryogenic treatment (DCT). Their finding shows that the wear resistance is considerably increased due to shallow cryogenic treatment, and that deep cryogenic treatment includes much more improvement in wear resistance when compared to conventional heat treatment.

Zhirafar *et al*. [20] carried out an experimental study to investigate the effects of cryogenic treatment on the mechanical properties and microstructures of AISI 4340 steel. They performed mechanical tests, including rotating fatigue, impact and hardness, after various heat treating conditions, and the results were compared. Fracture features of specimens were also compared. They have shown that in general, hardness and fatigue strength of the cryogenically treated specimens were a little higher whereas the toughness of the cryogenically treated specimens was lower when compared to that of the conventionally treated steel. Their neutron diffraction results showed that the transformation of retained austenite to martensite occurred, which along with possible carbide formation during tempering, is a key factor in improving hardness and fatigue resistance of the cryogenically treated specimens.

Liu *et al*. [21] have investigated the effects of deep cryogenic treatment on the microstructure, hardening behavior and abrasion resistance of 3Cr13Mo1V1.5 high chromium cast iron subjected to sub-critical treatment. Their results for deep cryogenic treatment after sub-critical treatment show that the hardness and abrasion resistance of high chromium cast iron can be boosted, primarily due to the large retained austenite transformation into martensite, and the secondary carbides precipitation. Their observation showed that in the course of sub-critical treatment with cryogenic treatment, the amount of precipitated secondary carbides was more than that in air cooling, and the secondary hardening peak advanced at a lower temperature.

Firouzdor *et al*. [22] have investigated the influence of deep cryogenic treatment on wear resistance and tool life of M2 HSS drills in high-speed dry drilling configuration of carbon steels. Their experimental results indicated 77 and 126% improvement in cryogenic-treated and cryogenic- and temper-treated drill lives, respectively. The results of wear rate test were in agreement with drill life tests. They concluded that the wear resistance improvement was mainly attributed to the resistance of cryogenically treated drills against diffusion wear mechanism, due to the formation of fine and homogeneous carbide particles during cryogenic treatment. Additionally, transformation of retained austenite to martensite played an effective role in improving hardness values.

Bensely *et al*. [23] have studies the effect of cryogenic treatment on the distribution of residual stress in the case carburized steel (En 353) using X-ray diffraction technique. They have adopted two types of cryogenic treatment: shallow cryogenic treatment (193 K) and deep cryogenic treatment (77 K), as a supplement to conventional heat treatment. Their results show that the amount of retained austenite in conventionally heat-treated, shallow cryogenically treated and deep cryogenically treated samples was 28%, 22% and 14%, respectively. The conventionally heat-treated, shallow cryogenically treated and deep cryogenically treated samples in untempered condition had a surface residual stress of −125MPa, −115MPa and −235MPa, respectively. After tempering, these values were found to be −150MPa, −80MPa and −80MPa, respectively. Their comparative study of the three treatments revealed that there was an increase in the compressive residual stress in steel that was subjected to cryogenic treatment prior to tempering. The experimental investigation revealed that deep cryogenically treated steel when subjected to tempering undergoes a reduction in compressive residual stress. Such stress relieving behavior was mainly due to the

increased precipitation of fine carbides in specimens subjected to deep cryogenic treatment with tempering.

3. THE CRYOGENIC TREATMENT PROCESS

The general processing cycle for modern cryogenic processors occurs within a three day time window, with 24 hours to reach the optimal bottom temperature for a product, 24 hours to hold at the bottom temperature, and 24 hours to return to room temperature. Depending on the product, some items will be heated in an oven to even higher temperatures. Some processors are capable of providing both the negative and positive extreme temperatures, separate units (a cryogenic processor and a dedicated oven) can sometimes produce better results depending upon the application.

The optimal bottom temperatures for objects, as well as the hold times involved, are determined utilizing a number of different research methods and backed by experience and analysis to determine what works the best for a given product. As new metals are used in different combinations for newer products on the market, processing profiles change to accommodate the changes in structure.

A number of companies maintain thermal profiles of various products that are updated for accuracy at least a few times a year with their ongoing research, including data from independent trials and studies. However, obtaining these profiles is sometimes difficult if they are not used for educational purposes (mainly institutional research).

A basic cryogenic treatment cycle consists of the following phases (see fig. 3):

1. A ramp down phase, during which the temperature of the sample is lowered slowly to the specified level (typically -190°C over a period of about one hour), to avoid any thermal shock from developing in the part.
2. A soaking phase, during which the metal sample is held at -190°C for the prescribed time, typically 24 hours.
3. A ramp up phase, during which the temperature of the object is brought back up to the room temperature. The ramp up phase is very important to the process. Ramping up too fast can cause problems such as cracking of the treated part.

It may be noted that a further temperature ramp up, during which the temperature of the object is elevated further, up to a value above ambient can be useful, especially with ferrous metals to reduce brittleness, if any. Also, a temperature hold phase, during which the metal sample is held at this elevated temperature for a specific time (may be up to 2 hours), can be incorporated in the basic cycle described above.

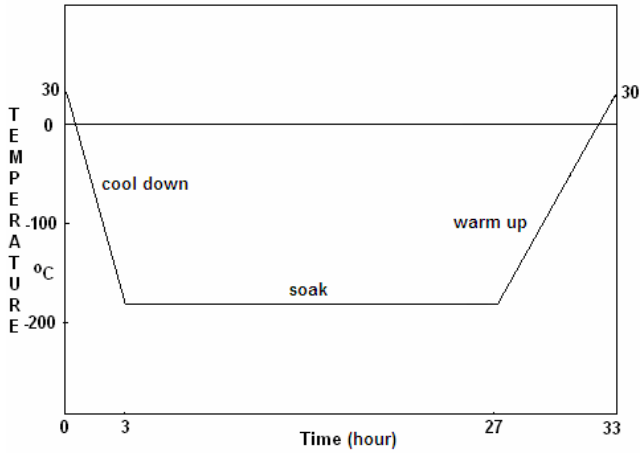

Fig.3 A basic cryogenic treatment cycle

In general, the prerequisites for successful implementation of this technique are: a method for creating the intense cold temperatures needed for the application, a method for the accurate monitoring and control of the working temperatures, and a reliable testing of the microstructure changes in the materials, for quantitative and qualitative evaluation of the treatment results.

4. THE CRYOGENIC PROCESSOR

A cryogenic processor is used to reach ultra-low temperatures of about -150 °C. The cooling is performed at slow rate to prevent thermal shock to the components being treated. The first commercial unit was developed by in the late 1960s. The development of programmable microprocessor controls allowed the machines to follow temperature profiles that greatly increased the effectiveness of the process.

Before programmable controls were added to control cryogenic processors, the "*treatment*" process of an object was done manually by immersing the object in liquid nitrogen. This normally caused thermal shock to occur within an object, resulting in cracks to the structure. Modern cryogenic processors measure changes in temperature and adjust the input of liquid nitrogen accordingly to ensure that only small fractional changes in temperature occur over a long period of time. Their temperature measurements and adjustments are condensed into "*profiles*" that are used to repeat the process in a certain way when treating for similarly grouped objects.

The general processing cycle for modern cryogenic processors occurs within a three day time window, with 24 hours to reach the optimal bottom temperature for a product, 24 hours to hold at the bottom temperature, and 24 hours to return to room temperature. Depending on the product, some items will be heated in an oven to even higher temperatures. Some processors are capable of providing both the negative and positive extreme temperatures, separate units (a cryogenic processor and a dedicated oven) can sometimes produce better results depending upon the application.

The optimal bottom temperatures for objects, as well as the hold times involved, are determined utilizing a number of different research methods and backed by experience and analysis to determine what works the best for a given product. As new metals are used in different combinations for newer products on the market, processing profiles change to accommodate the changes in structure.

Cryogenic processors come in a variety of sizes and configurations. The processors are typically designed to accommodate batch or continuous loads and come in two styles, front loading and top loading. The appropriate design depends upon the production volume and part configuration of a plant. Some examples are shown in fig. 4.

Fig.4 Examples of cryogenic processors by different manufacturers

Farhani *et al*. [24] presented the design and construction of a programmable cryogenic processor for treatment of steel alloys. The design minimizes chances of direct contact of liquid nitrogen with the working samples. The design is simple and the system can be constructed at low cost.

5 CONCLUSIONS

- The increase in wear resistance has been attributed to the transformation of soft retained austenite into the harder martensite phase, and the formation of fine carbide particles in the metal structure. These changes are the principal reasons for the dramatic improvement in wear resistance.
- Cryogenic treatment can reduce the austenite content but cannot make retained austenite transform to martensite completely.
- The cryogenic treatment process must be performed according to predefined temperature protocols, which are carried out in successive cooling and heating steps resulting in process cycles.
- In order to ensure the maximum effectiveness, the cryogenic process should sbe carried out in a dedicated programmable cryogenic system.

6. REFERENCES

[1] Wurzbach, R.N., et al., Improving component wear performance through cryogenic treatment, Maintenance Reliability Group, Brogue, 1996, Pennsylvania, USA.

[2] Barron, R.F., Cryogenic treatment of metals to improve wear resistance, *Cryogenics*, (Aug. 1982), pp. 409-413.

[3] Meng, F., Tagashira, K., Azuma, R., and Sohma, H., Role of Eta-carbide Precipitation in the Wear Resistance Improvements of Fe-12Cr-MO-V-1.4C Tool Steel by Cryogenic Treatment, *ISIJ International*, 34(1994), 2, pp. 205-210.

[4] Meng, F., Tagashira, K., and Sohma, H., Wear Resistance and Microstructure of Cryogenic Treated Fe-1.4Cr-1C Bearing Steel, *Scripta Metallurgica et Materialia*, 31(1994), 7, pp. 865-868.

[5] INFAC Findings, Increasing Hardness through Cryogenics, Illinois Institute of Technology Research Institute (IITRI), Nov. 1995, Illinois, USA.

[6] Rivero, I.V., Ruud, C., Residual Stresses and Patterns in 52100 Bearing Steel: Preliminary Analysis of Strain Hardening vs. Microstructural Transformation by XRD Analysis, *Lubrication Engineering*, (Oct. 2002), pp. 30-39.

[7] Barron, R.F., Cryogenic Treatment of AISIT8 and C1045 Steels, Advances in Cryogenic Engineering, 26, Plenum Press Inc., USA, 1980.

[8] Barron, R.F., How Cryogenic Treatment Controls Wear, 21st Inner-Plant Tool and Gage Conference (Shreveport, LA), Western Electric Co., 1982.

[9] Barron, R.F., Thompson, R.H., Effects of Cryogenic Treatment on Corrosion Resistance, Cryogenic Engineering Conference, paper BP-17, CA, USA, July 1989.

[10] Mohanlal, D., et al., Cryogenic treatment to augment wear resistance of tool and die steels, *Cryogenics*, 41(2001), pp. 149-155.

[11] Molinari, M., et al., Effect of deep cryogenic treatment on the mechanical properties of tool steels, *Journal of Materials Processing Technology*, 11892001), pp. 350-355.

[12] Zhisheng, W., et al., Effect of deep cryogenic treatment on electrode life and microstructure for spot welding hot dip galvanized steel, *Materials and Design*, 24(2003), pp.687–692.

[13] Singh, P.J., et al., Fatigue life improvement of AISI 304L cruciform welded joints by cryogenic treatment, *Engineering Failure Analysis*, 10(2003), pp. 1–12.
[14] Singh, P.J., et al., Fatigue life extension of notches in AISI 304L weldments using deep cryogenic treatment, *Engineering Failure Analysis*, 12(2005), pp. 263–271.
[15] Leskovs˘ek, V., et al., Influence of deep-cryogenic treatment on wear resistance of vacuum heat-treated HSS, *Vacuum*, 80(2006), pp. 507–518.
[16] Da Silva, F.J., et al., Performance of cryogenically treated HSS tools, *Wear*, 261(2006), pp. 674–685.
[17] Yang, H.S., et al., Effect of cryogenic treatment on the matrix structure and abrasion resistance of white cast iron subjected to destabilization treatment, *Wear*, 261(2006), pp. 1150–1154.
[18] Preciado, M., et al., Effect of low temperature tempering prior cryogenic treatment on carburized steels, *J. Materials Processing Technology*, 176(2006), pp. 41–44.
[19] Bensely, A. et al.,Enhancing the wear resistance of case carburized steel (En 353) by cryogenic treatment, *Cryogenics,* 45(2006), pp. 747–754.
[20] Zhirafar, S., et al., Effect of cryogenic treatment on the mechanical properties of 4340 steel, *J. Materials Processing Technology*, 186(2007), pp. 298–303.
[21] Liu, H., et al., Effects of deep cryogenic treatment on property of 3Cr13Mo1V1.5 high chromium cast iron, *Materials and Design*, 28(2007), pp.1059–1064.
[22] Firouzdor, V., et al., Effect of deep cryogenic treatment on wear resistance and tool life of M2 HSS drill, *J. Materials Processing Technology*, 206(2008), pp. 467–472.
[23] Bensely, A., et al., Effect of cryogenic treatment on distribution of residual stress in case carburized En 353 steel, *Materials Science and Engineering*, A(479)(2008), pp.229–235.
[24] Farhani, F., Niaki, K.S., Sarangi, S.K., Design and Construction of a Programmable Processor for Treatment of Metals at Low Temperatures, 3rd BSME-ASME International Conference on Thermal Engineering, Dhaka, Bangladesh, 20-22 December, 2006.

Proceedings of the 4th BSME-ASME International Conference on Thermal Engineering
27-29 December, 2008, Dhaka, Bangladesh

EFFECTIVENESS OF SNUBBER AS A PRESSURE PULSATION LIMITING UNIT USED IN RECIPROCATING HYDROGEN COMPRESSING

Mohammad Shiddiqur Rahman[1], Gyeonghwan Lee[1], Kwangsung Lee[1], Myeongkuk Ji[1], Hyomin Jeong[2] and Hanshik Chung[2]

[1]Dept. of Mechanical and Precision Engineering, Gyeongsang National University, Korea
[2]Dept. of Mechanical and Precision Engineering, Gyeongsang National University, Institute of Marine Industry, Tongyeong, Korea
Email: m_sq_rahman@yahoo.com

ABSTRACT

Rapid exhaustion of fossil fuels and also its harmful effects on environment make the scientists to attention to search for suitable alternative energy. Hydrogen has been becoming popular recently for its renewability and pollutant free properties. Because of its low volumetric energy content, compression is essential in all steps of hydrogen gas energy utilization. Pulsation waves are produced after passing through reciprocating compressor. Snubber- a pulsation limiting device is then introduced to reduce these harmful pulsation waveforms. An experiment has been conducted to investigate the effectiveness of snubber in regulating pressure pulsation developed during reciprocating compression. In order to get the detail pressure values at different parts of this snubber system, Computational Fluid Dynamics (CFD) analysis is applied. Pressure pulsation reduction by experiment and CFD model are performed and it shows that CFD has good agreement with experiment.

KEYWORDS: *Snubber, hydrogen compressing system, pressure amplitude, CFD*

1. INTRODUCTION

Fossil energy resources create unwanted environmental effects of various kinds- single or in combination. Such effects can be local or widespread and have long provoked concern. The emission of greenhouse gases: carbon dioxide, methane, nitrous oxide, and others is the most significant environmental effects of energy production and consumption. They alter the earth's climate which is inhospitable to life. The United States, as one of the world's largest producers and consumers of fossil fuels, is responsible for a major portion of global energy-related emissions. A total of 2732.9 and 1,958.6 out of 5945.3 million metric tons of carbon dioxide emissions from energy consumption by industrial and transportation sector in 2005 [1]. The increasing demand of energy for increased population and newly developed society, energy capturing politics of different country, and possibility of damage of environment make scientists to search for alternate future fuel and fuel vehicle. The recent hikes in the price of fossil fuel have added impetus to the movement towards hydrogen and other alternative fuels [2]. The physical and chemical properties of hydrogen make its utilization superior to fossil fuels. If generated from renewable energy, hydrogen becomes the crucial link in an inexhaustible global fuel cycle based on the cleanest, most abundant, natural, and elementary substances: H_2, O_2 and H_2O [3]. In integrating production planning and reactive scheduling for the optimization of a hydrogen supply network, compressor is an essential part [4]. Reciprocating compressor is used in hydrogen compression for its higher pressure increasing

capacity. But inherently there develops pressure pulsation resulted from reciprocating back and forth movement of piston inside the cylinder. Several various problems for the equipment related to the system and acting gas in it are inaccurate metering, unwanted vibrations, noises, explosions, shorten life of equipment, poor performance etc. of the hydrogen plant. Therefore, it needs to be lessened this pressure pulsations. Snubber is linear unit designed to limit this sudden unwanted pressure pulsation. It reduces the pressure fluctuation with restoring high pressure values and also removes the impurities contained in gas [5]. This study was taken to find out the snubber effectiveness in pressure fluctuation reduction by experiment and CFD.

2. EXPERIMENTAL SETUP AND METHOD

An acrylic snubber was constructed with inlet pipe, outlet pipe with 6 pressure measuring points (P1, P2, P3, P4, P5, P6) and with 163.97x75x4.88 mm flat plate inclined placed inside (Fig. 1). Inlet was connected to the compressor by small hose pipe and its outlet was exposed to atmosphere (Fig. 2). The experiment was conducted by running the compressor by motor setting at 10, 20, 30, 40, 50 and 60hz. Pressure was sensed by sensor at each points, amplified & recorded in PC using data logger. Air and hydrogen gas have almost same compressibility character, so, air was used in the experiment instead of hydrogen for its safety and availability.

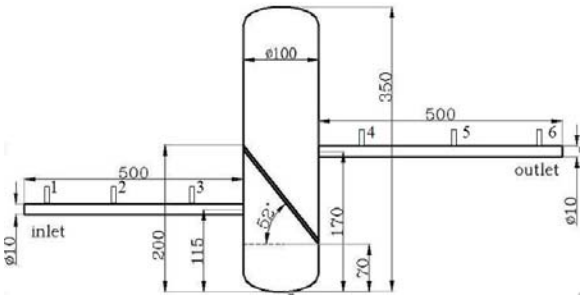

Fig. 1 Snubber dimensions

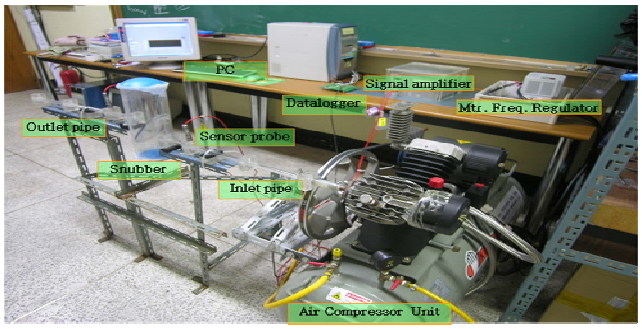

Fig. 2 Experimental set up

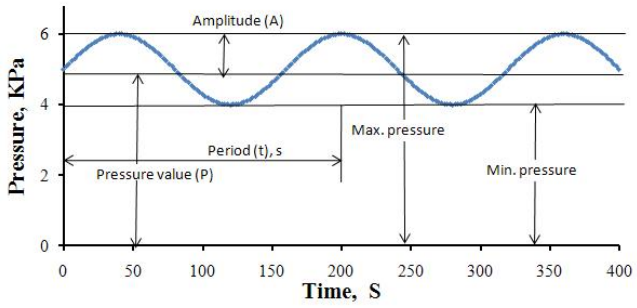

Fig. 3 Basic theory of pressure fluctuation

$$p = \frac{p_{max} + p_{min}}{2} \quad (1)$$

$$A = \frac{p_{max} - p_{min}}{2} \quad (2)$$

$$P_{red}(\%) = \frac{P_{in} - P_{out}}{P_{in}} \times 100\,\% \quad (3)$$

$$A_{red}(\%) = \frac{A_{in} - A_{out}}{A_{in}} \times 100\,\% \quad (4)$$

The periodic action of propelling gas through a pipe by the to and fro movement of the piston in the cylinder in reciprocating compressor created pulsation that causes the force of vibration in the whole system. Simple description of fluctuating pressure is shown in Fig. 3 and the pressure and its amplitude can be derived as eq. (1) and (2). Data at every points were analyzed for pressure loss and amplitude reduction. RMS values of input and output pressure were used for pressure loss. FFT analysis was done to on data to find out pressure amplitude. The resultant value was calculated by taking square root of summation of squares of all values [6]. Gas passing through a snubber will be reduced in magnitude of pressure and its fluctuations. Then, pressure and pressure pulsation reduction were obtained by eq. (3) and (4).

3. COMPUTATIONAL METHODS

Star CD (Version 3.24) computational code is employed, which solve the full 3D time dependent Navier-Stokes, continuity and energy equations using finite volume method. The turbulent flow in this investigation is considered as transient, incompressible, viscous, Newtonian and isotropic. The solver guesses the pressure filed and then solves the discretised form of the momentum equations to find new values of the pressure and velocity components. This process continues, in iterative manner, until the convergence criterion is satisfied. Turbulent model was using standard k-ε model. SIMPLE algorithm revised pressure and convection term belong to Upwind Scheme. Maximum residual tolerance was set under the 0.001 [7]. The geometry was drawn using the CATIA and then imported to pro-Surf as an Initial Graphics Exchange Specification file. Pressure from experiment at inlet (P1) and outlet (P6) were applied as boundary condition. The model was built in a half type for the symmetrical shape of the snubber and the symmetry boundary condition was applied.

4. RESULTS AND DISCUSSION

The gas pressures along the snubber system are varied corresponding to distance from the compressor outlet and motor frequency. Data obtained from the experiment show pressure characteristic of gas (Fig. 4). This pictorial view shows that higher pressure at inlet (P1) and then the pressure is reduced and reached at outlet (P6). It shows that pressure drop line for 1, 2, 3 are similar fasion but different in slope for all the motor frequency setting. At the outlet part of the snubber have also alike fashion of pressure gradient line as inlet parts but with lesser slope for each pressure line for 4, 5 and 6. When motor frequency is set at 30hz, the pressure at point 1, 2, 3, 4, 5 and 6 are 103.4879, 103.1812, 102.8375, 101.8500, 101.5282 and 101.3259 kPa, respectively. The highest pressure gradient is found for motor frequency 60hz and that of the lowest is at 10hz. The pressure gradient at point 1 and 6 are the highest and the lowest of all. There is a clear reasonable deviation in pressure line is found between 3 and 4 due to the main body of snubber. For higher motor frequency, the pressure reduction rate is also higher. Fig. 5 shows the pressure drop per unit length along the inlet and outlet pipe against specified motor speed. At inlet pipe, the pressure drop increases with the motor frequency. They are 2.6800, 8.9867, 17.3440, 29.9867, 44.4480 and 69.3147 Pa/cm for 10, 20, 30, 40, 50 and 60hz, respectively. The maximum and the minimum pressure drop are occurred at 60 and 10Hz, respectively for both of the cases. At outlet pipe, pressure drop also varied with motor speed but less in magnitude that of inlet pipe. The 2.3471 Pa/cm and 30.3645 Pa/cm pressure are found as minimum and maximum for 10 and 60hz at outlet pipe. The variation of pressure in inlet or outlet does not follow any statistical relationship with the motor frequency.

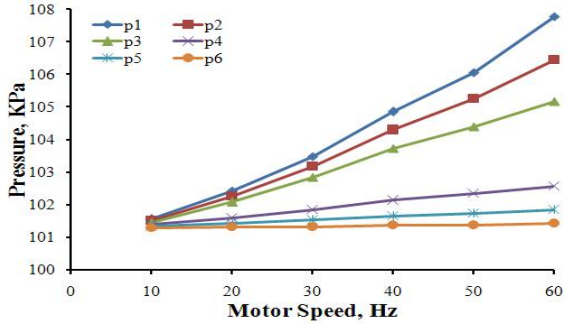

Fig 4. RMS values of pressure at corresponding to motor speed

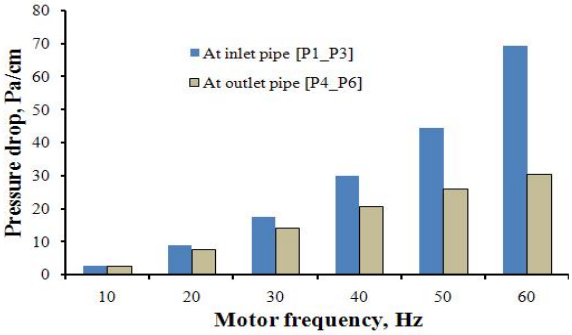

Fig. 5 RMS values of pressure drop at inlet and outlet for various motor speed

The pressure amplitude values of the flowing gas through the snubber are reduced different amount for different motor speed of compressor operation (Table 1). Tube shape buffered snubber reduces its incoming amplitude to a considerable amount. Input amplitude are varied from 0.2282 kPa to 2.0205 kPa; and the minimum and maximum output amplitudes are 0.0948 kPa and 0.8631 kPa, respectively for different motor speed. Although the compressor operates with different motor speed, it results with almost same percentages of amplitude reduction. The amplitude reductions in the snubber vary from 55.9466% to 58.4604%. Increased pressures are decreased here with the motor speed as it increase. The highest and lowest pressure loss are recorded as 2.4794% and 0.0678% for 60hz and 10hz. This indicates the best pressure restoring performance of the snubber. Detail pressure amplitudes per unit length are shown in Table 2. Amplitudes of pressured flowing gas drop per centimeter of length in inlet pipe are 2.5733, 6.0899, 10.8360, 20.5243, 38.3142, 63.7240Pa for the specified motor frequencies. But, at the outlet pipe drop of pressure amplitude are less in magnitude. The maximum 21.0838Pa amplitude is dropped per centimeter of the outlet pipe for 60hz.

Table 1: Pressure amplitude and pressure magnitude and theirs reduction at snubber

Motor	Amplitude at snubber			RMS pressure at snubber		
speed, hz	Input, kPa	Output, kPa	%, loss	Input, kPa	Output, kPa	%, loss
10	0.2282	0.0948	58.4604	101.4571	101.3883	0.0678
20	0.7931	0.3494	55.9466	102.0846	101.5995	0.4752
30	1.3492	0.5633	58.2487	102.8375	101.8500	0.9603
40	1.8810	0.8083	57.0261	103.7319	102.1418	1.5329
50	2.0814	0.8977	56.8709	104.3918	102.3423	1.9633
60	2.0205	0.8631	57.2832	105.1724	102.5648	2.4794

Table 2: Amplitude of pressure in inlet and in outlet pipe of the snubber

Motor	Amplitude in Inlet pipe			Amplitude in outlet pipe		
Freq., hz	At point1, kPa	At point3, kPa	Drop, Pa/cm	At point4, kPa	At point6, kPa	Drop, Pa/cm
10	0.3247	0.2282	2.5733	0.0948	0.0088	2.2933
20	1.0215	0.7931	6.0899	0.3494	0.0338	8.4144
30	1.7556	1.3492	10.8360	0.5633	0.0545	13.5690
40	2.6507	1.8810	20.5243	0.8083	0.0749	19.5579
50	3.5182	2.0814	38.3142	0.8977	0.0729	21.9937
60	4.4102	2.0205	63.7240	0.8631	0.0725	21.0838

Fig. 6 shows the transient pressure values along the snubber system at 4 different sections. It gives clear idea about pressure pulsation and its reduction scenarios from point to point. There is more reduction from point 3 to point 4 due to snubber arrangement and then reduction between 3 and 4 is almost similar as 2 and 3. It is presented CFD simulation results for each section in Fig. 7 for 35hz. CFD simulated pressures are almost same behaviours that of pressure values find experimentally at these four sections. At different points of the snubber, the pressure are measured experimentally and simulated by CFD. RMS pressure values are then calculated for both cases. These values of pressure by simulation and experiment are 2(103.8692, 103.8624); 3(103.5051, 103.4031); 4(102.1157, 102.0861); 5(101.8647, 101.6803). They are very close to each other. It differs from point to point and possesses maximum near compressor and then decreases along the length for pipe friction but abrupt down fall of the pressure due to tube snubber.

Analyzing all these CFD calculated pressures at point 2, 3, 4, and 5 are well match with the pressure found in experiment. So, now we can accept the pressure calculated by CFD to describe the pressure distribution in the snubber system. It explains the pressure values in the

snubber system with pictorial, numerical, maximum and minimum values for t=0.043s in full system (Fig 8(a)) and the transient pressure distribution pattern in the tube shape inside buffered snubber for different time steps (Fig. 8(b) – (j)). High pressure is developed at the beginning in the inlet pipe and it dwindles gradually with length of pipe. But there is sudden pressure drop from point 3 to point 4 due to snubber main body. Inside the snubber main unit, the entrance point of snubber, below the buffer parallel to inlet pipe, exit pipe entrance has high pressure zones. At the beginning of time step, there form different pressures at various points but at end of time step it is demolished and then pressure is become well distributed throughout the snubber but some locations. At the time step 0.043s, the maximum and minimum pressures are 0.1097E+06 Pa and 0.8787E+05Pa, respectively at the entrance and exit point in the snubber system. Detail pressure distribution with graphical and numerical at various time steps, can be obtained by selecting specific zone of the snubber model in CFD.

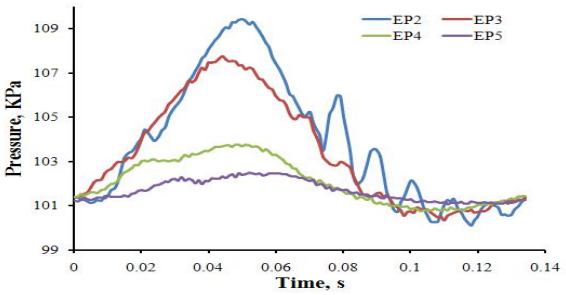

Fig. 6 Experimental pressure values against time at snubber

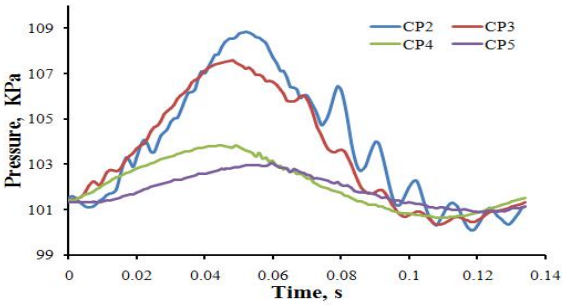

Fig. 7 CFD simulated pressure values against time at snubber

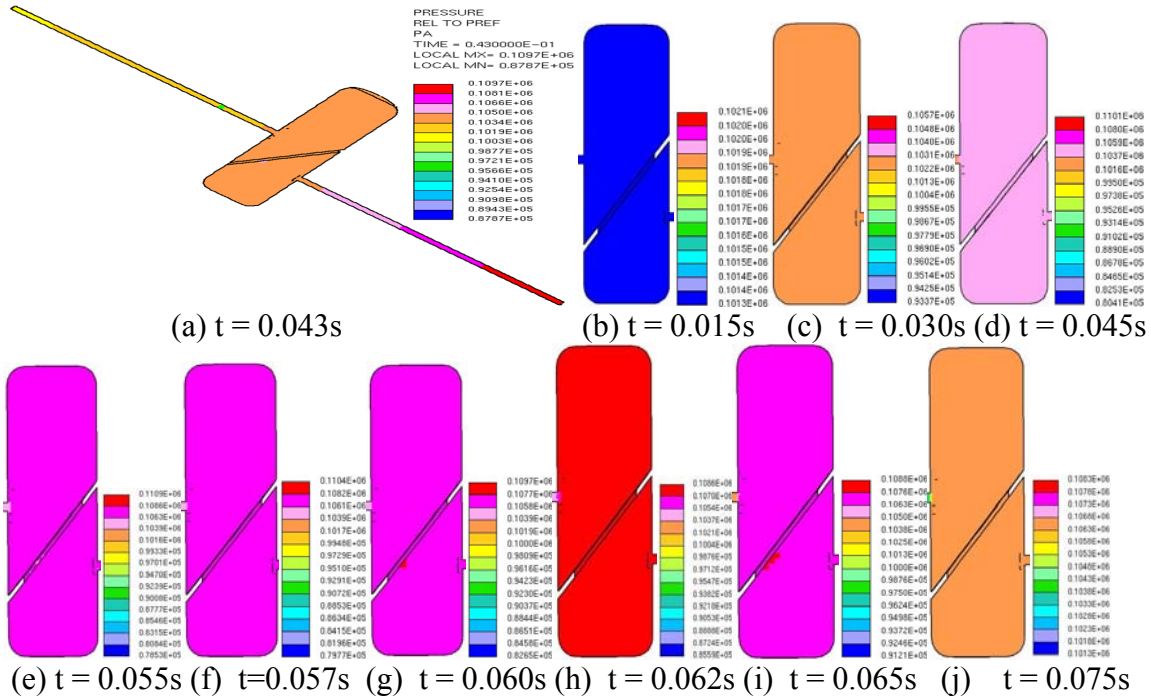

(a) t = 0.043s (b) t = 0.015s (c) t = 0.030s (d) t = 0.045s

(e) t = 0.055s (f) t=0.057s (g) t = 0.060s (h) t = 0.062s (i) t = 0.065s (j) t = 0.075s

Fig. 8 Pressure distribution inside tube shape of snubber at 35hz for different time steps

Table 3 shows the comparison of experiment and CFD simulation result for amplitude reduction at the snubber with 35Hz motor frequency. Input amplitudes and output amplitude are found 1.503 kPa and 1.649 kPa, 0.630 and 0.720 kPa from experiment and CFD simulation, respectively. The percentages of amplitude reduction are 58.064% and 56.343%

for experiment and CFD simulation. The variation of percentages of amplitude reduction from experiment is 1.721%. It indicates that CFD model credibility and efficacy and it can be applied for calculating pressure amplitude and amplitude reduction for any setting of motor frequency to run reciprocating compressor. Experiment with steel snubber of different dimensions was resulted maximum 21.59% pressure pulsation reduction [8]. The pressure loss for experiment and CFD are 1.283% and 1.344%, respectively. The 0.061% deviation in pressure loss is found from experiment which determines CFD as a powerful tool for calculating pressure pulsation reduction and pressure loss in the snubber.

Table 3 Comparison of experiment and CFD simulation for snubber performance

	Amplitude [P3_P4]			Pressure [P3_P4]		
Test type	Input, kPa	Output, kPa	% Reduction	Input, kPa	Output, kPa	% Loss
EXP	1.503	0.630	58.064	103.404	102.077	1.283
CFD	1.649	0.720	56.343	103.508	102.117	1.344

5. CONCLUSION

Compression is essential part of hydrogen economy in which pressure fluctuation attenuation is also essential. Numerical solution of various equations using CFD is a now-a-days tool to calculate pressure distribution in a system. CFD model can also predict the pressure information from which pressure pulsation and pressure loss can be obtained. In this study, CFD predicts pressure pulsation reduction as 56.343% and by experiment 58.064% pressure pulsation reduction is found. The percentage of pressure losses are estimated as 1.283% and 1.344%, for experiment and CFD simulation, respectively, at 35hz motor speed. Therefore, CFD can predict detail pressure pulsation and pressure loss at the snubber fast.

ACKNOWLEDGEMENT

This research was supported under the project No. 10024337 and Program for the Training and Graduate Students in Regional Innovation System of the Ministry of Knowledge Economy and Second-Phase of BK 21 project and NURI project, Korea.

REFERENCES

[1] Annual Energy Review 2006. Report No. DOE/EIA-0384.
[2] Shayegan, S. A., Hart, D., Pearson, P. and Joffe, D. Analysis of the cost of the hydrogen structure for buses in London. Journal of Power Sources, 2006. 157(2), 862-874.
[3] Salvador, M. A., Gene, D. B., Joel, M. F., Francisco, E. L. Vehicular storage of hydrogen in insulated pressure vessels. International Journal of Hydrogen Energy. 2006. 31: 2274-2283.
[4] Heever, S.A.V.D. and Grossman, I. E. A strategy for the integration of production planning and reactive scheduling in the optimization of hydrogen supply network. Computers & Chemical Engineering, 2003. Vol. 27: 1831-1839.
[5] American Petroleum Institute. 1995. Reciprocating compressors for petroleum, chemical and gas industry services. API Standard 618. American Petroleum Institute, Washington.
[6] Origin lab Co. 2003. Origin Reference v7.5. FFT Mathematical Description.
[7] Methodology Star CD Version 3.24, CD Adapco Group, 2004.
[8] Akbar, W.A., A study on high-pressured gas flow inside snubber of reciprocating hydrogen compressor system. A MS thesis, Mechanical and Precision Engineering Dept., Gyeongsang National University, South Korea, 2007: 62-67.

Proceedings of the 4th BSME-ASME International Conference on Thermal Engineering 27-29 December, 2008, Dhaka, Bangladesh

FORMULATION OF DAMAGE EVOLUTION IN COMPOSITE MATERIALS UNDER HYGROTHERMAL AGEING BY USING BACKWARD-FORWARD STOCHASTIC DIFFERENTIAL EQUATION

R. Rahman and A. Haque
Department of Aerospace Engineering and Mechanics
The University of Alabama, Tuscaloosa, AL 35487, USA
Email: ahaque@eng.ua.edu

ABSTRACT

A stochastic mathematical model has been developed for stiffness degradation due to hygrothermal ageing in polymer matrix composites (PMCs). The main focus was given in developing a stochastic micro-damage evolution model due to presence of various aggressive environmental ageing parameters such as temperature, moisture, and UV radiation (hardening) etc. The governing equation consists of Backward-Forward Stochastic Differential Equation (BFSDE). The damage nucleation and annihilation rates are assumed to follow Brownian motion. The solution of the proposed PDE was used in constructing a stochastic second order damage tensor which was incorporated in our proposed material stiffness degradation model.

Keywords: *Damage tensor, Backward-Forward Stochastic Differential Equation, Brownian motion, Hygrothermal degradation.*

1. INTRODUCTION

In recent years the use of PMCs is gradually increasing in aerospace, marine, military, sports and many other civil infrastructure applications due to their high specific strength and stiffness. These PMCs based structures in many situations are subjected to mechanical loading in presence of various environmental conditions such as temperature, moisture, UV radiation etc. So, indeed the question arises how the PMC structures will behave during their design life under the influence of these environmental parameters. Significant works [1-5] have been done in last ten years in order to predict the durability of PMC structures. One issue has been becoming more and more important in durability prediction; that is "Micro-crack density in composites and their evolution in time". This phenomenon is not strictly deterministic because of the uncertainty in damage nucleation as well as annihilation process [6, 7]. However, earlier investigators mostly considered temperature and moisture induced degradation as deterministic parameter. Once environmental degradation comes into the scenario the micro-crack density evolution becomes more uncertain. More specifically, the damage nucleation/annihilation rates may be defined as *Stochastic Processes*. Based on some assumptions, we may also define these terms as *Brownian motions*. We have incorporated Brownian motions in a generic damage evolution model proposed by Bai [8]. The stochastic governing differential equation in our model can predict the damage evolution under the influence of temperature and moisture [9, 10]. But the overall reliability in adverse situation has not been considered in our previous model. There should be backward validation of the governing differential equation. Hence, we have introduced "*Backward-Forward Stochastic*

Differential Equation (BFSDE)" as an extension of the previous formulation. Besides that, if we also consider environmental parameters as well as physical parameters of crack as random parameter, it is more convenient to apply BFSDE. Finally the material degradation have been evaluated based on evolving damage density.

2. DAMAGE DENSITY EVOLUTION MODEL

The generalized form of proposed damage density evolution equation in a RVE is ([9, 10]):

$$\frac{\partial \mathbf{n}}{\partial t}+(\overline{\mathrm{V}}\cdot\nabla)\mathbf{n}+A\frac{\partial \mathbf{n}}{\partial c}+\varphi\frac{\partial \mathbf{n}}{\partial \mu}+H\frac{\partial \mathbf{n}}{\partial h}+\theta\frac{\partial \mathbf{n}}{\partial T}=f(\mathbf{n},x_1,x_2,x_3,c,\mu,h,T)+\mathbf{n}_{\mathbf{N}}-\mathbf{n}_{\mathbf{A}} \tag{1}$$

$$\mathbf{n}(t_0,x_1,x_2,x_3,c,\mu,h,T:\sigma)=g(x_1,x_2,x_3,c,\mu,h,T)$$

Here, $f(\mathbf{n},x_1,x_2,x_3,c,\mu,h,T)\equiv \mathbf{n}\left(\frac{\partial \mathrm{V}_1}{\partial x_1}+\frac{\partial \mathrm{V}_2}{\partial x_2}+\frac{\partial \mathrm{V}_3}{\partial x_3}+\frac{\partial A}{\partial c}+\frac{\partial \varphi}{\partial \mu}+\frac{\partial H}{\partial h}+\frac{\partial \theta}{\partial T}\right)$ and

$$\mathbf{n}_N:\mathbf{Y}_N(t)\supseteq\left\{Y_{N_{\omega_L}}(t)\right\}=a_{N_{\omega_L}}(t)+b_{N_{\omega_L}}(t)B_{N_{\omega_L}}(t)$$

$$\mathbf{n}_A:\mathbf{Y}_A(t)\supseteq\left\{Y_{A_{\omega_L}}(t)\right\}=a_{A_{\omega_L}}(t)+b_{A_{\omega_L}}(t)B_{A_{\omega_L}}(t)$$

Lets' define the environmental and physical parameters of damage density in terms of "*White Noise*" as follows:

$$\begin{aligned}
\mathrm{V}_1&=\mathrm{V}_{1_0}+W(t)\\
\mathrm{V}_2&=\mathrm{V}_{2_0}+W(t)\\
\mathrm{V}_3&=\mathrm{V}_{3_0}+W(t)\\
A&=A_0+W(t)\\
\varphi&=\varphi_0+W(t)\\
H&=H_0+W(t)\\
\theta&=\theta_0+W(t)
\end{aligned} \tag{2}$$

Here, each term is in the form: "Parameter = Mean + White Noise" and $W(t)$is the "*White Noise*" term. Finally, we can define the "*Forward Stochastic Differential Equation*" after using equation (2) as (including initial condition):

$$\begin{aligned}
dn_t&=f_1(n_t,x_i,c,\mu,h,T)dt+\sigma(n_t,x_i,c,\mu,h,T)dB_t+a(t)dt+b(t)B_t dt\\
n_{t_0}&=g
\end{aligned} \tag{3}$$

Here, $a(t)=a_N(t)-a_A(t)$ and $b(t)=b_N(t)-b_A(t)$.

The above equation is in the form of Forward Stochastic differential Equation. We may associate this FSDE with a Backward SDE by using following expression with respect to a predictable process $\underline{n}_t$ (preferably from experimental observation of damage density) and the solution of FSDE n_t :

$$-d\overline{n_t} = f_2(n_t, \overline{n_t}, \underline{n_t}, t, x_i, c, \mu, h, T)dt + \underline{n_t}dB_t$$
$$\overline{n_T} = h \tag{4}$$

The above two equations leads to a solution as triplet: $\left(\overline{n_t}, n_t, \underline{n_t}\right)$. Physically, this triplet refers to the evolving damage density in time. Equation (4) solely depends on the experimental result and solution from forward differential equation. The advantage of using BFSDE approach is to lower the influence of environmental and physical parameters of crack. The experimental observation of these parameters is more difficult than observing micro-crack density directly. This triplet can be weightily averaged based on the significance:

$$n_{L_{AVG}} = \frac{l_1\underline{n_t} + l_2 n_t + l_2\overline{n_t}}{3} \tag{5}$$

Here, l_1, l_2, l_3 are corresponding weights.

Hence, the total number of damages (for a certain probability state) in a RVE is:

$$M_{L_{AVG}}(t, c, \mu, h, T) = \iiint_V n_{L_{AVG}} dV \tag{6}$$

The second order damage tensor at any certain mode α is written in modified form ([7-9], [14, 15]):

$$D^{\alpha}_{ij_{L_{AVG}}} = \frac{1}{V}\left[\sum_{k=0}^{M^{\alpha}_{ijL_{AVG}}(t,c,\mu,h,T)} (d_{ij})_k\right] \tag{7}$$

Here, d_{ij}: Integral of the diad $a_i n_i$ over the surface of damage. a_i: Damage influence factor and n_i: Outward normal on the damage surface.

Finally, we can write the strain pseudo-energy in terms of this damage tensor as; [9, 10]:

$$W = P_0 + (f_1\varepsilon_{11} + f_2\varepsilon_{22} + f_3\varepsilon_{33} + f_4\varepsilon_{23}D^{\alpha}_{23_{AVG}} + f_5\varepsilon_{13}D^{\alpha}_{13_{AVG}} + f_6\varepsilon_{12}D^{\alpha}_{12_{AVG}} + f_7\varepsilon_{11}D^{\alpha}_{11_{AVG}} +$$
$$f_8\varepsilon_{11}D^{\alpha}_{22_{AVG}} + f_9\varepsilon_{11}D^{\alpha}_{33_{AVG}} + f_{10}\varepsilon_{22}D^{\alpha}_{11_{AVG}} + f_{11}\varepsilon_{22}D^{\alpha}_{22_{AVG}} + f_{12}\varepsilon_{22}D^{\alpha}_{33_{AVG}} + f_{13}\varepsilon_{33}D^{\alpha}_{11_{AVG}} +$$
$$f_{14}\varepsilon_{33}\underline{D}^{\alpha}_{22} + f_{15}\varepsilon_{33}\underline{D}^{\alpha}_{33}) + (g_1\varepsilon^2{}_{11} + g_2\varepsilon^2{}_{22} + g_3\varepsilon^2{}_{33} + g_4\varepsilon^2{}_{12} + g_5\varepsilon^2{}_{13} + g_6\varepsilon^2{}_{23} +$$
$$g_7\varepsilon_{11}\varepsilon_{22} + g_8\varepsilon_{22}\varepsilon_{33} + g_9\varepsilon_{33}\varepsilon_{11} + g_{10}\varepsilon^2{}_{11}D^{\alpha}_{11_{AVG}} + g_{11}\varepsilon^2{}_{11}D^{\alpha}_{22_{AVG}} + g_{12}\varepsilon^2{}_{11}D^{\alpha}_{33_{AVG}} +$$
$$\ldots\ldots\ldots\ldots\ldots\ldots g_{44}\varepsilon_{33}\varepsilon_{11}D^{\alpha}_{22_{AVG}} + g_{45}\varepsilon_{33}\varepsilon_{11}D^{\alpha}_{33_{AVG}}) \tag{8}$$

If we consider only the damage tensor $D_{11_{L_{AVG}}}$, we may write the material properties as

$$E_{11_{L_{AVG}}} = \frac{\Delta_1}{\left(4g_3g_2 - g_8^2 + \left[4g_{13}g_{16} - g_{40}^2\right]D_{11_{L_{AVG}}}^2 - \left[2g_8g_{40} - 4g_3g_{13} - 4g_2g_{16}\right]D_{11_{L_{AVG}}}\right)}$$

$$E_{22_{L_{AVG}}} = \frac{\Delta_1}{\left(4g_3g_1 - g_9^2 + \left[4g_{10}g_{16} - g_{43}^2\right]D_{11_{L_{AVG}}}^2 - \left[2g_9g_{43} - 4g_1g_{16} - 4g_3g_{10}\right]D_{11_{L_{AVG}}}\right)}$$

$$E_{33_{L_{AVG}}} = \frac{\Delta_1}{\left(4g_2g_1 - g_7^2 + \left[4g_{10}g_{13} - g_{37}^2\right]D_{11_{L_{AVG}}}^2 - \left[2g_7g_{37} - 4g_1g_{13} - 4g_2g_{10}\right]D_{11_{L_{AVG}}}\right)}$$

:

$$\nu_{12_{L_{AVG}}} = \frac{\left(2g_3g_7 - g_8g_9 + \left[2g_{37}g_{16} - g_{40}g_{43}\right]D_{11_{L_{AVG}}}^2 + 2\left[g_3g_{37} + g_7g_{16}\right]D_{11_{L_{AVG}}} - \left[g_7g_{16} + g_9g_{40}\right]D_{11_{L_{AVG}}}\right)}{\left(4g_3g_2 - g_8^2 - 2\left[g_8g_{40} - 2g_2g_{16} - g_3g_{13}\right]D_{11_{L_{AVG}}} - \left[g_{40}^2 - 4g_{13}g_{16}\right]D_{11_{L_{AVG}}}^2\right)}$$

$$\nu_{13_{L_{AVG}}} = \frac{\left(g_8g_9 - 2g_2g_9 + \left[g_{37}g_{40} - 2g_{13}g_{43}\right]D_{11_{L_{AVG}}}^2 - 2\left[g_9g_{13} + g_2g_{43}\right]D_{11_{L_{AVG}}} + \left[g_7g_{40} + g_8g_{37}\right]D_{11_{L_{AVG}}}\right)}{\left(4g_3g_2 - g_8^2 - 2\left[g_8g_{40} - 2g_2g_{16} - g_3g_{13}\right]D_{11_{L_{AVG}}} - \left[g_{40}^2 - 4g_{13}g_{16}\right]D_{11_{L_{AVG}}}^2\right)}$$

$$\nu_{23_{L_{AVG}}} = \frac{\left(2g_1g_8 - g_7g_9 + \left[2g_{10}g_{40} - g_{37}g_{43}\right]D_{11_{L_{AVG}}}^2 + 2\left[g_1g_{40} + g_8g_{10}\right]D_{11_{L_{AVG}}} - \left[g_7g_{43} + g_9g_{37}\right]D_{11_{L_{AVG}}}\right)}{\left(4g_3g_1 - g_9^2 - 2\left[g_9g_{43} - 2g_1g_{16} - g_3g_{10}\right]D_{11_{L_{AVG}}} - \left[g_{43}^2 - 4g_{10}g_{16}\right]D_{11_{L_{AVG}}}^2\right)}$$

$$\begin{aligned} G_{12_{L_{AVG}}} &= 2g_4 + 2g_{25}D_{11_{L_{AVG}}} \\ G_{31_{L_{AVG}}} &= 2g_5 + 2g_{19}D_{11_{L_{AVG}}} \\ G_{23_{L_{AVG}}} &= 2g_6 + 2g_{22}D_{11_{L_{AVG}}} \end{aligned} \tag{9}$$

Here,

$$\Delta_1 = 8g_1g_2g_2 + 2g_7g_8g_9 - 2\left[g_1g_8^2 + g_2g_9^2 + g_3g_7^2\right] + 2\begin{bmatrix} g_7g_9g_{40} + g_7g_8g_{43} + g_8g_9g_{37} - \\ 2g_1g_8g_{40} - 2g_2g_9g_{43} - 2g_3g_7g_{37} \\ +4g_1g_2g_{16} + 4g_1g_3g_{13} + 4g_2g_3g_{10} \end{bmatrix}D_{11_{L_{AVG}}}$$

$$-2\left[g_7^2g_{16} + g_8^2g_{10} + g_9^2g_{13}\right]D_{11_{L_{AVG}}} + 2\begin{bmatrix} g_7g_{40}g_{43} + g_8g_{37}g_{43} + g_9g_{37}g_{40} - 2g_7g_{16}g_{37} - 2g_9g_{13}g_{43} \\ -2g_7g_{40}g_{43} - 2g_8g_{10}g_{40} + 4g_1g_{13}g_{16} + 4g_3g_{10}g_{13} + 4g_2g_{10}g_{16} \end{bmatrix}D_{11_{L_{AVG}}}^2$$

$$-2\left[g_1g_{40}^2 + g_2g_{43}^2 + g_3g_{37}^2\right]D_{11_{L_{AVG}}}^2 + 2\left[g_{40}g_{37}g_{43} + 4g_{10}g_{16}g_{13}\right]D_{11_{L_{AVG}}}^3 - 2\left[g_{10}g_{40}^2 + g_{13}g_{43}^2 + g_{16}g_{37}^2\right]D_{11_{L_{AVG}}}^3$$

3. **PREDICTING MATERIAL PROPERTY VARIANCE**:

As we are developing the model based on weighted averaged damage density, the variance will be an average entity itself. The estimated range can be written as:

$$\left(\frac{(M-1)K^2_{11VAR_{AVG}}(t)}{\chi^2_{a/2}}, \frac{(M-1)K^2_{11VAR_{AVG}}(t)^2}{\chi^2_{1-a/2}}\right) \tag{10}$$

Here,

K represents $E_{11_{L_{AVG}}}(t), E_{22_{L_{AVG}}}(t), E_{33_{L_{AVG}}}(t), G_{12_{L_{AVG}}}(t), G_{31_{L_{AVG}}}(t), G_{23_{L_{AVG}}}(t), \nu_{12_{L_{AVG}}}(t)$

$\nu_{13_{L_{AVG}}}(t), \nu_{23_{L_{AVG}}}(t)$

4. CONCLUSION

The stochastic damage evolution model has been extended to evaluate degradation of composite materials under synergistic environmental ageing parameters such as temperature, moisture and UV radiation in a more reliable manner. The evolving damage density is incorporated in the second order damage tensor. Such randomness in damage nucleation and annihilation process for composite is significantly important particularly under synergistic environmental ageing parameters i.e. the environmental parameters containing Gaussian noise. This important phenomenon in composite damage evolution has not been treated by any earlier investigators. In this extended model, we may consider nucleation/annihilation rates as jump processes. In order to consider all these factors the BFSDE approach is the most compatible one. Hence, the proposed model will improve the life prediction methodologies that are currently implied for composite materials.

5. NOMENCLATURE

n: Micro-crack density.

x_1, x_2, x_3: Spatial coordinates of the micro-crack tip.

c: Crack length.

$A(n, t, x_1, x_2, x_3, c, \mu, h, T : \sigma)$: Micro-crack growth rate for a certain load σ.

μ: Moisture content in RVE.

h: Hardening parameter in RVE.

T: Temperature in RVE.

V_1, V_2, V_3: Micro-crack tip velocity in spatial directions.

φ: Moisture content changing rate in RVE.

H: Hardening parameter changing rate in RVE.

θ: Temperature changing rate in RVE.

$n_N; n_A$: Damage/micro-crack nucleation and anihillation rate in RVE.

REFERENCES

[1] Chaim R., Baum L. and Brandon D. G. Mechanical Properties and Microstructure of Whisker- Reinforced Alumina–30 vol% Glass Matrix Composite. Journal of the American Ceramic Society, 1989. 72(9): p. 1636-1642.

[2] Oliveira, B. F. and Creus, G., J. An Analytical-Numerical Framework for the Study of Ageing in Fiber Reinforced Polymer Composites. Composite Structures, 2004. 65: p. 443-457.

[3] Case, S. W. and Reifsnider, K. L. Micromechanical Analysis of Fiber Fracture in Unidirectional Composite Materials. International Journal of Solids and Structures (UK), 1996. 33(26): p. 3795-3812.

[4] Talreja, R. A Continuum Mechanics Characterization of Damage in Composite Materials. Proceeding of Royal Society of London. Series A, Mathematical and Physical Sciences, 1985. 399(1817): p. 195-216.

[5] Talreja, R. Internal Variable Damage Mechanics of Composite Materials. In: Boehler, J.P (Ed.), Yielding, damage and failure of Anisotropic Solids, EGF 5, 1990. p. 509-533.

[6]. McManus, H L. and Michii, Y. Prediction of Microcracking Distributions in Composite Laminates using a Monte-Carlo simulation method. Journal of Reinforced Plastics and Composites (USA), 1997. 16(13): p. 1220-1230.
[7]. Augusti, G and Mariano, P.M. Stochastic Evolution of Microcracks in Continua. Computer Methods in Applied Mechanics and Engineering, 1999. 168: p.155-171.
[8]. Bai, Y ,Han, W and Bai, J. A Statistical Evolution Equation of Microdamage and its Application. Applications of Continuum Damage Mechanics to Fatigue and Fracture; Orlando, Florida; USA; 21 May 1996, 1997. p. 150-162.
[9]. R. Rahman, A. Haque ,Stochastic Modeling of Damage Evolution and Stiffness Degradation in Composites under Environmental ageing, SAMPE conference, Memphis, Tennessee, Sept. 9-11, 2008, USA.
[10]. R. Rahman, A. Haque, A Theoretical Model for Prediction of Damage Evaluation and Degradation in Composites due to Environmental Ageing, 23rd ASC technical conference, Sept. 9-11, 2008, Memphis, Tennessee, USA.

Proceedings of the 4th BSME-ASME International Conference on Thermal Engineering
27-29 December, 2008, Dhaka, Bangladesh

EFFECTS OF MINIMUM QUANTITY LUBRICATION BY VEGETABLE OIL-BASED CUTTING FLUID ON TEMPERATURE, CHIP MORPHOLOGY AND SURFACE FINISH IN GRINDING AISI 1060 STEEL

M. A. ISLAM[1] and N.R. DHAR[2]

[1]Lecturer
Department of Industrial & Production Engineering
Rajshahi University of Engineering & Technology (RUET)
E-mail: maislam252@yahoo.com
[2]Professor
Department of Industrial & Production Engineering
Bangladesh University of Engineering & Technology
E-mail: nrdhar@ipe.buet.ac.bd

ABSTRACT

In all grinding process, high accuracies, close dimensional tolerances, and a fine surface finishes are required. The abrasive action of grinding generates excessive heat. Such high temperature often leads to several problems like a large heat affected zone, change in hardness and microstructure of the work piece, burning and its consequences and micro cracks. Application of proper grinding fluids can reduce the above problems to some extent through cooling and lubrication of the grinding zone. The conventional cutting fluids used in grinding process cause a serious problem to manufacturers, since these substances can seriously damage human health and environment. Large quantities of emulsion-based cutting fluids for machining and grinding increases cost as well as impacting the environment. This paper deals with experimental investigation on the role of MQL by vegetable oil on grinding zone temperature, chips morphology and surface roughness in grinding AISI 1060 Steel by diamond grinding wheel. The encouraging results include significant reduction in surface roughness by MQL mainly through reduction in the grinding zone temperature and favorable change in the work-tool interaction.

KEYWORDS: *Minimum Quantity Lubrication, temperature, chips morphology, surface roughness*.

1. INTRODUCTION

The growing demand for higher productivity, product quality and overall economy in manufacturing by machining, particularly to meet the challenges thrown by liberalization and global cost competitiveness, insists high material removal rate and high stability and long life of the cutting tools. However, high production machining is inherently associated with generation of large amount of heat resulting high cutting zone temperature. Such high cutting zone temperature not only deteriorates dimensional accuracy and tool life but also impairs the surface integrity of the product [**1**]. High cutting temperature accelerates the growth of tool wear and also enhances the chances of premature failure of the tool by plastic deformation and thermal fracturing.

However, conventional cutting fluids are still widely used. The major problems of conventional cutting fluid application are [**2,3**] (i) environmental pollution due to chemical break-down of the cutting fluid at high cutting temperature (iii) biologically hazardous to operator due to bacterial growth (iv) requirements of additional system for pumping, local storage, filtration, recycling, chilling and large space and (iv) water pollution and soil contamination during final disposal. Conventionally employed cutting fluid fails to penetrate the chip-tool interface and removes heat by bulk cooling [**4**].

Minimum quantity lubrication refers to the use of cutting fluids of only a minute amount-typically of a flow rate of 50 to 500 ml/hour-which is about three to four orders of magnitude lower than the amount commonly used in flood cooling condition, where, for example, up to 10 liters of fluid can be dispensed per minute. The concept of minimum quantity lubrication, sometimes referred to as "near dry lubrication" [**5**] or "micro lubrication" [**6**], has been suggested since a decade ago as a means of addressing the issues of environmental intrusiveness and occupational hazards associated with the airborne cutting fluid particles on factory shop floors. The minimization of cutting fluid also leads to economical benefits by way of saving lubricant costs and workpiece, tool, machine cleaning cycle time. A recent survey conducted on the production of the European automotive industry revealed that the expense of cooling lubricant comprises nearly 20% of the total manufacturing cost [**7, 8**]. In comparison to cutting tools, the cooling lubricant cost is significantly higher. As a result, the need to reduce cutting fluids consumption is strong. The oil mist level in U.S. automotive parts manufacturing facilities has been estimated to be generally on the order of 20-90 mg/m^3 with the use of traditional flood cooling and lubrication [**8**]. This suggests an opportunity for improvement of several orders of magnitude.

On the other hand, completely dry cutting has been a common industry practice for the machining of hardened steel parts. These parts typically exhibit a very high specific cutting energy. Traditional beliefs indicate that completely dry cutting of them, as compared to flood cutting, lowers the required cutting force and power on the part of the machine tool as a result of increased cutting temperature. However, achievable grinding tool life and part finish often suffer under completely dry condition. Therefore, the permissible infeed is to be restricted. Under these considerations, the concept of minimum quantity lubrication presents itself as a possible solution for grinding AISI 1060 Steel in achieving slow grinding wheel wear while maintaining cutting temperature at reasonable levels, provided that the minimum quantity lubrication parameters can be strategically tuned. However, there has been no documented study so far that investigates the feasibility of using minimum quantity lubrication in hard material grinding processes.

The purpose of this research is to study the role of minimum quantity lubrication condition on the grinding temperature, grinding chips morphology and surface roughness performance of AISI 1060 steel, as compared to completely dry cutting. An approach based on the tool work combination method has been performed to identify the ideal testing parameters range. The study helps to provide an understanding of the behavior of the chips morphology and the workpiece under minimum quantity lubricant conditions. In the study, the minimum quantity lubrication is provided with a spray of air and vegetable oil. During each test, cutting temperature, grinding chips morphology and surface roughness are investigated and compared. The following sections describe the experimental condition, experimental results and discussion and conclusion.

2. EXPERIMENTAL INVESTIGATION

Experiments have been carried out by grinding 40 mm x 25 mm x 8 mm AISI 1060 steel in a Horizontal Spindle Surface Grinding Machine at different infeeds under dry, wet and minimum quantity lubricant condition to study the role of minimum quantity lubrication technique by vegetable oil (olive oil) on Grinding characteristics of that work material mainly in respect of grinding zone temperature, chips morphology and surface roughness. The experimental conditions have been given in Table-1. Nozzle is placed 35 mm apart from the cutting zone and 20^0 with horizontal to minimize the interference of the nozzle with the flowing chips and to reach quite close to the workpiece and grinding wheel contact zone.

Effectiveness of cooling and the related benefits depend on how closely the minimum quantity coolant jet can reach the work-tool interfaces where heat is generated. The positioning of the nozzle tip with respect to the work-tool interfaces has been settled after a number of trials. The final arrangement made and used has been shown along with photographic view of experimental set-up in Fig.1.

Grindability is usually judged by: (i) the magnitude of the grinding zone temperature which affects grinding defects, product quality and grinding wheel performance, wear and life, (ii) surface finish and (iii) pattern and mode of chip formation. In the present work grinding zone temperature, chips morphology and surface finish are considered for studying the role of minimum quantity lubrication application. The average cutting temperature was measured under all the machining conditions undertaken by simple but reliable tool-work thermocouple technique with proper calibration. A graphite block was used as a uniform heat source that gains heat from an electric crucible. A carbide rod and a strip of work material joined together at one edge and embedded in the graphite block and the other edges were connected with the terminals of a milivoltmeter. A temperature probe was placed in such a way that the probe and the aforesaid junction be equidistant from the wall of the crucible.

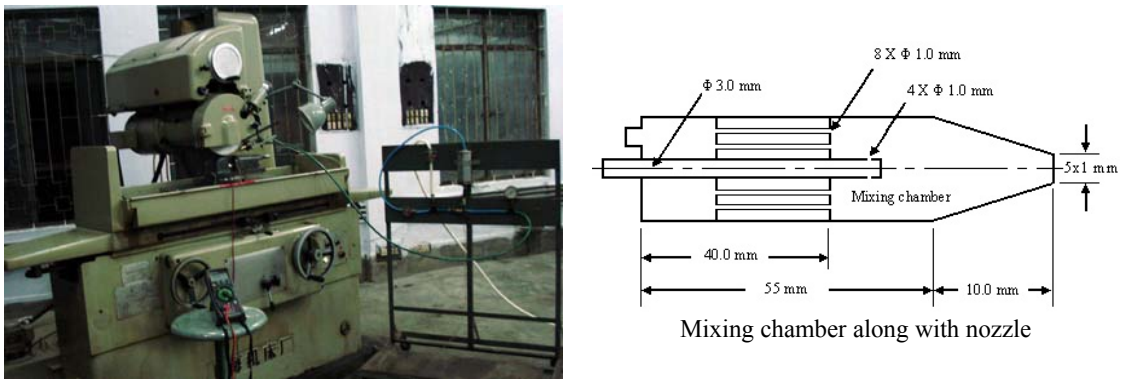

Fig. 1: Photographic view of experimental set-up.

Table-1: Experimental Conditions

Machine	: Horizontal Spindle Surface Grinding Machine with Rectangular Table (model: M7120A), 2.8 kW
Spindle speed	: 3000 rpm
Wheel speed	: 39.89 m/sec
Table speed	: 6 m/min
Infeed	: 10 µm, 20 µm, 30 µm and 40 µm
Wheel	: D126R100 B60-3 mm
Workpiece materials	: AISI 1060
Hardness (BHN)	: 179
Workpiece size	: 40 mm x 25 mm x 8 mm
MQL Supply	: Air- 8 bar, Lubricant- Vegetable oil, 120 ml/h through external nozzle having 5 mm x1 mm tip.
Environments	: i) Dry condition ii) Flood cooling with soluble oil and iii) Minimum Quantity Lubrication Cooling

Grinding chips were collected during the experiment by placing a glass slide coated with petroleum jelly on the spark stream during grinding. The collection of the chips were carried out only after the grinding has reached the steady state indicated by almost no vibration in the magnitude of the grinding forces with the number of passes. Those chips were thoroughly washed with acetone, dried and magnetically separated from the grinding wheel debries. After that dried chips were preserved by covering with aluminum foil. Then the cleaned chips were mounted on small disk and observed under scanning electron to study the morphological characteristics of the chips. The SEM views of the chips obtained under the different environments and at different infeeds. After grinding the specimen by diamond wheel, at different infeed and different environment dry, wet and MQL conditions the surface roughness was measured. A Talysurf using a sampling length of 0.8 cm has measured the surface roughness of the ground specimens in transverse and longitudinal directions.

3. EXPERIMENTAL RESULTS AND DISCUSSION

During grinding any ductile materials, heat is generated due to (i) shear and plastic deformation, (ii) rubbing at the work-tool interface. All such heat sources produce maximum temperature at the chip-tool interface, which substantially influence the chip formation mode, surface roughness and grinding wheel wears. Therefore, attempts are made to reduce this detrimental grinding temperature. Conventional cutting fluid application may, to some extent, cool the tool and the job in bulk but cannot cool and lubricate effectively as expected at the chip-tool interface where the temperature is maximum. This is mainly because the flowing chips make mainly bulk contact. Bulk contact does not allow the cutting fluid to penetrate in the interface. Cutting fluid reaches only over a small region at the grinding zone by capillary action. The cutting fluid action becomes more and more ineffective at the interface. Then grinding zone temperature is plotted against infeed in different environments.

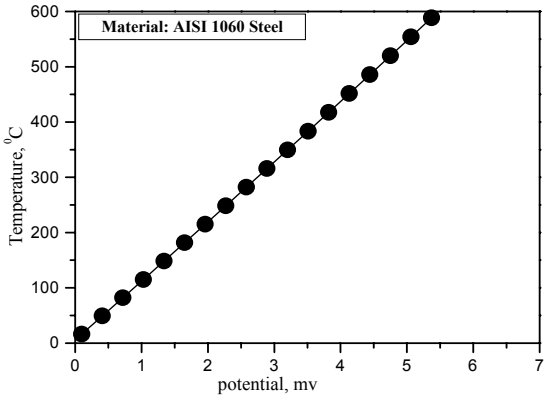

Fig. 2: Temperature calibration curves for AISI-1060 steel.

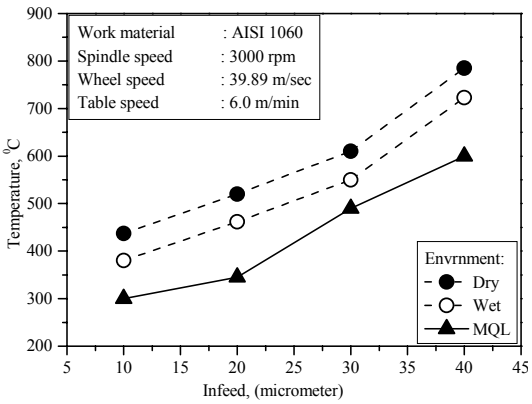

Fig.3: Variation of grinding zone temperature with infeed under different environments

The Fig.3 shows the effect of minimum quantity lubrication on average grinding zone temperature under different infeed as compared to dry and wet condition. However from the aforementioned figures it is clear that increasing the infeed increases the grinding temperature even under MQL condition due to increases in energy consumption and higher material removal rate. But minimum quantity lubrication still more effective as compared to dry and wet conditions. However, it is observed that minimum quantity lubrication in its present way of application enable the reduction of the average cutting temperature by about 10% to 30% depending upon the infeed and other process parameter.

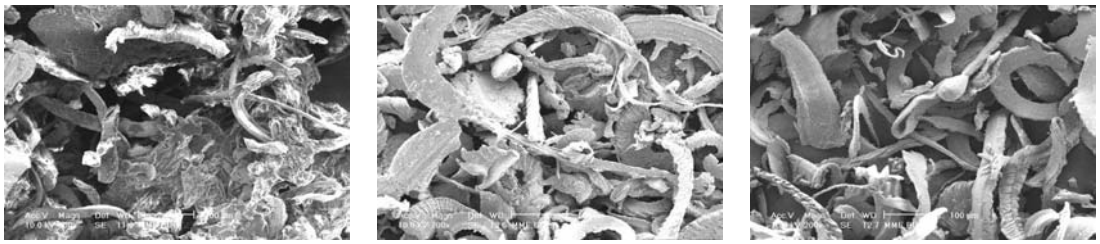

(a) Dry **(b) Wet** **(c) MQL**

Fig. 4: SEM photographs of grinding chips at 10 µm infeed while grinding AISI 1060 Steel at different environments.

The study of grinding chip is required to understand the mechanism of chip formation and those of material removal. The chips produced during grinding AISI 1060 steel at lower infeed 10 µm have been shown in the Fig.4 under the different environments. Dry grinding at 10 µm infeed provided different types of chips such as lamellar, spherical, irregular shaped and blocky particles which are shown in Fig.4. This indicates that at dry environment the mechanism of chip formation is particularly shearing, ploughing and rubbing. From Fig.5 at higher infeed (40µm) also some small and medium sizes chips have taken up spherical shape are found, this may be for excessive heating. Here most of the chips are leafy which produced by rubbing action between wheel and work piece. Higher grinding zone temperature and ductility of steel specimens are expected to yield larger number of spherical chips. Chips produced under minimum quantity lubrication condition at both lower and higher infeeds provided approximately equal width also along with long lamellar chips are mainly by shearing due to lower grinding zone temperature. By studying the chip characteristics, it is evident that in dry grinding the mechanism of chip formation is mainly due to ploughing and rubbing and some are by shearing. On other hand, in minimum quantity lubrication the mechanism of material removal to mainly shearing, there are some irregular shapes also found.

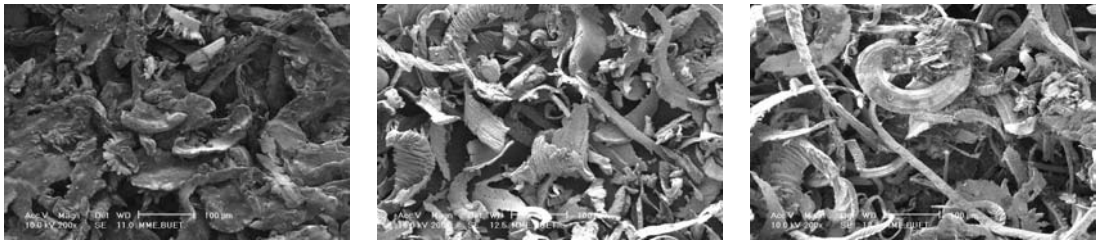

(a) Dry **(b) Wet** **(c) MQL**

Fig. 5: SEM photographs of grinding chips at 40 µm infeed while grinding AISI 1060 Steel at different environments.

Surface finish is an important index of grindability .The variation in surface roughness observed with progress of machining of AISI 1060 by the diamond grinding wheel at different infeed under dry, wet and MQL conditions has been in shown in Fig.6. At dry condition the surface roughness in more compared to other environments. But the surface roughness reduces under wet machining compared to dry, which may due to for the lubrication and reduction in the grinding zone temperature. MQL appeared to be effective in reducing surface roughness. However, it is evident that MQL improves surface finish depending upon the work-tool materials.

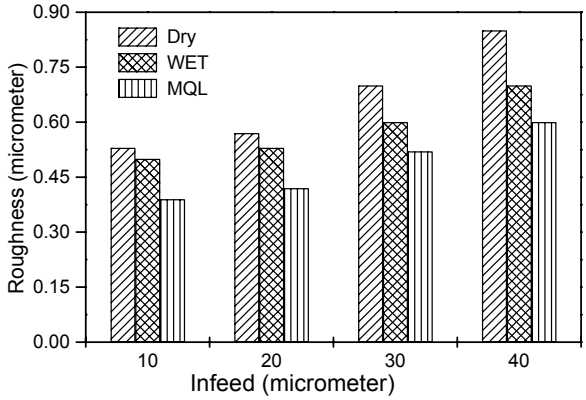

Fig. 6: Variation in the surface roughness with infeed under different environments conditions while grinding AISI 1060 Steel.

4. CONCLUSIONS

i) The present minimum quantity lubricant systems enabled reduction the average grinding zone temperature up to 20 to 30% depending on the process parameter. In the present experiment minimum quantity lubrication perfectly reached to the wheel-work interface up to 20 micrometers infeed. After that further increase the infeed reduces the effect of minimum quantity lubrication. Flood cooling by soluble oil could not control the grinding temperature appreciably.

ii) Minimum quantity lubrication provided significant improvements expectedly, though in varying degree, in respect of chip formation modes, surface characteristics throughout the infeed range undertaken mainly due to reduction in the grinding zone temperature. In MQL environment the chip formation modes is mainly due to shearing but in dry environment some chips are formed by shearing and most of the chips are found leafy chips which are formed by the rubbing action.

iii) The surface roughness in minimum quantity lubrication is better than the wet and dry condition due to reduction of damage of grinding wheel grits at lower grinding zone temperature.

5. ACKNOWLEDGEMENT

This research work has been funded by Directorate of Advisory Extension and Research Services, BUET, Dhaka, Bangladesh. The authors are also grateful to the Department of Industrial and Production Engineering, BUET for providing the facilities to carryout the experiment.

6. REFERENCES

[1] Chao, B. T. and Trigger, K.J., "Temperature Distribution at the chip-tool interface in metal-cutting", Trans. of the ASME, 1995, Vol.77,1107

[2] Malkin S. and Lenz E., "Burning Limit for Surface and Cylindrical Grinding of Steels", Annals of CIRP, Vol.27 (1), pp.233, 1978.

[3] Yasui H. and Tsukuda S., "Influence of Fluid Type on Wet Grinding Temperature", JSPE, Vol.17, pp.133, 1983.

[4] Howes T., "Assessment of the Cooling and Lubricative Properties of Grinding Fluids", Annals of CIRP, Vol.39 (1), pp.313, 1990.

[5] Klocke, F., Eisenblatter, G., "Dry Cutting" Annals of the CIRP, 46 (2), pp. 519-526, 1997.

[6] Byrne, G. and Scholta, E., "Environmentally Clean Machining Process - A Strategic Approach", Annals of CIRP, Vol.42/1, pp.471-474, (1993)

[7] Bennett, E.O. and Bennett, D.L., "Occupational Airway Diseases in the Metal-Working Industry", Tribology International, 18/3, pp.169-176, 1985

[8] MaClure, T. F., Adams, R. and Gugger, M. D, Comparison of Flood vs. Microlubrication on Machining Performance, website: http://www.unist.com/techsolve.html, 2001.

Proceedings of the 4th BSME-ASME International Conference on Thermal Engineering
27-29 December, 2008, Dhaka, Bangladesh

CHEMICAL AND STRUCTURAL NATURE OF SURFACE AND SUBSURFACE OF WORN AL-B_4C COMPOSITES

K.M. SHOROWORDI[1*], A.S.M.A. HASEEB[2], J.P. CELIS[3]

[1*]Institute of Appropriate Technology, Bangladesh University of Engineering and Technology (BUET), Dhaka 1000, Bangladesh, kmshorowordi@iat.buet.ac.bd

[2]Department of Mechanical Engineering, University of Malaya, 50603 Kuala Lumpur, Malaysia

[3]Department of Metallurgy and Materials Engineering (MTM), Catholic University of Leuven, de Croylaan 2, Heverlee, B 3001, Belgium

ABSTRACT

Worn surface of Al-B_4C metal matrix composites (MMC) sliding against phenolic brake pad at sliding speeds of 1.62 m s^{-1} under contact pressures of 0.75, 3.00 MPa and 4.17 m s^{-1} under 0.75 MPa in a pin-on-disc apparatus was investigated. Scanning electron microscopy (SEM) was used to study the structure of the surface and subsurface region of worn sample. X-ray photoelectron spectroscopy (XPS) was used to analyize chemical composition from the top few nanometres of the worn surface, while energy dispersive x-ray microanalysis (EDX) provided information from within a few micrometres. Results reveal that the surface of Al-B_4C undergoes significant chemical and physical changes during wear. The worn-surface on Al-B_4C is converted into a mixture that contains the constituents of Al-B_4C and the phenolic pad counter body e.g. C, Mg, Si, O, Fe, Ca as well as oxygen from atmosphere. The worn surface obtained in the present study is suggested to consist of continuous mixed top layer of a few μm in thickness in which topmost few nanometres of this mixed layer is totally oxidized. A thick mechanically mixed layer (MML) termed as massive MML also forms in addition with the continuous top layer. Its thickness and coverage is found to be load dependent. The massive MML is found to contain defects and debonding from bulk MMC. It is heterogeneous at the micrometre scale. The characteristics of the modified surface are discussed and a schematic model for the Al-B_4C MML is proposed.

KEY WORDS: *Al-B_4C MMC, wear, mechanically mixed layer, XPS, SEM-EDX.*

1. INTRODUCTION

Metal matrix composites (MMC) having a high strength-to-weight ratio is of great importance particularly in the aerospace and automotive sectors where weight saving leading to lower fuel consumption is a prime consideration. The tribological properties of Al-MMC reinforced by hard ceramic particles have also been found to improve wear resistance of aluminium to a great extent as compared to ureinforced alloy. These materials have already led their applications to aerospace and automotive sector viz. brake rotor, piston etc. for its improved tribological properties coupled with high strength-to-weight ratio. Considerable amount of research has been carried out on the tribology of Al-MMC, particularly on the Al-SiC system. In majority of these studies, mainly ferrous materials have been used as counter body [1-7]. A few studies involving brake pad material as counter body have also appeared recently [7-11]. These studies revealed that during sliding of Al-MMC, worn surface forms a layer termed as mechanically mixed layer (MML)

which contains the constituents of both MMC and the counter body. No such transfer layer or MML was found to form on unreinforced aluminium. The presence of the mechanically mixed layer was suggested to control greatly the wear rate and friction coefficient of Al-MMC [1-8]. It has also been reported that under conditions where MML is not allowed to form, the wear rate of MMC is quite high [3].

The nature of MML has been studied in a number of research [3,4,6] mainly by optical microscopy, scanning electron microscopy (SEM) and energy dispersive x-ray microanalysis (EDX). XPS has been introduced recently to analysis depthwise composition of tribo-surface of cast iron rotor slide against brake pad [12]. Using the data obtained from XPS and SEM-EDX, a schematic model has been proposed to describe the characteristics of the modified tribo surface on Al-SiC MMC against brake pad [11]. B_4C particle has been considered as reinforcement for its higher hardness as compared to SiC. It can be mentioned that although a considerable amount of information on the tribo surface of Al-MMC siding against ferrous counterbody is available in the literature, similar information pertaining to Al-B_4C MMC/phenolic pad couple, which is of practical importance in auto brake systems, is relatively scarce in the open literature. The present work therefore attempts to characterize the chemical and structural nature of the surface and subsurface of Al-13vol% B_4C sliding against a commercial phenolic brake pad. Based on the results obtained in the present work, a schematic model for the modified surface is also proposed.

2. EXPERIMENTAL

Al-13vol%B_4C metal matrix composite was used as pin material and a commercial phenolic based brake pad was used as counter body. The MMC was prepared using commercially pure aluminium (99.99%) and 40 μm sized SiC particles by stir-cast method followed by hot extrusion at a extrusion ratio of 1. MMC pins of 5 mm diameter and 12 mm length were used for wear tests. The end surface of the pin was polished using emery paper 1200, cleaned in distilled water and then dried in acetone prior to the wear tests. The main constituents of the commercial brake pad used in this study are phenolic resin, asbestos fiber, copper, zinc and iron. X-ray fluorescence spectroscopic investigation detected a number of elements viz. O, Mg, Si, Al, S, Ca, Fe, Cu, Zn, Ba and C on the pad. Detailed characterisation of the pad used in this study is given elsewhere [7]. Discs having a dimension of 65 mm diameter and 10 mm thickness were cut from the pad. Prior to the wear test, one surface of the disc was polished with emery paper 1200, and cleaned with dry cotton.

All the wear tests were conducted in ambient air having a relative humidity and temperature of 77±5% and 31±2^{o} C respectively. A pin-on-disc type wear testing setup was used. In the setup, the end surface of the cylindrical MMC pin presses against the phenolic disc that rotates in a horizontal plane. Wear tests were conducted at a linear sliding speed of 1.62 m s^{-1} under contact pressures of 0.75 and 3.00 MPa, and sliding speed 4.17 $m.s^{-1}$ under 0.75 MPa for 1 hour. X-ray photoelectron spectroscopy (XPS) was performed in Escalab 220I-XL at a base pressure of 10^{-8} Pa using AlK_{α} with a spot size about 1 mm. The data were collected in the constant analyser energy mode with pass of 20 eV. Native and worn surfaces were investigated after a mild etch (3keV Ar^{+}, 0.1 μA/mm^2, 15s) to remove contaminants. The spectra were calibrated against C1s peak. The cross-section of the worn surface of the MMC pins was examined by scanning electron microscope (SEM) (Philips XL30) equipped with an energy dispersive x-ray (EDX) analyser.

3. RESULTS AND DISCUSSION

Fig. 1 shows the XPS spectra recorded on native and worn Al-B_4C MMC surfaces. The native surface mainly contains Al, B and C. Oxygen peak is also visible in the spectra of the native surface which is due to the natural oxidation of the sample. The high intensity of carbon peak in the spectrum is due to contamination of the native surface which also lowers the intensity of Al2p peak. In addition to the peaks of the above elements, the XPS spectrum of the worn surface of Al-B_4C MMC sample contains a number of other elements viz., Si, Mg, Ba, Fe, Ca. These elements obviously came from the counter body to the MMC surface. The Al2p peak of aluminium was separately recorded on both native and worn MMC surfaces and is compared in Fig. 2. On the native surface, the Al2p peak splits into two: one at 73 eV is due to the metallic state of aluminium while the other at 75.5 eV is due to Al2p in the oxidized state, presumably caused by the presence of native oxide. On the worn sample, metallic state of aluminium is completely absent. Aluminium is seen to be present only in the oxidized form. Fig. 3 shows B1s peak at 187.5 eV identified as boron carbide on the surface of native Al-B_4C MMC, while the worn surface shows two B1s peaks at 187.5 and 196eV. The latter one is weak and identified as oxide of boron. The oxidized boron peak is seen to occur at higher binding energy (196eV) as compared with the standard peak position (193.3ev). It may be mentioned that the peak of oxidized silicon occurs on the worn surface of Al-SiC MMC at higher binding energy [11]. Writh et al. also observed that the XPS spectrum of the worn surface of cast iron slid against brake pad exhibited peak of oxidized iron at higher binding energy [13]. They attributed this peak shifts due to the possible complex formation during the wear process.

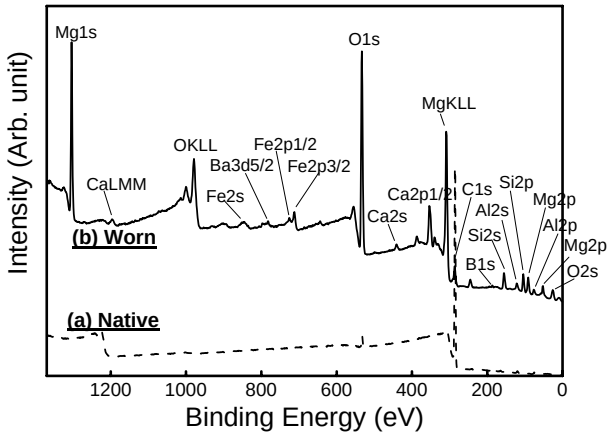

Fig. 1 XPS survey spectra recorded on (a) native and (b) worn Al-B_4C MMC surface [Sliding speed: 1.62 m s^{-1}, contact pressure: 0.75 MPa]

Fig. 4 shows a secondary electron image of a cross section of the worn surface of the Al-B_4C MMC. A modified layer termed as MML is visible at the surface of the worn specimen in Fig. 4. Its thickness varies from place to place and is seen to be up to about 20-50 μm at places. This layer is not continuous rather it becomes discontinuous at particle populated area. The evidence of debonding of this MML from bulk Al-B_4C MMC as separate line is observed like a third body layer. It can be mentioned that this type of debonding was not found in case of Al-SiC MMC. At higher magnification, it is observed that the layer contains fragments of boron carbide, small amount of pad materials (slightly dark color) with mainly Al (light color) (Fig. 4b). These constituents in MML are not well mixed like the MML on Al-SiC MMC. In the particular micrograph in Fig. 4a, the thickness of the layer is seen to be influenced by the presence of a hard B_4C underneath.

It is seen that both chemical and structural changes occur at the surface and subsurface of Al-B_4C MMC sliding against the commercial phenolic brake pad (Fig. 1 and

Fig. 4). The MML in the present case can be suggested to consist of a relatively finely mixed top layer of a few μm in thickness and massive MML of a few tens of μm in thickness which is completely separate from the bulk Al-B_4C MMC.

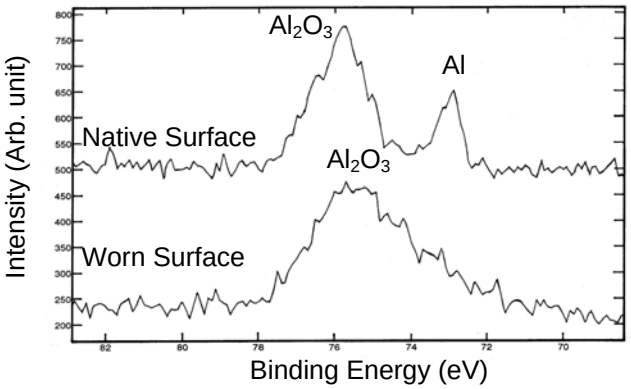

Fig. 2 A comparison of Al2p peak on native and worn Al-B_4C MMC [Sliding speed: 1.62 m s^{-1}, contact pressure: 0.75 MPa]

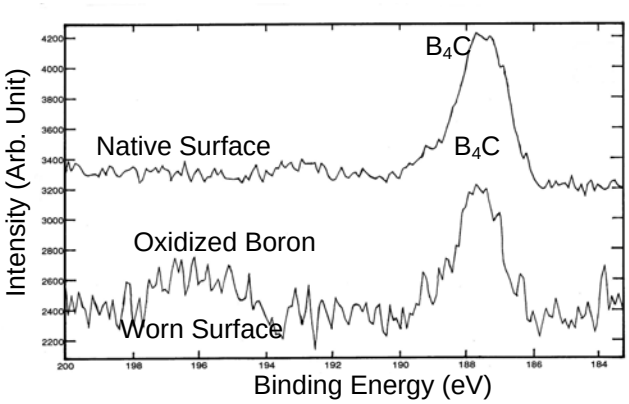

Fig. 3 A comparison of B1s peak on native and worn Al-B_4C MMC [Sliding speed: 1.62 m s^{-1}, contact pressure: 0.75 MPa]

The top of MML is a couple of micrometres in thickness. It is subjected to maximum shear during sliding and has a finely mixed structure. Given the depth resolution of EDX (of the order of a few μm) and the widespread occurrence of the pad constituents on the worn MMC surface [14], it is thought that a continuous mixed layer of a few micrometres in thickness covers the top surface of the worn Al-B_4C MMC. XPS also shows that the topmost few nanometres of this layer, being exposed directly to air, is totally oxidized even B_4C decomposed into oxidized boron. In addition to the continuous top layer a thick massive MML like a third body, also forms (Fig. 4a). The massive MML contains lots of defects like voids, cracks, debonding etc. The extent of coverage and thickness of massive MML is found to vary with normal load. At higher loads, massive MML covers wider areas on the surface.

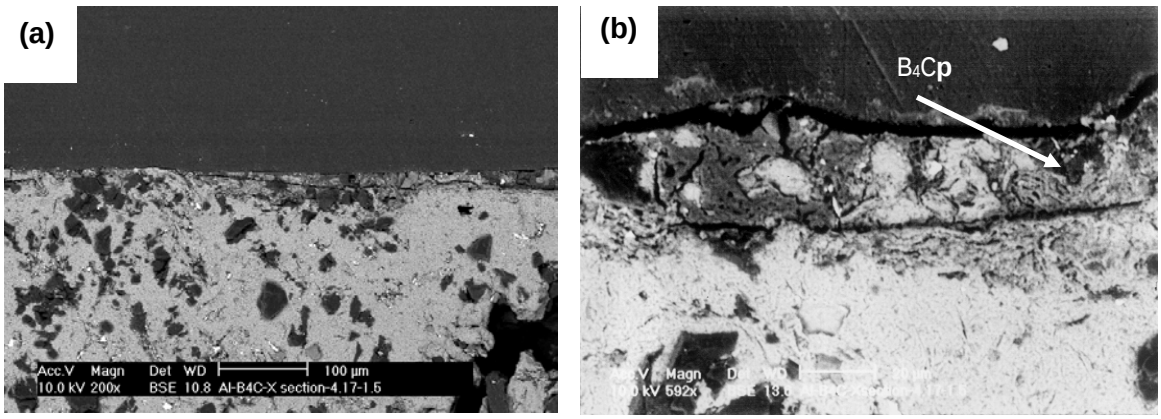

Fig. 4 SEM images of cross-section of worn Al-B_4C MMC (a) low magnification and (b) high magnification [Sliding speed: at 4.17 m s^{-1}; Contact pressure: 0.75 MPa]

The topography of the worn surface at high load showed delamination of flaky debris [14]. The nature of the crack suggests that the delaminating material is brittle. The delamination is likely to occur in the MML itself and the unconsolidated, inhomogeneous nature of the massive MML is expected to favour brittle fracture. It is to be noted that the wear process in Al-B_4C MMC in the present study has been found to be mainly abrasive.

It was reported that continued shear during wear leads to the development of subsurface structure having a top layer termed as Zone 3, which is a compositionally mixed layer containing constituents of the specimen, counter body and environment [15, 16]. This zone forms as a result of transfer and mixing of constituents by shear. It has been found that Zone 3 is very finely divided mechanical mixture whose grain size can be only a few nanometres. Evidence showed that the structure of Zone 3 is very similar to that of mechanically alloyed materials [15, 16]. Above information on the development of surface and subsurface structure on worn metallic materials and MMC leads us to suggest that the finely mixed top portion of the MML in the present study is linked to Zone 3 and shear is thought to play a major role in its formation. As for the massive MML, different mechanisms viz., turbulent flow mechanism [3,4,6], debris burial [5,10,17], and press-slide flattening [18] are believed to contribute to its formation.

Previous study proposed a schematic model for the MML on Al-SiC MMC sliding against phenolic brake pad (Fig. 5) [11]. It was reported that the top few micrometer of the layer are finely mixed and continuous over the worn surface where few nanometers at the topmost of this layer get completely oxidized. In addition, a massive well mixed MML formed on the worn surface of MMC which varied from place to place on the worn sample (Fig. 5).

The model based on the present investigation proposed that the topmost few nanometres of the worn surface is a mixed as well as completely oxidized layer as evidenced by XPS (Fig. 6). Based on the analysis depth resolution of EDX [19], it is also suggested that a continuous finely mixed MML, a few micrometres in thickness, form on the MMC worn surface. A massive MML forms on the subsurface of Al-B_4C MMC and its thickness varies from place to place on the same specimen. The structure of this massive MML found on Al-B_4C MMC differs in two aspects from the MML on Al-SiC MMC. Firstly, the MML in present case is not well mixed like the MML on Al-SiC MMC and secondly, the evidence of debonding from bulk MMC is observed as clear demarcation (Fig. 6). The causes of formation of this debonding require further investigations.

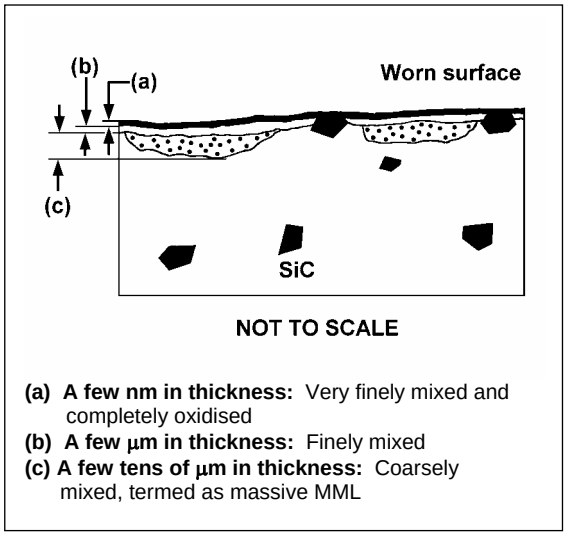

Fig. 5 Schematic model proposed for mechanically mixed layer on Al-SiC MMC in previous work [11]

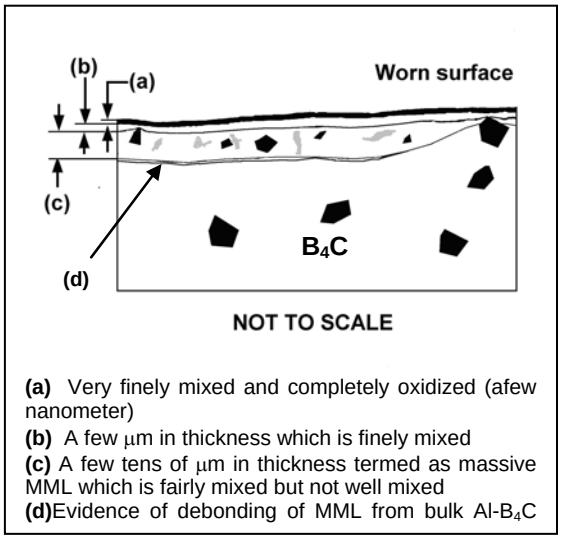

Fig. 6 Proposed schematic model for mechanically mixed layer on Al-B4C MMC based on the present work

4. CONCLUSIONS

(1) The surface and sub-surface on Al-B_4C is converted into a heterogeneous mixture of the constituents of Al-B_4C MMC and the phenolic pad counter body e.g., C, Mg, Si, O, Fe, Ca as well as oxygen from atmosphere.
(2) The worn surface consist of a relatively finely mixed top layer of a few μm in thickness which form continuously and quickly mends itself if some breakage occurs. The topmost few nanometres of this finely mixed layer is totally oxidized.
(3) A thick mechanically mixed layer (MML) termed as massive MML also forms, in addition with the continuous top layer. This MML consists of fragments of boron carbide and constituents of pad which are not consolidated like the MML on Al-SiC MMC.
(4) The MML thickness varies from place to place and is seen to be up to about 20-50 μm at places. Its thickness and coverage is found to be load dependent.
(5) The MML is found separate from bulk Al-B_4C MMC like a third body layer and it contains defects heterogeneously.

ACKNOWLEDGEMENTS

The authors acknowledge the support provided by the Committee for Advanced Study and Research (CASR), BUET. This work benefited from joint research collaboration between BUET and the Catholic University of Leuven, Belgium supported by the Belgian Agency for Development Cooperation, and the Ministry of Education, Bangladesh.

REFERENCES

[1] X.Y. Li, K.M. Tendon, *Wear,* Vol. 245(2000), pp.148-161.
[2] G. Staffelini, *Wear,* Vol. 245(2000), pp. 216-222.
[3] B. Venkataraman, G. Sundararajan, *Acta Mater,* Vol. 44(1996), pp.451-60.
[4] B. Venkataraman, G. Sundararajan, *Acta Mater,* Vol. 44(1996), pp.461-473.
[5] D. Lu, M. Gu, Z. Shi, *Tribology Letters,* Vol. 6(1999), pp.57-61.
[6] B. Venkatraman, G. Sundararajan, *Wear,* Vol. 245(2000), p. 22.
[7] K.M. Shorowordi, A.S.M.A. Haseeb, J.P. Celis, *Wear,* Vol. 256 (2004), pp.1176-1181.
[8] G. Straffelini, M. Pellizzari, A. Molinari, *Wear,* Vol. 256(2004), p. 754.
[9] G. Howell, A. Ball, *Wear,* Vol. 181-183(1995), p. 379.
[10] I. Sallit, C. Richard, R. Adam, F. Robb-Valloire, *Materials Characterization,* Vol. 40(1998), pp.169-188.
[11] K.M. Shorowordi, A.S.M.A. Haseeb, J.P. Celis, *Materials Science and Engineering A,* Vol. 425 (2006), pp. 213-218.
[12] W. Osterle, I. Urbran, Third body formation on brake pads and rotors, *Tribology International,* Vol. 39(2006), pp. 401-408.
[13] A. Writh, R. Whitaker, S. Turner, G. Fixter, *Journal of Electron Spectroscopy and Related Phenomena,* Vol. 68(1994), pp. 675-683.
[14] K.M. Shorowordi, A.S.M.A. Haseeb, J.P. Celis, Tribo-surface characteristics of Al-B_4C and Al-SiC composites worn under different contact pressures, *Wear,* Vol. 261(2006), pp.634-641.
[15] D.A.Rigney, L.H. Chen, M.G.S.Naybr, A.R.Rosenfield, *Wear,* Vol. 100(1984), p. 195.
[16] S.L. Rice, H. Nowotny, S.F. Wayne, in "The Role of Subsurface Zones in the Wear of Materials (Trans Tech Publications, Switzerland, 1988), p. 77.
[17] N. P. Suh, "Tribophysics" (Prentice-Hall Inc., New Jersey, 1986).
[18] T. Sasada, *Wear,* Vol. 100(1984), p. 561.
[19] R.C. Brundle, C.A. Evans, S. Wilson, in "Encyclopedia of Materials Characterization" (Butterworth-Heinemann, Boston, 1992), p. 22.